DLR-IB-AE-GO-2017-149

Mistuned Flutter Analysis of Strongly Coupled Bladed Disks in Conjunction with Reduced Order Modeling

Dimitri Franz

Institut für Aeroelastik

Deutsches Zentrum
DLR für Luft- und Raumfahrt

Mistuned Flutter Analysis of Strongly Coupled Bladed Disks in Conjunction with Reduced Order Modeling

Zusammenfassung:

A flutter analysis for a mistuned cantilevered and shrouded bladed disk is conducted using a higher order approach and compared against the reduced Fundamental Mistuning Model. For both cases, the first mode family is analyzed which is a bending mode for the cantilevered and a mixed bending-torsion mode for the shrouded bladed disk. An alternate mistuning pattern is implemented by proportionally scaling the Young's modulus of the structural finite element model. This allows taking into account the complete mistuning effects since all the perturbations including the eigenmode, frequency and aerodynamics are present in the flutter computations.

Using the higher order approach, it is shown that the effect of mistuning has less influence on the structurally strongly coupled system compared to the weakly coupled bladed disk. While the tuned results agree quite well between the higher order and reduced order approach, there are some noticeable differences for the mistuned bladed disk. Despite some quantitative differences, the Fundamental Mistuning Model correctly predicts the stabilizing trend with increasing mistuning amplitude of the cantilevered bladed disk. However, the reduced approach fails to qualitatively and quantitatively resemble the mistuned results of the higher order approach for the shrouded case.

DEUTSCHES ZENTRUM FÜR LUFT- UND RAUMFAHRT e.V.

Institut für Aeroelastik

Institutsleiter:

Prof. Dr.-Ing. Lorenz Tichy

Autor:

Dimitri Franz

Abteilungsleiter:

Dr. rer. nat. Holger Mai

Gruppenleiter:

Dr.-Ing. Joachim Belz

Mistuned Flutter Analysis of Strongly Coupled Bladed Disks in Conjunction with Reduced Order Modeling

Master Thesis

Graduation Studies conducted for obtaining the
Master's degree in Turbomachinery Aeromechanics (THRUST) by

Dimitri Franz

Faculty of Applied Sciences
University of Liège
Liège, Belgium

Academic Year
2016/2017

Abstract

Bladed disks are often analyzed under the assumption that the whole structure consists of perfectly identical substructures or sections. But real bladed disks exhibit small variations in geometry and material properties among the sectors. These differences, called mistuning, can have a large impact on the dynamic behavior and stability of the system.

A thorough review of reduced order models is performed for the description of the dynamic behavior of mistuned rotors. A flutter analysis for a mistuned cantilevered and shrouded bladed disk is conducted using a higher order approach and compared against the reduced Fundamental Mistuning Model. For both cases, the first mode family is analyzed which is a bending mode for the cantilevered and a mixed bending-torsion mode for the shrouded bladed disk. An alternate mistuning pattern is implemented by proportionally scaling the Young's modulus of the structural finite element model. This allows taking into account the complete mistuning effects since all the perturbations including the eigenmode, frequency and aerodynamics are present in the flutter computations. The cantilevered bladed disk model, representing a structurally weakly coupled system, is created by removing the cyclic symmetry boundary condition at the blade tip of the shrouded bladed disk.

Using the higher order approach, it is shown that the effect of mistuning has less influence on the structurally strongly coupled system compared to the weakly coupled bladed disk. A small mistuning level positively affects the cantilevered bladed disk. Further increase in mistuning stabilizes the system and the aerodynamic work becomes independent of the inter-sector phase angle. On the other hand, alternate mistuning of rotors with a high number of blades does not alter the eigenmodes of the shrouded bladed disk greatly enough, especially the lower nodal diameters. On the contrary, an unfavorable effect of alternate mistuning is observed which is seldom reported in the literature.

While the tuned results agree quite well between the higher order and reduced order approach, there are some noticeable differences for the mistuned bladed disk. Despite some quantitative differences, the Fundamental Mistuning Model correctly predicts the stabilizing trend with increasing mistuning amplitude of the cantilevered bladed disk. However, the reduced approach fails to qualitatively and quantitatively resemble the mistuned results of the higher order approach for the shrouded case.

Acknowledgements

The present Master thesis results from an internship at the Institute of Aeroelasticity of the German Aerospace Center DLR in Göttingen. At this point, I would like to thank for this great possibility and all the provided resources. I offer my sincerest gratitude to my supervisor Dr.-Ing. Joachim Belz for the thorough theoretical discussions and continuous motivation. Also special thanks goes to Markus Matthias who supported me in all matters throughout the work. Furthermore, I am very grateful to Michael Blocher and Christoph Reiber for their help regarding numerical issues. It was a pleasure to be part of this great turbomachinery group. Apart from that, many thanks go likewise to all my other DLR colleagues for proof-reading my thesis and all positive contributions.

In addition, I would also like to express many thanks to Dr. Nenad Glodic and Dr. Paul Petrie-Repar at the Royal Institute of Technology for their great support during the first year of my Master degree. Both of them gave me a great understanding about several aeroleastic problems so that I was prepared to write this Master thesis. The THRUST program was for me a whirlwind of learning but also a great time in which I met many good friends. I also would like to thank Prof. Ludovic Noels and my academic supervisor Prof. Greg Dimitriadis at the University of Liège for their assistance and critical reflections on my thesis.

Lastly, I see me very fortunate to have such great friends and family who greatly motivated me at every point of this thesis and especially in difficult time. When I needed a time-out, they always welcomed me with open arms and made me forget all troubles so that I could continue my thesis full of energy. I am quite sure that without them, I would never have finished this thesis as it is in its current form.

Contents

Nomenclature

Latin Symbols

$\hat{\mathbf{A}}_{\sigma_n}$	Mistuned aerodynamic influence coefficient matrix in traveling wave space	$N\,m$
$\mathbf{A}$	Tuned aerodynamic influence coefficient matrix	$N\,m$
A_0	Blade reference surface	m^2
A_{max}	Mistuning amplification factor	–
$\mathbf{C}$	Damping matrix	kg/s
$\mathbf{C}_x$	Nondimensional aerodynamic influence coefficient matrix	m
c	Blade choord	m
$\mathbf{E}$	Discrete Fourier transformation matrix	–
E_{kin}	Kinematic energy	J
$\vec{F}_c$	Aerodynamic coupling force vector	N
$\vec{F}_e$	External force vector	N
$\vec{F}_{aero}$	Aerodynamic force vector	N
$\vec{G}$	Generalized modal force	$N\,m$
h	Blade span	m
h_{FEM}	Harmonic number in FEM calculation	–
$\mathbf{I}$	Identity matrix	–
i	Blade or sector index	–
j	Imaginary unit	–
$\mathbf{K}$	Stiffness matrix	N/m
k	Running index	–
l	Running index	–
$\mathbf{M}$	Mass matrix	kg
m	Mass	kg
m^*	Reference mass for mode normalization	$kg\,m^2$
MAC	Modal assurance criterion	–
$\vec{n}$	Normal vector	–
N	Number of blades	–
n	Nodal diameter	–

n_{cycles}	Number of oscillation cycles	–
n_{eq}	Equivalent mistuned nodal diameter	–
$\hat{\mathbf{P}}$	Structural mistuning matrix	rad^2/s^2
P	Number of degrees of freedom	
p	Pressure at entry	Pa
p_1	Static pressure at entry	Pa
p_{01}	Total pressure at entry	Pa
$\vec{R}$	Residual vector containg the numerical flux variables	–
S	Number of bladed disk sectors in a finite element model	–
T	Oscillation period	s
t	Time	s
$\vec{q}$	Generalized displacement vector	–
$\vec{U}$	Vector of conservative flow variables	–
W_{aero}	Aerodynamic work	J
$\vec{x}$	Coordinate vector of the CFD mesh vertices	m
$\vec{x}$	Displacement vector in physical space	m
y^+	Wall distance coordinate	-

Greek Symbols

α	Angle	$^\circ$
$\vec{\hat{\alpha}}_{\sigma_n}$	Scaling vector in the CFD computations	–
$\vec{\beta}$	Vector of mistuning weighting factors	–
γ	Inter-sector phase angle	$^\circ$
$\Delta\mathbf{K}$	Mistuned stiffness matrix	N/m
$\Delta\mathbf{M}$	Mistuned mass matrix	kg
$\Delta\omega_{mis}$	Fractional change in frequency	–
$\Delta\tilde{\omega}_{mis}$	Discrete Fourier transformation of mistuning pattern	–
Δx	Time dependent quantity x	–
Δ	Relative difference	%
δ	Structural damping	rad/s
δ_a	Aeroelastic decay rate	rad/s
ζ	Aerodynamic damping	–
$\mathbf{\Theta}$	Eigenvector including all degrees of freedom associated to all nodal diameter and to a single blade mode shape in traveling wave space	m
θ	Circumferential position	$^\circ$

$\vec{\Theta}$	Eigenvector including all degrees of freedom associated to a single nodal diameter and to a single blade mode shape in traveling wave space	m
Λ	Logarithmic decrement	$-$
λ	Structural eigenvalue	rad/s
λ_a	Aeroelastic eigenvalue	rad/s
μ	Mass ratio	$-$
ϱ	Density	kg/m^3
σ_n	Inter-blade phase angle for n^{th} nodal diameter	$^\circ$
$\mathbf{\Phi}$	Eigenvector matrix of all degrees of freedom and all blade mode shapes for a single nodal diameter in physical space	m
ϕ	Mode shape of disk or blade dominated modes	$-$
$\mathbf{\Psi}$	Eigenvector including all degrees of freedom associated to all nodal diameter and to a single blade mode shape in physical space	m
$\vec{\Psi}$	Eigenvector including all degrees of freedom associated to a single nodal diameter and to a single blade mode shape in physical space	m
$\mathbf{\Omega}$	Structural frequency matrix	rad/s
ω	Angular structural frequency	rad/s
ω_a	Angular aeroelastic frequency	rad/s
$\tilde{\Omega}_{mis}$	Matrix of discrete Fourier transformations of mistuning pattern	$-$

Subscripts, Superscripts and Indices

0	Steady, time-independent quantity
0	Tuned quantity
b	Quantity of an averaged sector
c	Quantity associated to coupling
i	Quantity for the i^{th} blade or sector
k	Index indicating a row or column in a matrix
l	Index indicating a row or column in a matrix
min	Minimum value of a quantity
mis	Quantity subjected to mistuning
n	Quantity in traveling phase or associated to the n^{th} harmonic index
$norm$	Quantity used for normalization
x	Quantity in physical space
x, y, z	x, y, z component of a quantity
σ_n	Quantity accociated to the n^{th} nodal diameter

Acronyms

AIC	Aerodynamic Influence Coefficients
AMM	Asymptotic Mistuning Model
ANN	Artificial Neural Network
APT	Adaptive Perturbation Technique
CB	Craig-Bampton
CBSR	Craig-Bampton Substructure Reduction
CCM	Characteristic Constraint Modes
CFD	Computational Fluid Dynamics
CMM	Component Mode Mistuning
CMS	Component Mode Synthesis
CMS-HB	Component Mode Synthesis with Harmonic Balance method
CTA	Centro de Tecnologías Aeronauticas
DOF	Degree of Freedom
EROM	Exact Reduced Order Model
FE	Finite Element
FMM	Fundamental Mistuning Model
FUTURE	European project, Flutter Free Turbomachinery Blades
IBPA	Inter-Blade Phase Angle
ISPA	Inter-Sector Phase Angle
LPT	Low Pressure Turbine
MMDA	Multiple Modal Domain Analysis
ND	Nodal Diameter
NNMA	Non-Nominal Mode Approach
RANS	Reynolds Averaged Navier-Stokes
REDUCE	Reduced Order Model proposed by Castanier et al.
ROM	Reduced Order Model
RT	Receptance Technique
SMART	Secondary Modal Analysis Reduction Technique
SNM	Subset of Nominal Modes
TW	Traveling Wave
URANS	Unsteady Reynolds Averaged Navier-Stokes

Symbols

$\ddot{x}$	Acceleration
$\hat{x}$	Amplitude of a quantity

$\overline{\vec{x}}$	Complex conjugate of a vector
$\tilde{x}$	Discrete Fourier transformation of a quantity
$\mathbf{E}^H$	Hermitian transpose of a matrix
$\Im$	Imaginary part of a quantity
$\otimes$	Kronecker product
$\Re$	Real part of a quantity
$\dot{x}$	Time derivative of a quantity, velocity
$\mathbf{E}^T$	Transpose of a matrix

1 Introduction

1.1 General Background

In the development of aero engines and stationary turbines, a trend towards lighter and heavily loaded stages can be observed. Reducing the weight of bladed disks brings the eigenmodes closer together which even might result in the interaction of different mode families. For that reason, the aeroelastic design becomes more challenging and an accurate prediction of the flutter stability is necessary.

The analysis of the structural dynamic properties of nominally cyclic structures such as bladed disks is often done under the assumption that the whole structure consists of perfectly identical substructures or sections. But it has been shown that the dynamic behavior of a bladed disk is highly sensitive to small variations in geometry and material properties among the sectors which are caused, for instance, by manufacturing tolerance, material defects or uneven wear. These differences, called mistuning, can have a large impact on the dynamic behavior and aeroelastic stability of the system, leading to a response which is quantitatively different from an ideally tuned structure.

In order to describe the dynamic behavior of mistuned structures, some approaches were developed in the last decades such as different reduced order models or the power-flow procedure which performs a probabilistic distribution of mistuning. Most of them are designed for small imperfections and under the assumption that the structure vibrates in the same manner, i.e. equal mode shapes, and are only structurally coupled through an almost perfectly rigid disk. However, blades are also often coupled by a connection along the span, known as shroud or interlock, or by a flexible disk which is the case for disks with a large diameter. While the former coupling is implemented in fans or low-pressure turbine of aero engine, the latter one is usually observed in the low-pressure turbine of larger aero engines or steam turbines. The greater structural coupling makes the analysis more difficult since it results in a great variation of frequencies and complex eigenmodes.

This work is performed at the Institute of Aeroelasticity of the German Aerospace Center (DLR) in Göttingen, Germany. The institute is specialized in the experimental and numerical aeroelastic analysis of air planes, wind turbines, helicopters as well as aero engines.

1.2 Motivation

The majority of recent mistuning studies focuses on the analysis of weakly coupled or uncoupled systems. A large part of today's bladed disks and blisks are weakly coupled systems but a non-

negligible fraction of structurally strongly coupled bladed disks are present. A stronger coupling is often introduced in aero engines or stationary turbines in order to enhance the stability of the system. In consequence, a thorough consideration of mistuned strongly coupled bladed disks is crucial and therefore the procedure for the stability analysis of mistuned bladed disks but also the related issues are addressed within this thesis.

The aim of the thesis can be stated by establishing four key questions or points which are as following:

1. Which reduced order model (ROM) is suitable for modeling mistuned bladed disks with different levels of coupling? A detailed overview of currently available ROMs should be created and compared against each other using adequate criteria. Such an overview would be beneficial for further analyses within the framework of the DLR Institute of Aeroelasticity to intensify the studies in the area of mistuning. The review should emphasize whether the listed ROMs are able to model shrouded bladed disks.

2. Using the overview, select one reduced order model and apply it on the case of study. In addition, perform several structural and aeroelastic computations to identify the differences in the

   (a) modal properties

   (b) stability of the aeroelastic system

   between the ROM and the higher accuracy numerical method depending on the level of coupling.

3. Is the current process chain suitable for the analysis of structurally strongly coupled bladed disks? If it is not, update the process chain by implementing new pre- and post-processing steps. Conceive and create an aeroleastic model which is able to analyze alternate mistuned bladed disks.

4. Does the selected ROM correctly represent the modal characteristics and the aerodynamic damping of the system? If it does not, explain why and if necessary conduct further calculations which help to discuss the results. Make conclusions and give recommendations on applying the selected ROM for structurally strongly coupled bladed disk.

Lastly, it should be noted that within this thesis, the term coupling does not refer to the numerical coupling of a fluid-structure interaction but to the structural coupling of the bladed disk which occurs due to the connection of the blades through the disk or at the shroud interface.

2 Terminology and Vibration Characteristics of Tuned Configurations

Aeroelasticity or fluid-structure interaction explores the interdependency between inertia, elastic and aerodynamic forces. There are two major distinctions in the study of aeroelasticity which are self-excited (flutter) and forced vibration (forced response). This chapter describes general characteristics of tuned blade vibration and highlights important aspects of self-excited structures subjected to flutter. A detailed discussion of the forced response theory is out of scope for this thesis.

2.1 General Vibration Characteristics and Terminology

The vibration of a rotor can be characterized by the amount of strain energy presented in the disk and blade [1]. Therefore, the analysis is distinguished between disk or blade dominated modes and coupled vibrations.

Disk dominated vibration, where the greater part of the strain energy is stored in the disk, can be simplified through a quasi-axisymmetric model. The vibration of the structure is defined by the disk mode shape while the blades simply follow the deflection and are approximated by point masses fixed at the outer rim. The circumferential mode shapes of such disk-like systems can be expressed by [2]

$$\phi(\theta) = \hat{\phi}\cos(n\theta + \alpha) \tag{2.1}$$

where n is the harmonic index or nodal diameter (ND) and refers to the number of circumferential lines along the diameter where the displacement is zero, θ the circumferential position and α a fixed reference angle.

When the disk is mostly rigid and the strain energy is predominantly located in the blades, the blades can be modeled as beam-like structures. For such structures, the blade vibration can be decomposed in flex/bending, torsion, edge-wise modes or combinations of those, see Fig. 2.1.

Although the disk is mostly rigid, the blades are coupled through the disk and the response of the whole system has to be taken into account. In contrast to a quasi-axisymmetric model for which the maximum number of nodal diameters is infinite, bladed disks being cyclic symmetric structures have

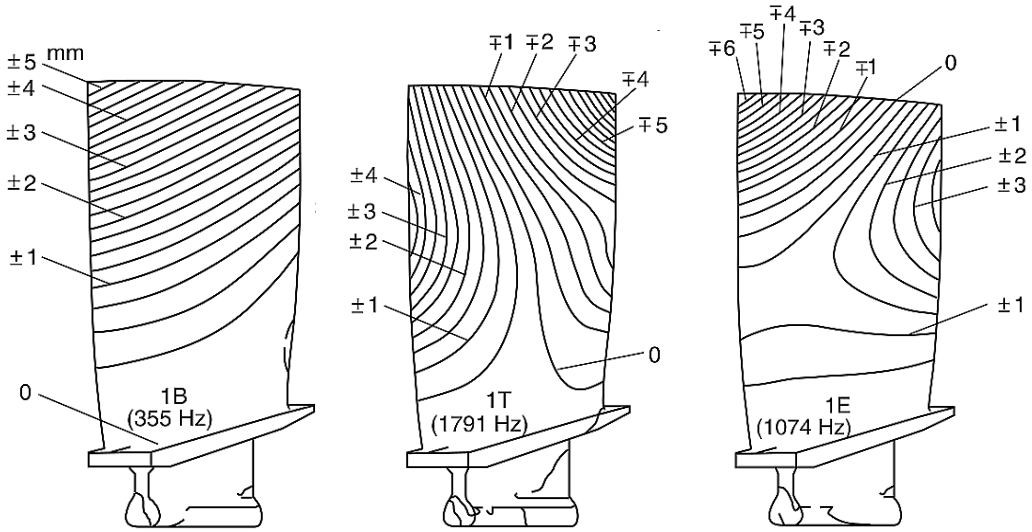

(a) First Flex (1F) **(b)** First Torsion (1T) **(c)** First Edgewise (1E)

Figure 2.1: Cantilever Blade Mode Shapes with Displacement Contour [3]

a finite number of nodal diameter n which is related to the number of blades N by

$$\begin{aligned} n_{max} &= \frac{N}{2} && \text{if } N \text{ is even} \\ n_{max} &= \frac{N-1}{2} && \text{if } N \text{ is odd.} \end{aligned} \tag{2.2}$$

The combination of disk and blade mode shapes describes the modes of the entire system in terms of traveling waves

$$\phi_{i,n} = \hat{\phi}_{i,n} e^{j\sigma_n i} \tag{2.3}$$

where i is the sector index of the bladed disk and σ_n is the inter-blade phase angle for the n^{th} harmonic or nodal diameter:

$$\sigma_n = \frac{2\pi n}{N} \tag{2.4}$$

The inter-blade phase angle introduces the concept of traveling waves. Mode shapes of an entire structure can either be real or complex. While complex modes are better described with traveling waves, real mode shapes can be considered as standing waves. Real mode shapes occur for $n = 0$ (in-phase motion of blades) and $n = n_{max}$ (out-of-phase motion of blades), compare Eq. (2.2). The maximum displacement of each blade is reached at the same instant of time for a real mode shape and analogously, all blades simultaneously pass through the zero deflection position. In case of a complex mode shape, each part of the structure has not only its own amplitude but also its own phase. For such tuned complex mode shapes, a pair of nodal diameter corresponding to the same frequency can rotate in opposite directions and therefore, a forward and backward traveling wave can be established. A combination of a forward (positive nodal diameter) and backward traveling wave (negative nodal diameter) belonging to the same harmonic index is referred to a double mode and is a characteristic

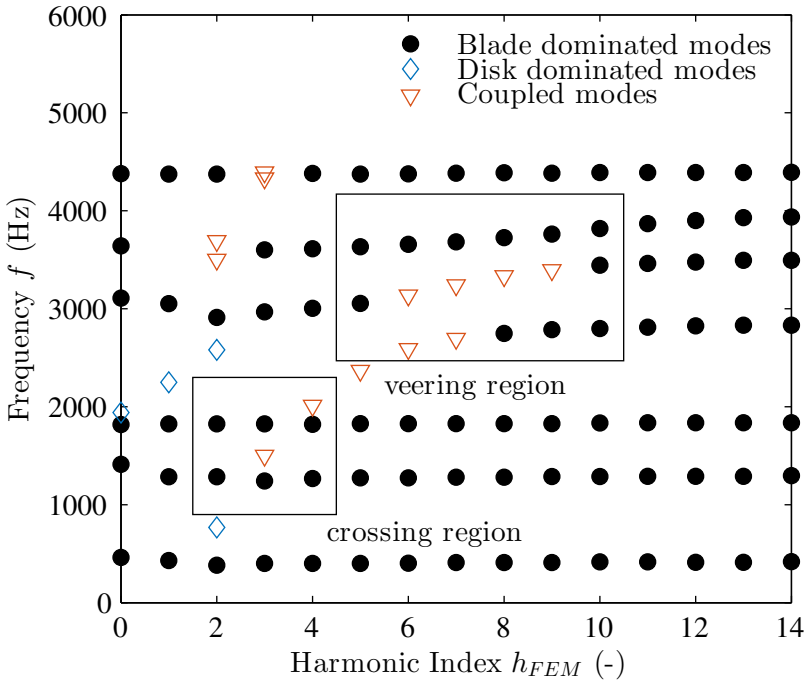

Figure 2.2: Natural Frequencies for Different Nodal Diameter of a High Pressure Compressor Blisk with Veering and Crossing Regions [1]

of cyclic symmetric structures. The response of a tuned cyclic symmetric system is harmonic so that the motion of each blade i has the form of

$$u(t)_{i,n} = \Re\left\{\hat{\phi}_{i,n} e^{j(\omega t + i\sigma_n)}\right\} = \hat{\phi}_{i,n}\left\{\cos(i\sigma_n)\cos(\omega t) - \sin(i\sigma_n)\sin(\omega t)\right\}. \tag{2.5}$$

Blade disk modes with the same type of blade deflection, e.g. flex or torsion mode, but with different inter-blade-phase angles can be grouped to a mode family.

When the major part of the vibration energy is in the blade and yet, a non-negligible fraction is located in the disk, coupled vibration occurs. There are two phenomena to distinguish in the context of coupled vibration which are frequency veering of blade modes and frequency crossing of blade and disk modes, see Fig. 2.2. In the frequency veering region, two natural frequencies of the blade are close enough in a limited range of a harmonic index which might lead to a coupled response consisting of this two blade modes. Frequency crossing appears when both blade and disk contribute to the deflection of the bladed disk. The overall deflection is a superposition of a blade mode shape and a considerable rigid body motion of the disk. [4]

2.2 Flutter of Coupled Bladed Disks

Flutter is a self-induced excitation where one of the system eigenmodes experiences a self-excitation due to unfavorable (negative) aerodynamic damping which leads to an unstable condition. The equation of motion for a tuned, discretized bladed disk with P degrees of freedom per sector and N sectors in

the assembly in its general form is given by

$$\mathbf{M}\ddot{\vec{x}} + \mathbf{C}\dot{\vec{x}} + \mathbf{K}\vec{x} = \vec{F}_{aero} = \vec{F}_c(\vec{x}, \dot{\vec{x}}) + \vec{F}_e \tag{2.6}$$

where the left-hand side reflects the structural forces with $\mathbf{M}$ being the mass, $\mathbf{K}$ the stiffness matrix, both symmetric and positive definite, and $\mathbf{C}$ the structural damping. On the right hand side, the aerodynamic force can be divided into coupled aerodynamic forces due to blade motion $\vec{F}_c$ and external forces $\vec{F}_e$. The exact value of structural damping is difficult to estimate and in many cases not known. Therefore, the damping matrix $\mathbf{C}$ is dropped in the further derivation which can be seen as a conservative approach because structural damping always acts in a stabilizing manner. If the displacement vector $\vec{x}$ is partitioned in such a way that the individual vectors $\vec{x}_i$ contain the displacement of P degrees of freedom of each corresponding sector

$$\vec{x} = (\vec{x}_1^T, \vec{x}_2^T, \ldots, \vec{x}_N^T)^T \,, \tag{2.7}$$

the mass and stiffness matrices get circulant and Eq. (2.6) becomes

$$\begin{bmatrix} \mathbf{M}_i & \mathbf{M}_{i,c} & 0 & \ldots & \mathbf{M}_{i,c}^T \\ \mathbf{M}_{i,c}^T & \mathbf{M}_i & \mathbf{M}_{i,c} & \ldots & 0 \\ 0 & \mathbf{M}_{i,c}^T & \mathbf{M}_i & \ldots & 0 \\ \vdots & \vdots & \vdots & \ddots & \vdots \\ \mathbf{M}_{i,c} & 0 & 0 & \ldots & \mathbf{M}_i \end{bmatrix} \begin{Bmatrix} \ddot{\vec{x}}_1 \\ \ddot{\vec{x}}_2 \\ \ddot{\vec{x}}_3 \\ \vdots \\ \ddot{\vec{x}}_N \end{Bmatrix} + \begin{bmatrix} \mathbf{K}_i & \mathbf{K}_{i,c} & 0 & \ldots & \mathbf{K}_{i,c}^T \\ \mathbf{K}_{i,c}^T & \mathbf{K}_i & \mathbf{K}_{i,c} & \ldots & 0 \\ 0 & \mathbf{K}_{i,c}^T & \mathbf{K}_i & \ldots & 0 \\ \vdots & \vdots & \vdots & \ddots & \vdots \\ \mathbf{K}_{i,c} & 0 & 0 & \ldots & \mathbf{K}_i \end{bmatrix} \begin{Bmatrix} \vec{x}_1 \\ \vec{x}_2 \\ \vec{x}_3 \\ \vdots \\ \vec{x}_N \end{Bmatrix} = \begin{Bmatrix} \vec{F}_{1,c} + \vec{F}_{1,e} \\ \vec{F}_{2,c} + \vec{F}_{2,e} \\ \vec{F}_{3,c} + \vec{F}_{3,e} \\ \vdots \\ \vec{F}_{N,c} + \vec{F}_{N,e} \end{Bmatrix} \tag{2.8}$$

where $\mathbf{M}_i$ and $\mathbf{K}_i$ are the mass and stiffness matrix of the individual sector each of the size $P \times P$ and $\mathbf{M}_{c,i}$ and $\mathbf{K}_{c,i}$ the coupling mass and stiffness matrix due to structural coupling, i.e. coupling through the disk or the shroud. It should be noted here that the subscript for the sector i in Eq. (2.8) can be chosen arbitrarily since each tuned sector has the same mass and stiffness.

To form an eigenvalue problem, the aerodynamic forces are set to zero and the solution is assumed to be of complex exponential form

$$\vec{x} = \hat{\vec{x}} e^{\lambda_n t} \,. \tag{2.9}$$

In general, the eigenvalue for the n^{th} harmonic $\lambda_n = -\delta + j\omega_n$ consists of the structural damping δ (set to zero) and natural frequency of the structure ω_n. The coupled eigenvalue problem can be established

$$|\mathbf{K} - \lambda_n^2 \mathbf{M}|\hat{\vec{x}} = \vec{0} \tag{2.10}$$

and the eigenvalues and eigenvectors (mode shapes) extracted by using for example the finite element (FE) approach.

However, the cyclic symmetric property of turbomachinery bladed disks is evident in Eq. (2.8) in terms of its block circulant nature where the mass and stiffness matrices are composed of a sector repeated N times along the diagonal. Therefore, based on this periodical behavior, it is convenient to use Lane's theorem which says that the response of a cyclic structure appears in traveling waves

with blades reaching the same amplitude but lagged by a constant inter-blade phase angle [5]. This property allows to rewrite Eq. (2.7) so that the degrees of freedom are drastically reduced from the size $N \times P$ to $1 \times P$. One possible eigenvector $\vec{\Psi}_n$ for all DOFs associated to the n^{th} nodal diameter is

$$\vec{\hat{x}}_n = \begin{Bmatrix} \vec{\Psi}_{0,n} \\ \vec{\Psi}_{1,n} \\ \vdots \\ \vec{\Psi}_{N-1,n} \end{Bmatrix} = \begin{Bmatrix} \vec{\Psi}_{0,n} e^{i\sigma_n 0} \\ \vec{\Psi}_{0,n} e^{i\sigma_n 1} \\ \vdots \\ \vec{\Psi}_{0,n} e^{i\sigma_n (N-1)} \end{Bmatrix} \quad \text{for } n = 0, ..., n_{max} \tag{2.11}$$

which is in general complex and rotates around the annulus with a constant angular velocity ω/n. $\vec{\Psi}_{0,n}$ is the eigenform of the first sector or the reference sector of the size P and can be regarded as the n^{th} mode of the discrete Fourier transform of the N periodic sequence for all the degrees of freedom along the complete assembly $(\vec{\Psi}_0, \ldots, \vec{\Psi}_{N-1})$. Apart from reducing the model size, this approach has another advantage which is that it splits the coupled eigenvalue problem, Eq. (2.10), into N decoupled eigenvalue problems of size P [6]:

$$|(\mathbf{K}_c - \lambda_n^2 \mathbf{M}_c) e^{i\sigma_n} + (\mathbf{K}_c - \lambda_n^2 \mathbf{M}_c)^T e^{-i\sigma_n} + \mathbf{K} - \lambda^2 \mathbf{M}| = \vec{0}\,. \tag{2.12}$$

Solving Eq. (2.12) gives P real eigenvalues $\omega_{n,1}^2, \ldots, \omega_{n,P}^2$ representing the squared angular oscillation frequency of the structure and the corresponding mode shapes for each nodal diameter. The mode shapes can be typical blade modes, e.g. bending or torsion modes, but also disk-dominated modes or any coupled combinations of these, e.g. bending-torsion modes. When the eigenmodes of each decoupled eigenvalue problem are arranged for a given nodal diameter in such a way that the columns are the displacements of all mode shapes for each degree of freedom

$$\mathbf{\Phi}_n = \left[\vec{\Phi}_{n,1}, \vec{\Phi}_{n,2}, \ldots, \vec{\Phi}_{n,P}\right] \tag{2.13}$$

and are normalized with respect to mass, the orthogonality property can be used and following relations stated

$$\mathbf{\Phi}_n^H (\mathbf{M}_c e^{i\sigma_n} + \mathbf{M}_c^T e^{-i\sigma_n} + \mathbf{M}) \mathbf{\Phi}_n = m^* \mathbf{I} \tag{2.14}$$

and

$$\mathbf{\Phi}_n^H (\mathbf{K}_c e^{i\sigma_n} + \mathbf{K}_c^T e^{-i\sigma_n} + \mathbf{K}) \mathbf{\Phi}_n = m^* \mathbf{\Omega}_n^2 = m^* \begin{bmatrix} \omega_{n,1}^2 & \ldots & 0 \\ \vdots & \ddots & \vdots \\ 0 & \ldots & \omega_{n,P}^2 \end{bmatrix} \tag{2.15}$$

where $\mathbf{I}$ is the identity matrix, $\mathbf{\Omega}_n$ a diagonal matrix with the structural frequencies as the entries, $\mathbf{\Phi}_n^H$ the Hermitian of the mode shape matrix. m^* is a reference mass for the eigenvector normalization which usually is the modal mass and equals to $1\,kg\,m^2$ or $1\,t\,mm^2$. The eigenproblem of Eq. (2.12) remains invariant for a given pair of traveling waves, i.e. forward $\vec{\Theta}_n$ and backward traveling wave $\bar{\vec{\Theta}}_n$,

under the following conditions:

$$-n \rightarrow +n \tag{2.16}$$

$$\omega_n^2 \rightarrow \omega_{-n}^2 = \omega_n^2 \tag{2.17}$$

$$\vec{\Theta}_n \rightarrow \bar{\vec{\Theta}}_n \,. \tag{2.18}$$

This implies that there always are traveling wave modes which appear as counter propagating pairs excluding the standing waves with the 0^{th} nodal diameter and the maximum one. The behavior can be directly seen from Eq. (2.9) which remains unchanged after time is reversed $t \rightarrow -t$ since it does not exhibit any dissipation [6]. In the course of this, a backward traveling wave is the complex conjugate of the forward traveling wave.

$$\vec{\Theta}_{n,backward} = \overline{\vec{\Theta}}_{n,forward} = \overline{\Re\{\vec{\Theta}_n\} + j\Im\{\vec{\Theta}_n\}} = \Re\{\vec{\Theta}_n\} - j\Im\{\vec{\Theta}_n\} \tag{2.19}$$

Standing waves are non-propagating and consist only of a real part.

To consider the aerodynamics, the spatial part of the displacement vector $\vec{x}$ in Eq. (2.9) is projected on all harmonics of the traveling wave basis. In addition, applying the Lagrangian principle on the projected space of $\vec{\hat{x}}$, the following change of variables to the traveling wave space can be established for one particular blade mode

$$\vec{\hat{x}} = \frac{1}{\sqrt{N}} \begin{bmatrix} \vec{\Psi}_{n=0}\, e^{j\frac{2\pi 0^2}{N}} & \vec{\Psi}_{n=1}\, e^{j\frac{2\pi 0\cdot 1}{N}} & \dots & \vec{\Psi}_{n=N-1}\, e^{j\frac{2\pi 0(N-1)}{N}} \\ \vec{\Psi}_{n=0}\, e^{j\frac{2\pi 1\cdot 0}{N}} & \vec{\Psi}_{n=1}\, e^{j\frac{2\pi 1^2}{N}} & \dots & \vec{\Psi}_{n=N-1}\, e^{j\frac{2\pi 1(N-1)}{N}} \\ \vdots & \vdots & & \vdots \\ \vec{\Psi}_{n=0}\, e^{j\frac{2\pi k0}{N}} & \vec{\Psi}_{n=1}\, e^{j\frac{2\pi k1}{N}} & \dots & \vec{\Psi}_{n=N-1}\, e^{j\frac{2\pi k(N-1)}{N}} \\ \vdots & \vdots & & \vdots \\ \vec{\Psi}_{n=0}\, e^{j\frac{2\pi (N-1)0}{N}} & \vec{\Psi}_{n=1}\, e^{j\frac{2\pi (N-1)1}{N}} & \dots & \vec{\Psi}_{n=N-1}\, e^{j\frac{2\pi (N-1)(N-1)}{N}} \end{bmatrix} \vec{\hat{q}}_{\sigma_n} \tag{2.20}$$

with $\vec{\Psi}_{n=0}$ being the eigenform of the reference sector for the 0^{th} nodal diameter and $\vec{\Psi}_{n=N-1}$ being the eigenvector for the maximum harmonic n_{max} of the reference sector while both are standing waves. In between these two eigenvectors are the traveling waves consisting of a complex eigenform and its complex conjugate part according to Eq. (2.19). $\vec{\hat{u}}$ is the generalized coordinate representing the amplitudes of all sectors for different traveling wave modes

$$\vec{\hat{q}}_{\sigma_n} = (\vec{\hat{q}}^T_{\sigma_n,1}, \vec{\hat{q}}^T_{\sigma_n,2}, \dots, \vec{\hat{q}}^T_{\sigma_n,i}, \dots, \vec{\hat{q}}^T_{\sigma_n,N})^T \,. \tag{2.21}$$

It can be noted that the generalized coordinate $\vec{\hat{u}}$ in Eq. (2.21) is expressed in a general form which means that the subentries of $\vec{\hat{u}}$ are itself vectors. The subvectors can have only one entry as in Eqn. (2.20) and Eq. (2.23) or P entries as in Eq. (2.24). The external forces $\vec{F}_e$ can be dropped, since they are of no importance for the determination of flutter. As can be deduced from Eq. (2.20), the projection basis for the transformation is the discrete Fourier transformation matrix $\mathbf{E}$ [7] (with $1/\sqrt{N}$

as a normalization factor):

$$E_{n,i} = \frac{1}{\sqrt{N}} e_{ni} = \frac{1}{\sqrt{N}} e^{j\frac{2\pi ni}{N}} \quad \text{for } i, n = 0, 1, ..., N-1\,. \tag{2.22}$$

Finally, Eq. (2.20) can be rewritten in a compact form

$$\vec{\hat{x}} = (\mathbf{E} \otimes \mathbf{I})\mathbf{\Psi}\vec{\hat{u}}_{\sigma_n} = \mathbf{\Theta}\vec{\hat{u}}_{\sigma_n}\,. \tag{2.23}$$

Following this methodology and applying the orthogonality as before, a generalized equation of motion including the aerodynamic coupling forces is established

$$m^* \begin{bmatrix} \mathbf{\Omega}_1^2 - \lambda^2\mathbf{I} & \dots & \mathbf{0} \\ \vdots & \ddots & \vdots \\ \mathbf{0} & \dots & \mathbf{\Omega}_N^2 - \lambda^2\mathbf{I} \end{bmatrix} \begin{Bmatrix} \vec{\hat{q}}_{\sigma_n,1} \\ \vdots \\ \vec{\hat{q}}_{\sigma_n,N} \end{Bmatrix} = \mathbf{\Theta}^H \vec{\hat{F}}_c = \vec{\hat{G}}_{\sigma_n} \tag{2.24}$$

with diagonal normalized mass $\mathbf{I}$ and stiffness matrices $\mathbf{\Omega}_i^2$ for each sector i calculated as shown in Eqn. (2.14) and (2.15) respectively and a block diagonal generalized modal force matrix $\vec{G}_{\sigma_n}$ in traveling wave space.

Assuming small flow perturbations due to the blade vibration, the coupling force $\vec{F}_{c,i}$ in physical space can be expressed as a linear superposition [8]. In such a case, the total unsteady response of the i^{th} blade is governed by the the displacement of the i^{th} blade itself and by the other blades lagged by the respective multiple of the inter-blade phase angles [9]. Therefore, the coupling force acting on blade i can be decomposed according to

$$\vec{F}_{c,i}(t) = \vec{F}_{c,0}\Big(\vec{x}_0(t), \dot{\vec{x}}_0(t), \ddot{\vec{x}}_0(t)\Big) + \vec{F}_{c,1}\Big(\vec{x}_0(t), \dot{\vec{x}}_0(t), \ddot{\vec{x}}_0(t)\Big) + \vec{F}_{c,N-1}\Big(\vec{x}_0(t), \dot{\vec{x}}_0(t), \ddot{\vec{x}}_0(t)\Big) + \dots\,. \tag{2.25}$$

From a physical perspective, Eq. (2.25) above describes the unsteady forces due to a flow perturbation induced by the displaced blade i on the blade i itself and all its neighboring blades on the suction and pressure side respectively. The induced forces for the whole assembly can be rewritten in terms of non-dimensional aerodynamic influence coefficients (AIC) as

$$\vec{G}_x = \mathbf{\Psi}\vec{F}_c = (p_{01} - p_1)A_0\mathbf{C}_x\vec{\hat{q}}_x \tag{2.26}$$

where $\mathbf{C}_x$ is the non-dimensional aerodynamic influence coefficients matrix containing complex entries, $(p_{01} - p_1)$ is the reference dynamic head and A_0 the blade surface at the blade row inlet, respectively. $\vec{\hat{q}}_x$ is the generalized coordinate in physical space and $\mathbf{\Psi}$ contains all mass-normalized eigenvectors while both result from the decoupling of the displacement vector according to the Lagrangian principle in the physical space.

It should be pointed out here that the non-dimensional aerodynamic influence coefficients actually have the dimension unit length. The matrix $\mathbf{C}_x$ is circulant but non-symmetric due to different influences on the suction and pressure side. The subscript x indicates the definition of the AIC in the

physical, modal space. It has been shown that the influence coefficients decrease in order of magnitude by increasing distance, e.g. $C_{0,x}$ is of one magnitude greater than $C_{1,x}$ and $C_{N-1,x}$ [8–10]. Therefore, the consideration of 7 blades is usually enough for a relativly accurate representation of the system. It can be noted here that due to the linearity of the superposition, not only fluid forces of a single mode shape can be taken into account but also several different mode shapes which are called intermode influence coefficients.

In a similar manner, the generalized force $\vec{\hat{G}}_{\sigma_n}$ in traveling wave (TW) space is determined by

$$\vec{\hat{G}}_{\sigma_n} = (p_{01} - p_1) A_0 \mathbf{C}_{\sigma_n} \vec{\hat{u}} = \mathbf{A}_{\sigma_n} \vec{\hat{q}}_{\sigma_n} \ , \tag{2.27}$$

$\mathbf{A}_{\sigma_n}$ being the dimension assigned aerodynamic influence coefficient matrix. Using this projection of the AICs from physical to the traveling wave space and inserting Eq. (2.27) into Eq. (2.24) leads to the aeroelastic eigenvalue problem in TW space

$$\begin{bmatrix} m^* \mathbf{\Omega}_1^2 - \lambda^2 \mathbf{I} & \dots & \mathbf{0} \\ \vdots & \ddots & \vdots \\ \mathbf{0} & \dots & \mathbf{\Omega}_N^2 - \lambda^2 \mathbf{I} \end{bmatrix} \begin{Bmatrix} \vec{\hat{q}}_{\sigma_n,1} \\ \vdots \\ \vec{\hat{q}}_{\sigma_n,N} \end{Bmatrix} = \mathbf{A}_{\sigma_n} \vec{\hat{q}}_{\sigma_n} \tag{2.28}$$

with the block diagonal aerodynamic influence coefficient matrix

$$\mathbf{A}_{\sigma_n} = \begin{bmatrix} \mathbf{A}_{1,\sigma_n} & \dots & \mathbf{0} \\ \vdots & \ddots & \vdots \\ \mathbf{0} & \dots & \mathbf{A}_{N,\sigma_n} \end{bmatrix} . \tag{2.29}$$

The aerodynamic influence coefficient matrices $\mathbf{A}_{\sigma_n}$ can be transformed from TW to physical space by

$$\mathbf{A}_x = \mathbf{E} \mathbf{A}_{\sigma_n} \mathbf{E}^H . \tag{2.30}$$

Alternatively, the individual subentries of the AIC matrix are transformed by

$$A_{i,x} = \frac{1}{N} \sum_{n=0}^{N-1} \mathbf{A}_{i,\sigma_n} e^{j \frac{2\pi i n}{N}} \tag{2.31}$$

or backwards by

$$A_{i,\sigma_n} = \sum_{i=0}^{N-1} \mathbf{A}_{i,x} e^{-j \frac{2\pi i n}{N}} . \tag{2.32}$$

Eventually, the eigenproblem can be rewritten in a more compact form

$$m^* \left| \begin{bmatrix} \mathbf{\Omega}_1^2 - \lambda^2 \mathbf{I} - \mathbf{A}_{1,\sigma_n}/m^* & \dots & \mathbf{0} \\ \vdots & \ddots & \vdots \\ \mathbf{0} & \dots & \mathbf{\Omega}_N^2 - \lambda^2 \mathbf{I} - \mathbf{A}_{N,\sigma_n}/m^* \end{bmatrix} \right| \begin{Bmatrix} \vec{\hat{q}}_{\sigma_n,1} \\ \vdots \\ \vec{\hat{u}}_{\sigma_n,N} \end{Bmatrix} = \mathbf{0} \tag{2.33}$$

where the eigenvalues of each sector can be determined separately with the aeroelastic eigenvalues

$$\lambda_{a,\sigma_n} = -\delta_{a,\sigma_n} + j\omega_{a,\sigma_n} \,. \tag{2.34}$$

The solution of the eigenvalue problem gives the aeroelastic eigenvalues and the aerodynamic damping ζ_{σ_n} can be calculated from the critical damping ratio by taking the ratio of the aeroelastic decay rate δ_{a,σ_n} to the undamped structural frequency ω_{σ_n} or approximated by the real and the imaginary part of the eigenvalue λ_{a,σ_n}:

$$\zeta_{\sigma_n} = \frac{1}{2\pi}\frac{\delta_{a,\sigma_n}}{\omega_{\sigma_n}} \approx -\frac{1}{2\pi}\frac{\Re(\lambda_{a,\sigma_n})}{\Im(\lambda_{a,\sigma_n})} \,. \tag{2.35}$$

The system is aerodynamically unstable if the aerodynamic damping is negative and flutter occurs.

2.3 Flutter Methodologies

There are three main methodologies which allows the prediction of flutter. The first method is the usage of bidirectionally coupled simulations. The equations of motion are solved in the time domain coupled to the aerodynamic forces which are calculated by a CFD solver. The strength of the coupling can be divided into weak or explicit coupling where data exchange occurs only once per time step, and strong or implicit coupling where the data is exchanged iteratively until an equilibrium state is accomplished at each iteration step [4]. The aerodynamic damping can be retrieved from the displacement versus time curves using the logarithmic decrement method

$$\Lambda = \frac{1}{n_{cycles}} \ln \frac{x(t)_{max}}{x(t + n_{cycles}T)_{max}} = \frac{2\pi\zeta}{\sqrt{1-\zeta^2}} \tag{2.36}$$

where $x(t)_{max}$ is the amplitude at a given time t and $x(t+n_{cycles}T)_{max}$ the amplitude shifted by $n_{cycles}T$ from the given time with n_{cycles} being the number of cycles and T the period of one oscillation. The main advantage of bidirectionally coupled simulations is that it captures all non-linearities in the flow field. However, the drawback is the immense demand for computational resources.

The second methodology is the energy method developed by Carta that takes into account the high mass ratio μ of turbomachinery blades

$$\mu = \frac{2m_{blade}}{\varrho h c^2} \tag{2.37}$$

which relates the representative fluid volume that is set in motion by the blade oscillation to the blade mass [11]. The practical implementation of it is the decoupling of the structural equation of motion and the fluid forces resulting into a unidirectional aeroelastic problem. Hence, it implies that the structural forces dominate and the unsteady aerodynamic forces do not alter structural deformation including the structural frequencies. Assuming that aeroelastic modes are traveling wave modes, the unsteady flow response can be determined for each TWM by CFD analysis where the blade motion is prescribed to be a structural mode shape. The aerodynamic work done by the fluid on the blade signifies a potential flutter problem. The logarithmic decrement is related to the aerodynamic damping

by

$$\Lambda = \frac{-W_{aero}}{2E_{kin,max}} \tag{2.38}$$

where W_{aero} is the unsteady aerodynamic work per cycle and $E_{kin,max}$ the maximum kinetic energy of the blade. The mass ratio of airplane wings is much lower compared to turbomachinery blades and therefore, the energy method is not directly applicable.

The third method is a direct method which directly solves the aeroelastic eigenvalue problem in traveling wave space, Eq. (2.33), or in physical space. The order of the matrices can be of the size of the degree of freedoms of the aeroelastic model. However, since the aerodynamic influence coefficients matrix is non-symmetric in the physical space, the computational time of the eigenvalue solver is high. Therefore, it is advisable to determine the aeroelastic eigenvalue in the TW space. Nonetheless, the computational effort might still be high due to large matrices sizes. Hence, if the number of DOFs can be reduced by a system approach, a more efficient reduced order model can be established. To solve the equation of motion, aerodynamic influence coefficients are required which can be determined through unsteady CFD calculations and the procedure is elaborated in the following section.

2.4 Computation of Aerodynamic Influence Coefficients

In general, the aerodynamic work can act in a stabilizing or destabilizing manner. If the structural damping is relatively low, for instance for integrally bladed disks which are also knowns as blisks, the exact calculation of the aerodynamic work is crucial to determine the aeroelastic stability of a system.

For the sake of simplicity, the derivation of the aerodynamic influence coefficients will be performed for a disk sector represented solely by a single-degree of freedom system. The calculation can easily be extended for a discretized system with P degree of freedom per sector and an indication will be given where the main difference is.

The aerodynamic work W_{aero} on the i^{th} blade is defined by the dot product between the coupled aerodynamic force $\vec{F_i}, c$ acting on the blade and the displacement $\vec{x_i}$. A positive work ($W_{aero,i} > 0$) symbolizes an energy transfer from the fluid to the structure indicating an unstable system. In case of a negative work ($W_{aero,i} < 0$) in contrast, the blade releases energy and therefore, an oscillation will be damped. Since the blade undergoes a periodic oscillation, the net work has to be integrated over one period

$$W_{aero,i} = \int_0^T \vec{F}_{i,c}(t) \cdot \dot{\vec{x}}_i(t)\, dt\,. \tag{2.39}$$

Projecting the displacement $\vec{x}_i$ on the generalized, traveling wave domain as done previously

$$\vec{x}_i(t) = \Re\Big\{\mathbf{E}\mathbf{\Psi}\vec{u}(t)\Big\} = \Re\Big\{\mathbf{\Theta}\vec{\hat{u}}e^{j\omega_{a,\sigma_n}t}\Big\} = \Re\Big\{\vec{\hat{\alpha}}_{\sigma_n}e^{j\omega_{a,\sigma_n}t}\Big\}\,, \tag{2.40}$$

where $\mathbf{\Theta}$ contains the traveling wave mode shape and the amplitude $\vec{\hat{\alpha}}_{\sigma_n}$ acts like a scaling factor and is non-complex. The aerodynamic force in terms of the local pressure consisting of a static and an

unsteady component as well as the variation of the blade normal $\vec{n}$ take also a harmonic form

$$p(t) = p + \hat{p}e^{j\omega_{a,\sigma_n}t} \tag{2.41}$$

$$\vec{n}(t) = n + \hat{n}_{\sigma_n}e^{j\omega_{a,\sigma_n}t} \tag{2.42}$$

while the scalar quantity pressure $\hat{p}$ is complex since it reaches its maximum phase shifted with respect to the blade motion. In the case of complex mode shapes, as they occur for bladed disks, the static pressure p does not have a significant influence on the AIC (usually less than 10%) but it is taken into account here for the sake of completeness [12]. Integrating the pressure over the oscillating blade surface which oscillates in the mode shape $\vec{\Theta}$

$$\begin{aligned}\vec{F}_{i,c}(t) &= -\int_A \left(p + \hat{p}e^{j\omega_{a,\sigma_n}t}\right)\left(\vec{n} + \vec{\hat{n}}_{\sigma_n}e^{j\omega_{a,\sigma_n}t}\right) dA \\ &= -\int_A \left(p\vec{\hat{n}}_{\sigma_n}e^{j\omega_{a,\sigma_n}t} + \hat{p}\vec{n}e^{j\omega_{a,\sigma_n}t} + p\vec{n} + \hat{\vec{p}}\vec{\hat{n}}e^{2j\omega_{a,\sigma_n}t}\right) dA\,.\end{aligned} \tag{2.43}$$

If only the unsteady forces are considered and the higher harmonics are dropped, Eq. (2.43) becomes

$$\vec{F}_{i,c}(t) = -\int_A \left(p\vec{\hat{n}}_{\sigma_n}e^{j\omega_{a,\sigma_n}t} + \hat{p}\vec{n}e^{j\omega_{a,\sigma_n}t}\right) dA \;= \vec{\hat{F}}_{i,c}e^{j\omega_{a,\sigma_n}t}. \tag{2.44}$$

and inserting Eqn. (2.40) and (2.44) into the aerodynamic work, Eq, (2.39), gives

$$W_{aero,\sigma_n} = \int_0^T \Re\left\{\vec{\hat{\alpha}}_{\sigma_n} j\omega_{a,\sigma_n}e^{j\omega_{a,\sigma_n}t}\right\} \cdot \Re\left\{\vec{\hat{F}}e^{j\omega_{a,\sigma_n}t}\right\} dt \tag{2.45}$$

Resolving the real part operators and further simplifying results in

$$W_{aero,\sigma_n} = \frac{1}{2}j\pi\left(\vec{\hat{x}} \cdot \overline{\vec{\hat{F}}}_{i,c} - \overline{\vec{\hat{x}}} \cdot \vec{\hat{F}}_{i,c}\right) = j\pi|\vec{\hat{\alpha}}_{\sigma_n}|^2 \int_A \vec{\Theta}^H \left(p\vec{\hat{n}}_{\sigma_n}e^{j\omega_{a,\sigma_n}t} + \hat{p}\vec{n}e^{j\omega_{a,\sigma_n}t}\right) dA\,. \tag{2.46}$$

Finally, the diagonal terms of the AIC matrix of Eq. (2.32) can be computed according to

$$C_{\sigma_n} = \frac{-W_{aero,\sigma_n}}{j\pi A_0\,(p_{01} - p_0)|\vec{\hat{\alpha}}_{\sigma_n}|^2} \tag{2.47}$$

where $\vec{\hat{\alpha}}_{\sigma_n}$ is the scaling factor of the eigenmode in the CFD calculation which is usually the same for all traveling wave modes.

A more thorough derivation of the aerodynamic influence coefficients is presented in [12]. As can be deduced from Eq. (2.47), only the imaginary part of the perturbation force and moments enter the work. If the aerodynamic response is lagging the excitation, the imaginary part has a destabilizing contribution [13].

3 State-of-the-Art

This chapter discusses some general aspects of mistuning with a more specific focus on shrouded bladed disks. Additionally, a review of currently available reduced order models is given and their applicability compared by predefined adequate criteria.

3.1 Mistuning

An ideal tuned bladed disk is a periodic structure consisting of identical blades and disk sectors which is generally modeled using cyclic symmetry. Although a bladed disk is typically designed in a tuned manner, there are always random deviations among the blades caused by manufacturing tolerances, operational wear or foreign object damage. These deviations among blades destroy the cyclic symmetry of the system and are referred to as mistuning. It is commonly known that mistuning usually has a negative effect on forced response and a positive one on flutter. In a structurally coupled analysis (no aerodynamic coupling), the presence of mistuning gives rise to some effects which are not common in tuned bladed disks. These are frequency splitting, mode localization and amplitude magnification which are individually addressed below.

In a tuned system without aerodynamic coupling, double nodal diameter correspond to a forward and a backward traveling wave and appear with the same frequency. These double nodal diameters are separated into two modes with different frequencies in case of mistuning. The separated frequencies stay close but the respective modes are more complex and cannot combine into a single sinusoidal wave [14]. It has a direct effect on forced response and is visible by an increase of amplitude peaks in the frequency range around the resonance frequency.

The distortion of mode shapes appeared in the literature through studies performed by Anderson [15] in the field of solid-state physics and applied by Ewins to bladed disks [16]. The localization of mode shapes was further assessed and the term has been established later by Hodges [17]. Hodges stated that mode localization is more pronounced with increasing strength of disorder (mistuning) or decreasing strength of mechanical coupling. In other words, the extent of mode localization depends only on the disorder-to-coupling ratio. When a structure is subjected to vibration energy, this energy cannot propagate arbitrarily to large distances but will substantially tend to localize around the excitation source. The steady-state response to this excitation decays asymptotically exponentially. However, it should not be compared to a damped response since the decay does not occur due to dissipation but rather due to confinement. The confinement of energy can be explained from two perspectives.

From a wave perspective, the confinement is caused by reflections of waves by constraints, e.g. at the edge of a bladed-disk sector. From a modal perspective, the localized modes in the immediate vicinity of the source will be excited greater with increasing mode localization than modes that are further away from the source. To give an example, a rotor which is excited by the wakes of an upstream vane row is considered. A tuned rotor would be excited by multiple of the vane row blade number and consequently, only nodal diameter which equals to these multiples would be found in the response. However, for a mistuned rotor with a high disorder-to-coupling ratio, the periodic excitation activates several nodal diameters which add up to the response with different contribution so that some are more pronounced than others. Since the disorder is high, the vibrational energy localizes around the blades for which the contribution of all the activated nodal diameters is the highest.

As a consequence, the vibration energy is localized around a limited set of consecutive blades instead of being distributed about the whole assembly, as it can be seen in Fig. 3.1. The number

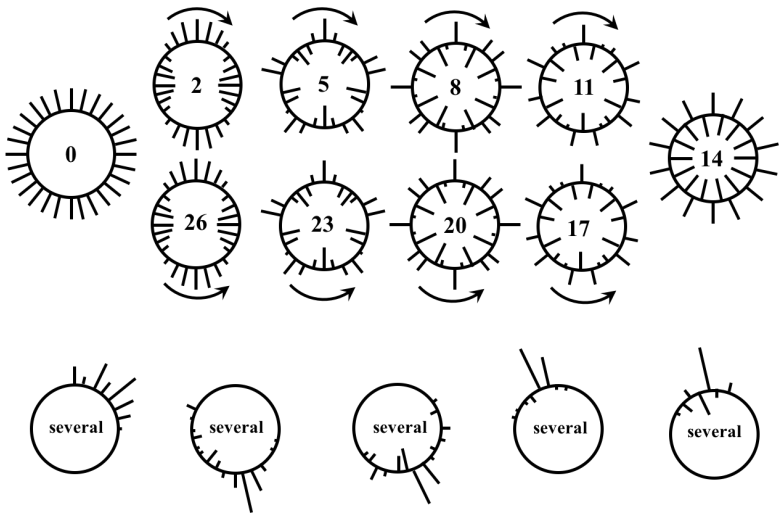

Figure 3.1: Tuned (on top) and Mistuned Modes (at the bottom) of a 28-Bladed Assembly (adapted from [18, 19])

inside the circle in the upper part of Fig. 3.1 indicates the circumferential harmonic of the disk (nodal diameter). So each modal response can be related to a distinct harmonic index for one mode family of the blade. The arrows symbolize the direction of the traveling wave. As indicated before, two traveling waves with different directions but similar modal characteristics, eigenfrequency and eigenvector, exist. In contrast, the response of a mistuned assembly to an engine order excitation has multiple harmonic contents, which may be identified through a Fourier analysis.

The amplification of the vibration amplitude due to mistuning was first estimated by Whitehead for a worst case scenario by relating the amplification factor A to the number of blades N [7].

$$A_{max} = \frac{1 + \sqrt{N}}{2} \tag{3.1}$$

The amplification factor is defined as the ratio of the maximum amplitude of the mistuned response to the tuned one. Further studies by Han et al. [20] established a relation of the maximum amplification

factor to the amount of damping in the bladed disk and concluded that the upper bound of the amplification factor stated by Whitehead might be over-conservative since it does not include damping. The maximum amplification factor increases with decreasing damping and is therefore crucial for the design. However, although mode localization increases monotonically with mistuning-to-coupling ratio, that does not apply to the amplification ratio as can be seen in Fig. 3.2. The amplification factor

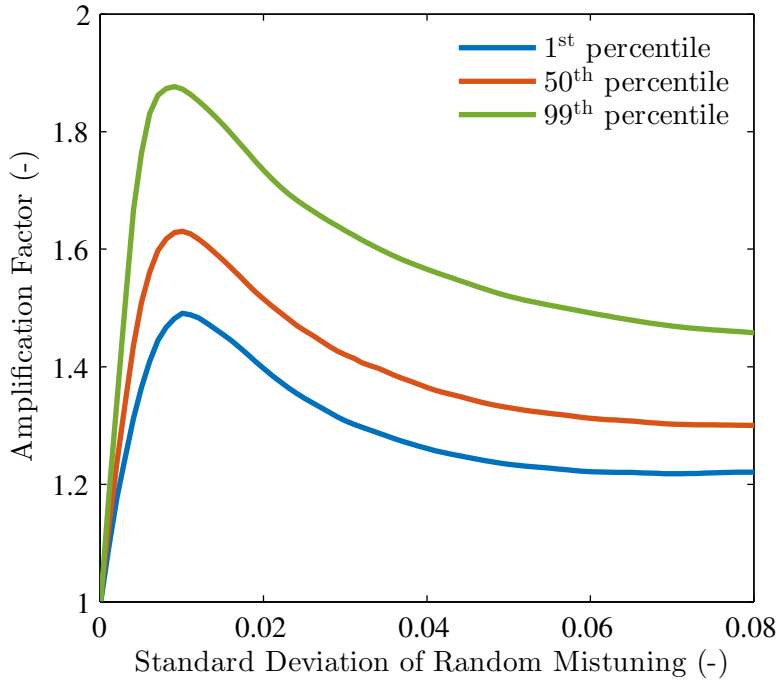

Figure 3.2: Aerodynamic Damping as a Function of the Mistuning Strength [21]

exhibits a peak value with respect to mistuning or coupling strength [16, 22, 23].

The influence of mistuning on the aerodynamic damping, i.e. flutter, has been examined in several studies. Mistuning increases the aerodynamic damping of the least unstable nodal diameters but as a consequence decreases the damping of the stable nodal diameters [6]. Consequently, the overall stability curve (aerodynamic damping versus nodal diameter) converges to a mean value of the tuned aerodynamic damping of all nodal diameters when the mistuning amplitude increases. Fig. 3.3 represents the converging behavior where the aerodynamic damping of a pair of stable and unstable modes tends to merge. Such converging behavior has been used to stabilize unstable systems by introducing intentional mistuning, e.g. alternate mistuning (every second blade is mistuned), as has been demonstrated by Crawley and Hall [24].

All the above phenomena are mainly caused by changes in the geometry or material of the bladed disk and are referred to as frequency or structural mistuning. Aside from that, there is another type of mistuning which is attributed to perturbations in the fluid passage and is commonly known as mis-staggering or aerodynamic asymmetry. While frequency mistuning enhances the stability of a system, aerodynamic mistuning can have a destabilizing effect and has to be addressed individually for different configurations [25, 26]. Nevertheless, the differences between a tuned and an aerody-

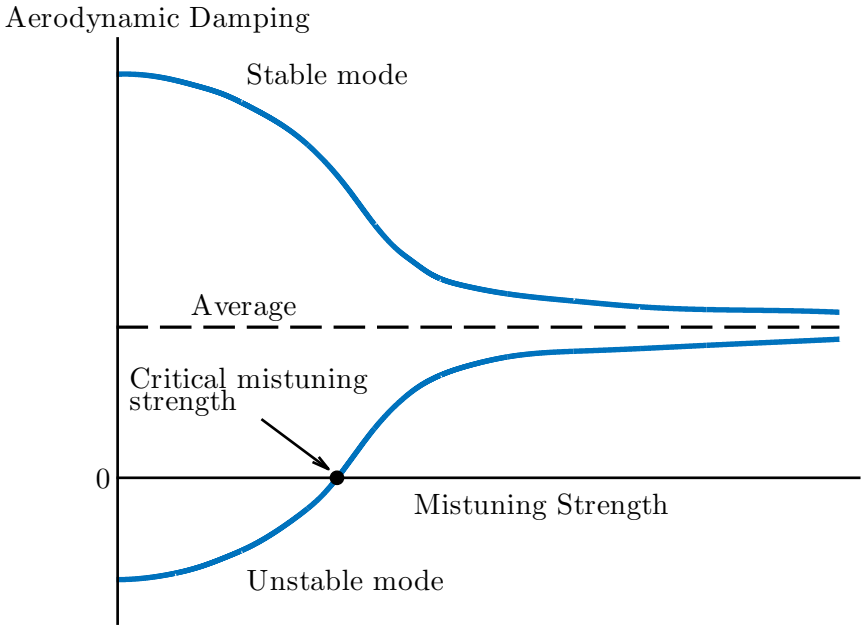

Figure 3.3: Aerodynamic Damping Change for a Pair of Modes due to Increase in Mistuning Amplitude [6]

namically mis-staggered configuration is rather small compared to frequency mistuning. Regarding forced response, when both frequency mistuning and mis-staggering are considered, the amplification factor is predominantly driven by the amount of frequency mistuning [27]. In addition, aerodynamic asymmetries do not cause a frequency split and no significant mode localization can be observed.

3.2 Reduced Order Modeling

For tuned bladed disks, it is possible to obtain the modal characteristics by defining a sector as one blade plus the corresponding segment of the disk. Using a finite element code, the structure can be analyzed by applying the appropriate phase conditions at the interfaces with adjacent sectors. Therefore, the structural characteristics of the entire cyclic structure can be predicted by only one sector model [28]. However, when the geometry, mass or stiffness of a bladed disk is perturbed, a single sector model is not able to correctly predict the vibration response of the system. Hence, a FE model of the whole assembly is required resulting in a high number of degree of freedoms (DOFs) and consequently high computational costs. In order to obtain the characteristics of a bladed disk subjected to random mistuning, e.g. caused by manufacturing tolerances, statistical tools such as Monte Carlo analyses are applied for which computations are repeated with varying mistuning strength. In order to reduce the number of DOFs and therefore the required computational resources, reduced order models become essential. Two main classes of ROMs have evolved over the last decades, namely methods based on component modes and system modes respectively. This two groups of ROMs with their main characteristics and submodels as well as other models characterized in neither of the two branches will be discussed in the following sections. All this methods provide a technique for assessing structural

mistuning. To account for aerodynamics, some methods were extended to model aeroelastic systems. Furthermore, a comparison of the models and limitations will be made, which is rather rare in the literature.

3.2.1 Component-Mode-Based Methods

The first generation of FE based reduced order models used an approach known as Component Mode Synthesis (CMS) or similar component-mode-based techniques. The main idea here is to divide the structure into substructures and to independently compute the individual normal modes [29–31]. The difference between several existing CMS models lies in the the modal basis of the ROM and especially in the way how the interaction or boundary conditions between the substructures are modeled. For a bladed disk, the interactions are usually referred to as a fixed-interface, a free interface or hybrid methods. One of the general requirements for the modal basis is that the modes have to be linearly independent. Apart from that, the use of the complete set of modes in the ROM from the parent FE model has to result in the exact solution relative to the parent FE model, i.e. it should span the complete deformation space [32]. The differences among the component-mode-based methods are the substructuring techniques and the mistuning implementations.

1. The receptance technique (RT) uses the observation that the dynamic response of every substructure can be identified by its interaction with the environment at its boundaries. When the interactions occur at limited areas, it becomes convenient to express the DOFs of the substructures by the motion of the DOFs at the boundaries. Menq et al. [33] used this behavior to model a mistuned shrouded bladed disk. However, the number of DOFs at the disk-blade interface is still quite large since the blades usually vibrate close to the clamped-free condition which requires a great number of modes to achieve good results. Yang and Griffin simplified the model by assuming the interface between blade and disk to follow a rigid body based motion [34]. On the one hand, this approach greatly enhances the computational efficiency in terms of time and cost and provides a systematic way of transferring parameters from FE models to the ROM. On the other hand, the effects of blade-disk coupling are completely ignored, due to the coarse way of how the blade-disk interface was modeled which can have a great influence on the outcome when mistuning sensitive studies are performed [35].

2. The Craig-Bampton (CB) substructuring technique enables to capture the motion at the interface better because there is a one-to-one correspondence between Craig-Bampton constrain modes and a node in the parent FE model. The CB method becomes of interest for bladed disks since the blade modes are calculated with a fixed interface which gives results that are in good agreement with bench test measurements of blade-alone natural frequencies. Consequently, the one-to-one modeling leads to large ROMs, in particular for a fine mesh and/or a large number of blades. With the aim to reduce the number of DOFs, the Craig-Bampton method was reformulated with the focus on mistuned bladed disks by several authors [36, 37]. In general, the modal basis for ROMs based on the CB approach consists of two set of modes: The first set is a truncated

set of normal dynamic modes of vibrations with the DOF at the component interface held fixed. Secondly, each interface DOF is subjected to a unit deflection while keeping all the other interface DOFs at rest so that all individual static constraint modes can be calculated.

Bladh et. al. [38, 39] tailored the CB method for a bladed disk with a cyclic disk component resulting in a very compact and robust model. Mistuning is included by modifying the cantilevered blade properties in the CMS coordinates and transforming them to the ROM coordinates by the eigenvectors of the CMS matrices.

Another way of reducing the size of the model using the CB technique is to treat each sector as a separated component. As an example, Tran [37] used this technique with component interface reduction to keep the number of DOFs low. Moyround et al. [36] did not employ an interface reduction but they validated the structural behavior of a shrouded bladed disk using among others a ROM which is based on the CB/CMS technique with separately treated sectors in a multisubstructuring approach. The latter method is able to consider mistuned mode shapes (i.e. non-nominal modes) and will be referred to as the Craig-Bampton Substructure Reduction (CBSR) technique.

3. Bladh et al. [38, 39] suggested a further modal reduction of the previously mentioned CBSR method by condensing out some interface modes. The resulting model is known as the Secondary Modal Analysis Reduction Technique (SMART). SMART can be applied to any intermediate model but the authors have chosen the CBSR method since the blade modal properties are directly accessible. This approach was further extended to multi-stage systems [40].

4. In SMART the mass and stiffness matrices are reduced in full-scale which means that the reduction technique is applied on the normal dynamic modes as well as on the static constraint modes. In contrary, Castanier and Pierre [41] proposed a partial secondary modal analysis where only the constraint modes at the interface are reduced. The new constraint modes are referred to as the Characteristic Constraint Modes (CCM). Similar to SMART, the CCM method was expanded for multi-stage rotors [40].

5. Another ROM was presented by Castanier et al. [42] and is sometimes referred to as the REDUCE model. Apart from cantilevered clamped blade modes, the modal basis contains additional blade modes which were induced by disk deformation. The latter ones are obtained by performing finite element modal analysis of the disk with intertialess blades (mass density of all blades set to zero). Due to lack of mass, the blades follow the motion of the disk and therefore compatibility between these two substructures is ensured without the need of constraint modes. This method was extended for shrouded bladed disks by Bladh et al. [43].

6. A Non-Nominal Mode Approach (NNMA) was established by Brown [44] where the modal basis consists of a set of geometrically perturbed mode shapes. In this context, non-nominal mode shapes means that no cyclic symmetry formulation is involved. This is different to many of the models above since their modal basis is built from tuned, cyclic symmetric modes. Non-

nominal Craig-Bampton matrices are generated using non-nominal substructure reduction from geometrically-perturbed FEM calculations.

7. A last approach which is worth to mention and was developed quite recently by Schreyer et al. [45] is a combination of the CMS method which is the basis for the ROM and a harmonic balance method (CMS-HB) to model non-linear contact at the shrouds. Assuming the solution is harmonic, the harmonic balance method approximates the solution of a differential equation by a truncated Fourier series so that any type of contact, i.e. free and fixed shrouds, linear sliding or non-linear friction contact at the shroud interface can be considered.

3.2.2 System-Mode-Based Methods

Similar to component-mode-based methods, system-mode-based methods use tuned or nominal modes to reduce the finite element matrices. The main distinction between these two methods is that system-mode-based methods do not require substructures to introduce mistuning. Instead, a sector consisting of a disk and a blade is modeled as one unit. In general, the system-mode-based method can be referred to as classical modal analysis with mistuning projection. The majority of the methods included in this class are based on the ROM developed by Yang and Griffin known as Subset of Nominal Modes (SNM).

1. For a low level of structural system distortion, Yang and Griffin [46] observed that the basis of selected tuned system modes is capable of representing the corresponding vibration characteristics of mistuned systems. Therefore, a classical modal analysis can be applied in the traveling wave domain for a given frequency range where the vibration energy is primarily stored in the blades (blade-dominated system modes). Using the advantage that modes of bladed disks are clustered together with similar frequencies, which is especially true for the first mode families, a linear weighted combination of a set of nominal mode shapes represents a mistuned mode. For that reason, the resulting mistuned mode contains several harmonics of the nominal Fourier basis. Since the mistuned mode shapes are defined by a limited selected set of tuned modes, the mistuned mode is approximated. The approximation error decreases with increasing number of included nominal modes and is inversely proportional to the frequency difference between the mode family under study and the next nearest mode family. The SNM method is able to account for mistuning with a system size equaling the number of blades which is the minimum size for mistuned ROM. Mistuning is included by assuming a form of mistuned blade structural matrices and transformed to system model coordinates (traveling wave space) by an appropriate coordinate transformation.

2. Feiner and Griffin [47] reduced the SNM even further to form a highly reduced order model and named it as Fundamental Mistuning Model (FMM) due to its simplicity. The reduction is done by limiting the nominal modes to a single family of blade modes, e.g. first bending or torsion mode. Similar to SNM, the FMM works well for the case of a isolated family of blade-dominated modes in which the strain energy is located primarily in the blades. The intention to simplify the SNM method even further is the mathematically complexity of SNM which makes it difficult to provide physical insights into the mistuning problem. However, the accuracy is reduced near

veering regions of disk- and blade-dominated modes and in regions with higher modal density. At the beginning, FMM was only applicable for rigid or less flexible disks since the deviation mistuning was modeled as a deviation in the blade-alone frequency. Nevertheless, the model was improved later to allow for more strain energy in the disk [48, 49]. Consequently, mistuning is distributed in the whole blade-disk sector in the improved version of the model.

3. A further adaption of the FMM using an asymptotic approach was done by Martel et al. [6] and was consequently labeled as Asymptotic Mistuning Model (AMM). The AMM is further reduced compared to FMM since only so called active modes of a given family of modes are used to build the modal basis of the ROM. The active modes are those tuned modes which are "relevant" from the point of view of mistuning. In the reduced aeroelastic model, it is assumed that both aerodynamics and structural dynamics of the assembly are linearized. The tuned system was perturbed asymptotically and only the first order terms were computed representing aerodynamic perturbation and blade mistuning. The fully consistent asymptotic expansion allows to describe the effect of small mistuning on modes belonging to the same family but exhibiting non-small variation in frequency as was shown by Martel et al. for interlocked and welded-in-pair low-pressure turbine blades (LPT). Therefore, AMM can be used for stronger coupled blades where the frequency greatly varies with the structural harmonics. In other words, AMM provides great accuracy in disk- and blade-dominated modes of the same mode family. AMM is unique because it is capable to unveil some physical insights into the mistuning problem. It describes in detail how the aerodynamic damping corresponding to a tuned specific nodal diameter pattern could be affected by adding intentional mistuning which would couple the responding waves.

4. A mixed method between component-mode-based and system-mode-based methods was developed by Lim et al. [50]. Both nominal system modes and blade component modes are used as the modal basis and the approach is named as the Component Mode Mistuning (CMM) method. The basis of the ROM is created by a linear combination of tuned system modes as it is done in the SNM technique. Mistuning is added to the system by modeling and perturbing the blade-alone motion through a virtual set of cantilever blade modes. Optionally, Craig and Bampton constraint modes for clamped DOFs are utilized in the cantilevered blade model. By identifying the blade motion in the tuned system modes, modal participation factors are established. This participation factors project the individual blade mistuning onto the reduced final modal basis. The CMM mistuning projection method by Bladh et al. [43] is an extension of the REDUCE method version which was tailored for shrouded blades. A great advantage of the CMM method is that it can handle various types of blade mistuning in a systematic way, including non-uniform variations of individual blades that lead to different frequency mistuning patterns for different types of blade-alone modes, e.g. as it occurs in higher frequency regions.

5. The majority of the reduced order models include mistuning by varying the stiffness matrix (Young's modulus). This facilitates the analysis since it allows to transform the equations of motion into the modal domain. In reality, a variation in the blade geometry implies a change

in the mass as well which is disregarded by common ROMs. The perturbation in the mass and stiffness matrix is referred to as geometric mistuning and Sinha [51] explored this type of mistuning and established a ROM known as Multiple Modal Domain Analysis (MMDA). According to Sinha, the SNM approach can predict the vibration characteristics of bladed disk with geometry mistuning but to do so, an arbitrarily large number of tuned modes is required. Thus, the main aim of ROMs to reduce the size and the computational effort is missed and the model cannot be seen to be a reducing approach. The modal basis of MMDA is composed of nominal system tuned modes and tuned modes of rotors having perturbed geometry based on a spatial statistics model. Although the MMDA utilizes an approximated basis, because the actual geometry is neglected, large computational costs associated with the transformation of physical sector DOFs to the ROM basis are inevitable. In addition, multiple solutions from sector models are needed as input. In contrast, CMS would alleviate this issue by portioning the substructures in such a way that the disk DOFs are calculated only once for each retained geometry model. Nevertheless, Sinha's work is still noteworthy because of its novelty and the possibility to account for perturbations in the mass matrix.

3.2.3 Other Reduced Order Models

There is a large variety of ROMs which cannot be assigned to one of the two main classes. This section lists only a small fraction of the available ROMs with a short description.

1. The first exclusive group which is worth to mention is the lumped parameter models. Already for this subclass, there are many models which differentiate between each other depending on the complexity and accuracy. One of the first to establish a reduced order model was Wagner in 1967 [52]. In Wagner's model the individual blades are connected through springs and dashpots to a flexible disk without inertia (no mass). The disk is flexible in a sense that it is connected by many springs to a ground. Since the disk is massless, the obtained frequencies are blade-alone frequencies. Another possible type of coupling was realized by Sinha and Chen [53]through an inter-blade spring and the blades are attached to the ground again by linear spring and dashpots. Happawama et al. [54] built a model to allow a mistuning analysis for strongly-coupled bladed disks by connecting the blades among each other and to the disk by torsion springs respectively.

   All of the above models consider only one degree of freedom per mass (blade). More enhanced lumped parameter models were developed by Griffin and Hoosac [55, 56] consisting of three degrees of freedom per sector. The coupling was realized by beam-like structures and in an extended version by springs, dashpots and aerodynamic forces. Therefore, their method can be applied for mistuned force response analyses of an unshrouded bladed disk.

   A last method worth to mention here is the model provided by Basu and Griffin [57] in which a finite-element approach is applied. The blades are connected to the disk through linear springs whereas the disk is modeled by an axisymmetric plate discretized through shell elements. Likewise the previous method, the finite element based model allows to include aerodynamic forces and was used to analyze the influence of the fluid density on the mistuning.

2. Another approach is the adaptive perturbation technique (APT) by Lin and Mignolet [58] which was used to study the forced response of a bladed disk. The basis of the mistuning approach is to establish an impedance matrix based on the tuned configuration. The impedance matrix is filtered to create partitions of blocks associated to the natural frequencies that are either close or far away from the excitation frequency. The steady-state response is calculated by applying the filter impedance matrix where a perturbation expansion technique is employed on the frequencies far away from the excitation frequencies to account for mistuning. The approach is adaptive in the way that the number of frequencies that were included can be varied.

3. Petrov et al. [59, 60] created a so called Exact Reduced Order Model (EROM) which computes the response for a forced analysis using the tuned forced matrix as well as a modification matrix, which is built from the frequency response function of the tuned system and a mistuning matrix. Mistuning is employed in the physical space by lumped masses, dampers and springs which are attached to active coordinates. The equations of motion are only solved for the active coordinates which are obtained by reducing the tuned system in the physical system, leaving only the degrees of freedom where mistuning is applied and those where the forced level is of interest. EROM is exact in a sense that no approximation at all is applied to the model.

4. A further unique approach is the usage of Artificial Neural Networks (ANN) for mistuned forced response analyses [61, 62]. In the first phase, the ANN adapts to the structure and tries to learn the mapping relationship from the blade property (blade frequency) to maximal vibrating displacement and the corresponding frequency. Once the relationship is established, the network should provide an output for any applied level of mistuning.

3.3 Analyses Findings for Mistuned Shrouded Bladed Disks Using Reduced Order Models

This section outlines the results obtained for shrouded blades using reduced order models. The review emphasizes on main findings, limitations of ROMs dealing with shrouded blades and is ordered in a chronological order when the findings were published.

Bladh et al. [43] used the REDUCE method with a few pertinent adaptions for shrouded blades modeling the tuned-blade shroud ring as a single, cyclic component. Therefore, his approach is limited to full-stick or full-slip shroud interfaces. The presented analysis by Bladh et al. solely focuses on a structural dynamic analysis including a free and forced response analysis but without any aerodynamic coupling. The level of mistuning is sampled from a random, uniform distribution with a standard deviation of 5% and the difference in frequency is attributed only to the blade, i.e. a blade with clamped roots and free shrouds. However, to build the component mode synthesis matrices, a complete sector with cyclic constraints at disk-to-disk and shroud-to-shroud interfaces is analyzed. Since mistuning was introduced by scaling the Young's modulus, no individual mode mistuning was implemented.

To account for random mistuning, full rotor FEM calculation were performed. The total number of DOF for the full rotor is 56,376 which could be minimized to 240 DOF after model reduction

representing 0.4% of the initial size. The results for free and forced response were in good agreement between the full rotor FEM calculations and the REDUCE method. Bladh was one of the first to validate the capability of a ROM to correctly predict the response of shrouded blades. Nevertheless, being a pure numerical analysis, no conclusion about the behavior of mistuned shrouded blades has been made. In addition, the neglect of any aerodynamic coupling makes it difficult to extend his results straightforward for flutter analyses.

Moyroud et al. [36] provided a comparison between the SNM and CBSR methods because they have the advantage that the analyses can be performed for unshrouded as well as shrouded blades without any particular extensions. The modal basis of the SNM approach is built upon tuned modes from cyclic symmetry FEM calculation. In contrary, tuned non-nominal modes, i.e. without cyclic symmetry formulations (full rotor calculations), are used as the modal basis for the CBSR approach. Three different configurations are utilized in their free response analysis: An axisymmetric annular plate (AXI) with strong intersector elastic coupling strength (simplified model of a continuously shrouded bladed disk), a cyclic symmetric annular plate (CYC) with 20 cyclic symmetric sectors with a weak intersector elastic coupling strength and a typical modern design industrial bladed disk fan with 30 blades. The DOF resulting reduction through both ROMs is summarized in Tab 3.1.

Table 3.1: Size Reduction of the Structural System for the SNM and CBSR Method for Three Different Rotor Configurations

	FEM model	**SNM**		**CBSR**	
	size	size	% of FEM	size	% of FEM
AXI	10080	80	0.8%	2080	20.6%
CYC	9600	80	0.8%	880	9.2%
Real fan rotor	304,650	120	$< 0.1\%$	23640	7.8%

The FEM model size represents the "full rotor" model in each case. Two types of frequency mistuning were investigated: $\pm 10\%$ partial mistuning (only reference blade is mistuned) and $\pm 10\%$ alternate (harmonic) mistuning.

Both ROMs are capable to accurately predict the first tuned and mistuned modes of AXI and CYC configurations at rest (no rotational speed). Hence, the ability of the two ROMs is insensitive with respect to the elastic coupling strength. It was observed that a perturbed system with weak structural coupling (CYC) is more prone to mode localization than a mistuned system with stronger structural coupling (AXI).

Mode localization of the real fan rotor can be detected, provided enough tuned modes are included into the modal basis. There is a quite good match in the results between the FEM, the SNM and CBSR method regardless of takening into account centrifugal forces or not, i.e. rotating rotor and rotor at rest. The usage of the two ROMs results in a computational time reduction in the order of magnitude of 1 to 2. The findings of this investigation of the fan rotor revealed that the structural frequencies are much less sensitive to mistuning than the mode shapes. The mode shape sensitivity depends on the sign of the stiffness perturbation, i.e. increasing or decreasing the Young's modulus, and the

rotational speed. Moyround et al. concluded that the SNM approach is clearly more efficient in terms of DOF size reduction and consequently in terms of the required computational time. Nonetheless, the CBSR method is more flexible in its application range since a full-stick, full-slip as well as a stick-slip constraint can be incorporated at the shroud interface.

Lim et al. [50] reported the results of a free and forced response analysis (aerodynamic coupling neglected) for an unshrouded and a shrouded bladed disk of similar disk-blade geometry using their established reduced order method CMM. The geometry of the unshrouded blade is the same as for the shrouded case with the exception of a full-stick or full-slip shroud interface. Both proportional and non-proportional stiffness mistuning in a veering region are studied where a mistuning amplitude up to 7% is applied. The modal density for the shrouded configuration is lower and consequently, it is difficult to predict mistuned system normal modes. In other words, since the modes are not closely spaced, more tuned-system normal modes are required to capture mistuned system normal modes compared to the unshrouded case. Therefore, Lim et al. choose two regions where the modal density is higher to perform the forced response analysis.

Again, based on the variation of the modal density, Lim et al. reported that the provided results for the shrouded case are less accurate than for the configurations without shrouds. This shows the complexity in reducing the model size of a shrouded rotor and still obtaining sophisticated results. However, the accuracy is better for the shroud interface with a fixed connection when boundary-mode mistuning is included than with a free-shroud interface relative to the FEM results. Furthermore, when non-proportional mistuning is applied, only the free-shroud model can be used since the fixed-shroud rotor produces poor results.

Corral et al. [63] as well as Martel et al. [6] made a comparison of the stability of a cantilever, welded-in-pair and interlock bladed disk of a low pressure turbine while the former uses FMM and the latter the AMM method, respectively. At first glance, the welded-in-pair and the interlock configuration might look similar in terms of their modal characteristics but they are substantially different though. While the unstable modes of the interlock rotor are separated in terms of frequency from the rest of the modes, the unstable modes of the welded-in-pair rotor are clustered together and share nearly the same frequency. They noted that the flutter boundaries are very sensitive to blade mode shapes and the reduced frequency plays a secondary role.

In the paper of Corral et al., the boundary conditions of the shrouded blades were modeled using phase-shifted boundary conditions, i.e. cyclic symmetry, in the structural analysis and hence, full-stick interlocks were considered. It was assumed that aerodynamic and structural models are linear and consequently, the damping of the mistuned configuration is always larger compared to the tuned configuration. The tuned reduced frequency for all three configurations is shown in Fig. 3.4. It can be observed from Fig. 3.4 that the modal density of the welded pair is high and comparable to the cantilever bladed disk whereas the interlock design has a low modal density for almost all nodal diameter. In addition, the interlock configuration, see Fig. 3.4c, experiences a transition between edge-wise modes at low ND and torsion modes at high ND.

Welding of the blades to pairs increases the aerodynamic damping since the mode shapes are modified. The increase in damping is still inferior compared to the interlock design because the

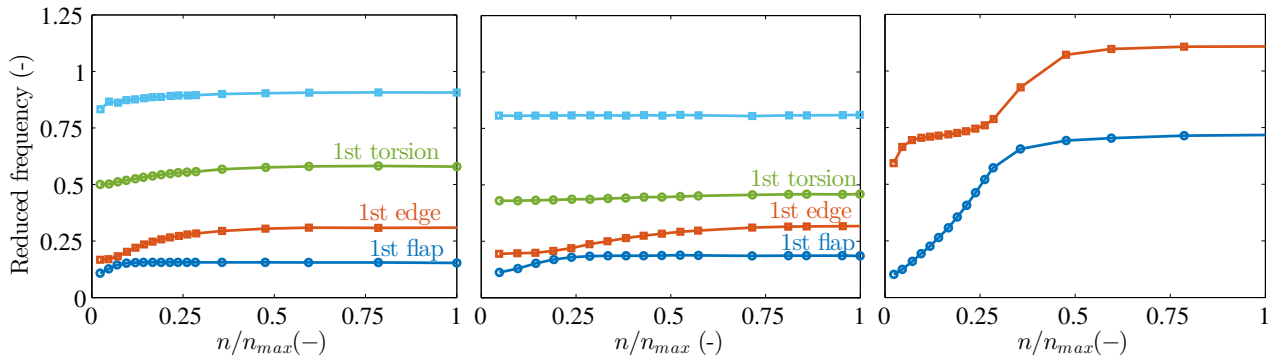

(a) Cantilevered Blades **(b)** Welded in-Pairs Blades **(c)** Shrouded Blades

Figure 3.4: Change of Reduced Frequency with Nodal Diameter for Different Blade Configurations of a Bladed Disk [63]

interlock dramatically changes the overall behavior of the assembly and considerably raises the reduced frequency so that the rotor in general is less prone to flutter. The level of mistuning is sampled from a normal distribution with a standard deviation of 1%.

The results obtained by the FMM suggest that the consequences of mistuning on shrouded blades are negligible and the effect on the welded configuration is essential to increase the aerodynamic damping. This can be explained as follows: The most unstable modes of the interlock configuration were observed for an inter-blade phase angle between 0° and 45° which can also be observed from the reduced frequency plots in Fig. 3.4c. These modes are separated from the rest and consequently, as stated by Corral et al., mistuning is not able to effectively combine unstable and stable modes. However, the welded packs of blades are unstable for a wide range of inter-blade phase angles between 0° and 160° where many modes have nearly the same frequency and may be sufficiently combined by the effect of mistuning to increase the minimum damping. Nevertheless, the interlock design remains still superior to the welded-pair design due to already higher aerodynamic damping of the tuned system. Martel et al. underlines the findings of Corral et al. by using the AMM approach and gets a similar trend of the results.

Finally, Schreyer et al. conducted an analysis to investigate the difference between the effects of modeling the contact as a fixed interface, linear sliding contact and non-linear friction contact of a mistuned shrouded bladed disk on forced response. Their full FE model has 59,508 DOF whereas the ROM reduced by the CMS approach has just 300 DOF which corresponds to a reduction of more than 95.5%.

The normal forces are increased from $0\,N$ to a certain amount in order to obtain a transition from a free sliding interface, over a non-linear friction contact to a fixed interface for the tuned case. First, when the normal force is increased, the amplitudes decrease since the relative motion of the shrouds is present and non-linear friction occurs. After the normal force has passed a certain limit value, the amplitudes start to increase again due to the more appearing dominance of the stick condition so that less energy can be dissipated by friction.

The frequency response function of the ROM for the mistuned rotor with a fixed shroud interface

agrees reasonably well with the FE code. As expected, the amplitude of some blades increases whereas the amplitudes of others decreases. When a stick-slip condition is employed, the peak amplitude decreases compared to the full-stick shroud but the amplitude is still higher than for the tuned case.

3.4 Comparison of Reduced Order Models

One of the aims of this thesis is to provide a detailed overview over known available reduced order models. By answering some general points, the overview should help to select a suitable ROM for the case under study. To be able to establish such an overview in form of a comparison table, several criteria are identified and are explained below.

1. Year: "Year" shows when the ROM was firstly published. For some ROMs two years are given because the ROM was primarily published in the first year but a significant adaption or expansion was implemented in the second year.

2. Mistuning projection domain: The mistuning projection domain indicates in which domain the mistuning is introduced. Two distinctions are possible, namely in the physical or cyclic domain.

3. Mistuned modes domain: This entry shows whether the ROM considers non-nominal modes in the presence of mistuning or solely nominal modes which are tuned cyclic symmetric modes. Mistuning destroys the cyclic symmetry of a system so that a quasi-cyclic symmetric approach or a full rotor calculation is necessary. A quasi-cyclic symmetric approach means that a certain mistuning pattern, for instance alternate mistuning, admittedly destroys the cyclic symmetry but it can be recovered by considering several bladed disks sector in the computational domain. However, some ROMs approximate the mistuned eigenvectors by non-nominal modes and ignore the effect of mistuning on the actual mode shape.

4. Type: The point type stands for the type of mistuning. There are two major types of mistuning which are proportional (prop) and geometric (geo) mistuning. For the former type, the blade mass or stiffness is globally scaled by a single factor whereas for the latter type the change in properties can be introduced locally. Therefore, with geometric mistuning the impact of foreign object damage on the flutter stability can be analyzed. Both proportional and geometric mistuning can be further distinguished in physical (phy) and artificial (art) mistuning. While mechanical properties are modified directly for physical mistuning, artificial mistuning takes into account changes in the modal characteristics such as the vibrational frequency.

5. Amount: The "amount" specifies the level of mistuning, i.e. small or large, until which the ROM gives accurate results.

6. Property: The entry "property" shows which of the mechanical properties is mistuned. The possible mistuned properties are the mass $\mathbf{M}$, stiffness $\mathbf{K}$ or even the damping $\mathbf{C}$.

7. Geometry: As the name says "geometry" shows the geometry which is mistuned in the ROM, i.e. only the blade or the whole bladed disk sector including the blade as well as the disk.

8. Aero: The point “aero“ gives an indication about whether it is possible to calculate the aerodynamic damping using the ROM. This is determined by answering the question whether aerodynamic influence coefficients are included or if an extension to incorporate AICs is possible, so that a flutter calculation is feasible.

9. Shroud: The criteria “shroud“ suggests whether the ROM was proven to work for strongly coupled blades with an interlock. For that reason, the criterion is only positively answered when an existing publication exists which shows accurate results for shrouded blades. However, the point is negative when an author states that the the ROM works for shrouded but has never proven it.

10. Veering: The point “veering“ tells whether the ROM gives accurate results in veering zones.

11. Order: “Order“ gives an estimate about the retained number of degrees of freedom of the parent model and hence, the computational time. It has to be kept in mind that even when the order is low, the required input or the complexity of the ROM might still be high.

12. Input: The entry “input“ lists the main input parameter needed for the specific model. It is suggested to see the order of the ROM in conjunction with the required input parameter in order to get a conclusion about the effort to setup and get good results using a ROM.

Tables 3.2 and 3.3 show the comparison of the different models with the evaluated criteria listed in chronological order. A dash indicates that there is no information available for this entry in the publication or the entry is irrelevant for the particular ROM.

It can be observed from Tab. 3.3 that only a portion of the ROMs allows to determinate the flutter stability. Some of the models require a high amount of input parameters and are quite complex. Selecting from the flutter suitable models, the Fundamental Mistuning Model (FMM) is chosen to be used in the present work. Although the FMM is not proven to give accurate results for shrouded blades, the model was utilized by Corral et al. to study mistuned interlocked bladed disks [63]. Martel et al. concluded later that the FMM is not able to manage a great variation of the frequency with the harmonic nor a high level of mistuning [6]. Nevertheless, the FMM is used due to its simplicity in order to make an attempt to explain at which point exactly the model would possibly fail. In addition, the aim is also to verify whether the FMM gives accurate results compared to full mistuned calculations, i.e. including structural effects and aerodynamic asymmetries, without a cyclic symmetry at the shroud interface. Once the FMM is implemented, it can also serve as a basis for an extension similar to the methedology of the AMM which allows greater structural coupling.

Table 3.2: Overview over Different ROMs with Selected Criteria

	Year	Mistuning projection domain	Mistuned modes domain	Type	Amount	Property	Geometry
RT	1986 & 1997	physical	nominal	prop: phy, art	small	$\mathbf{K}$	blade
APT	1997	physical	-	geo: phy, art[1]	small	$\mathbf{M}, \mathbf{K}$	blade
REDUCE	1997 & 1999	cyclic	nominal	prop: phy, art	small	$\mathbf{K}$	blade
ANN	2000	-	-	-	small[2]	$\mathbf{M}, \mathbf{K}$	-
SMART	2001	physical	nominal	prop: phy, art	small	$\mathbf{M}, \mathbf{K}$	blade
SNM	2001	cyclic	nominal	prop: art	small	$\mathbf{M}, \mathbf{K}$	blade & disk
CBSR	2001 & 2002	physical	nominal & non-nominal	prop: phy, art	large	$\mathbf{M}, \mathbf{K}$	blades
FMM	2002	cyclic	nominal	prop: art	small	$(\mathbf{M},)\,\mathbf{K}$[3]	blade & disk
EROM	2002	physical	nominal & non-nominal[4]	prop: phy, art	large	$(\mathbf{M},)\,\mathbf{K}\,(, \mathbf{C})$	blade
CMM	2003	physical	nominal	prop: phy, art[5]	small[6]	$(\mathbf{M},)$[7] $\mathbf{K}$	blade
MMDA	2007	physical	nominal & non-nominal[8]	geo: phy, art	large	$\mathbf{M}, \mathbf{K}$	blade
AMM	2008	cyclic	nominal	prop: art	small	$\mathbf{M}, \mathbf{K}$	blade & disk
NNMA	2008	physical	nominal & non-nominal	geo: phy, art	large	$\mathbf{M}, \mathbf{K}$	blade
CMS-HB	2014	physical	nominal	prop: art	small	$\mathbf{K}$	blade

[1] The ROM is quite simple though so that a real bladed disk is not properly modeled.
[2] Only a low level of mistuning is applied in the reference paper but a higher level of mistuning might be possible.
[3] There is one parameter that varies simultaneously the mass and stiffness.
[4] The ROM is an exact expression for forced response.
[5] Shrouded blades are only analyzed with artificial mistuning. Non-linear or geometrical mistuning is also possible for unshrouded configurations.
[6] The CMM model is derived for the shrouded case only for small mistuning. Large mistuning is possible for cantilevered configurations.
[7] A mistuning of the mass is possible for a generalized model which does not have to be computationally efficient and might be complex.
[8] Non-nominal modes are constructed from perturbed nominal modes.

Table 3.3: Overview over Different ROMs with Selected Criteria (Continued)

	Aero?	Shrouds?	Veering?	Order	Input
RT	no	yes	no	$\sim$ interface DOFs	single clamped blade modes, cyclic disk modes
APT	no	yes / no [9]	-	$\sim$ truncated Taylor series	equivalent mass, stiffness and damping matrices for lumped mass model, modal properties of tuned system (eigenfrequencies, eigenvectors)
REDUCE	no	yes	yes	$\sim$ retained DOFs in ROM	see footnote[10]
ANN	no	no	-	independent	-
SMART	no	no	yes	$\sim$ retained DOFs in ROM	CB substructure modes[11] and FE matrices of substructures
SNM	yes	yes	yes	$\sim$ retained DOFs in ROM	nominal system modes and frequencies, AIC
CBSR	no	yes	yes	$\sim$ interface DOFs	same as SMART
FMM	yes	no	no	$\sim$ independent, N	system normal frequencies, AIC
EROM	no	yes	yes	$\sim$ mistuned and "interesting" nodes	nominal system modes and frequencies, frequency matrix
CMM	yes	yes	yes	$\sim$ retained blade normal modes	modal participation factor, cyclic symmetric disk modes, cantilevered blade disk normal modes, static constraint modes, AIC
MMDA	no	no	yes	$\sim$ retained tuned principal modes and component modes	see footnote[12]
AMM	yes	yes	no	$\sim$ independent, $\leq N$	system normal modes, AIC, aerodynamic / mistuning correction matrix
NNMA	no	-	-	$\sim$ interface DOFs	see footnote[13]
CMS-HB	yes	yes	-	$\sim$ retained blade normal modes	same as CMM

[9] The input for the ROM is not from a FE model but from a lumped mass model which allows strong blade-to-blade coupling.

[10] The required input consists of blade mode shapes from modal analysis of a disk sector with a massless blade and corresponding modal stiffness, mode shapes of a cantilevered blade and corresponding modal stiffness and FE mass and stiffness matrices of a free blade.

[11] The CB substructre modes include blade and disk normal modes as well as blade and disk constraint modes.

[12] The required input consists of eigenmodes, mass and stiffness matrices of a tuned cyclic symmetric analysis, mode shapes of a tuned blade with specifically modified geometry and the FE mass and stiffness matrices of the whole tuned rotor.

[13] Several models are presented in the reference source and it is advised to look up the input in the given reference.

4 Theoretical Background for the Fundamental Mistuning Model

The Fundamental Mistuning Model, initially developed by Feiner and Griffin [48], is a structural reduced order model which was extended by Kielb et al. [64] for aerodynamic coupling allowing the determination of the aerodynamic stability as well as forced response calculations. Hence, the derivation of the model is based on both aforementioned works. Firstly, a purely structural method including mistuning effects is derived. In the second step, aerodynamic influence coefficients are introduced into the mistuned equation of motion. This allows to solve an eigenproblem for the aeroelastic eigenvalues which, among others, consist of the aerodynamic damping.

4.1 Structural Analysis

The fundamental mistuning model considers an isolated mode family of a bladed disk where a significant amount of the strain energy is located in the blades. If a considerable amount of the strain energy is in the disk, the structural frequencies vary with the harmonic and the modes are not isolated so that an interaction with other mode families might occur. This statement is also partially true for shrouded bladed disks: Although the strain energy does not explicitly have to be primarily in the disk, the frequencies cover a broad range since the coupling takes place over the shrouds. Nevertheless, despite of the great variation in the frequency, the mode family can still be isolated. This assumption has to be kept in mind for the discussion of the results of the coming mistuning analysis.

To set up the structural FMM (without aerodynamic coupling), theoretically, three sets of inputs are required which usually can be extracted from a cyclic symmetric structural analysis of the tuned system:

1. The modal stiffness matrix of the isolated mode family $\mathbf{\Omega}$, similar as in Eq. (2.15) which contains the tuned structural frequencies along the diagonal.

2. All tuned mode shapes are defined in the traveling wave domain. The mode shapes are complex and are arranged as follows
$$\mathbf{\Theta} = \left[\vec{\Theta}_0, \vec{\Theta}_{1F}, \vec{\Theta}_{2F}, ..., \vec{\Theta}_{1B}\right] \tag{4.1}$$
where $\vec{\Theta}_{nF}$ and $\vec{\Theta}_{nB}$ refer to the n^{th} forward and backward traveling mode respectively. It can be noted that the mode shapes are not required in practice since they are known to be periodically in

the case of a tuned system. Hence, they are assumed to be known for the proceeding derivation.

3. The mistuning pattern of the blade disks expressed as a fractional change $\Delta\omega_{mis}$ of the tuned frequencies of a sector,

$$\Delta\omega_{mis} = \frac{\omega_{mis} - \omega^0}{\omega^0} \tag{4.2}$$

with ω_{mis} and ω^0 being the mistuned and tuned structural frequency, respectively.

In the FMM, each blade is represented by a single degree of freedom resulting into N independent equations of motion. Another further implicit assumption is done in the reduced model which says that solely the stiffness matrix is perturbed. This is not explicitly mentioned in the paper by Feiner and Griffin, but implied when equations are rearranged and simplified which will be shown later.

The structural equation of motion for a mistuned bladed disk is given by

$$\Big[\mathbf{K} + \Delta\mathbf{K} - \omega^2(\mathbf{M} + \Delta\mathbf{M})\Big]\vec{\Theta}_{mis} = \vec{0} \tag{4.3}$$

where the mass and stiffness matrices are separated into a tuned and a mistuned part, i.e. $\Delta\mathbf{K}$ and $\Delta\mathbf{M}$, respectively. The tuned eigenvectors are altered by the mistuning and hence, the system responds with a mistuned mode shape $\vec{\Theta}_{mis}$ and a mistuned eigenfrequency ω. Since the family of modes is isolated, the mistuned eigenvector $\vec{\Theta}_{mis}$ can be approximated by the N tuned mode shapes of the isolated family by a weighted sum

$$\vec{\Theta}_{mis} = \mathbf{\Theta}\vec{\beta}_{mis}\,. \tag{4.4}$$

$\vec{\beta}_{mis}$ contains the weighting factors to what extent a tuned mode is represented in the mistuned mode. Obviously, the model completely misses the occurrence as well as the effects of crossing or veering regions.

Once again, the tuned eigenvectors of the matrix $\mathbf{\Theta}$ are mass normalized so that the following properties hold for the stiffness matrix

$$\mathbf{\Theta}^H\mathbf{K}\mathbf{\Theta} = m^*\mathbf{\Omega}^2 \tag{4.5}$$

as well as for the mass matrix

$$\mathbf{\Theta}^H\mathbf{M}\mathbf{\Theta} = m^*\mathbf{I}\,. \tag{4.6}$$

Inserting Eq. (4.4) into Eq. (4.3) and premultiplying the result by the Hermitian $\mathbf{\Theta}^H$ gives

$$\begin{aligned}\Big[\mathbf{\Omega}^2 + \mathbf{\Theta}^H\Delta\mathbf{K}\mathbf{\Theta} - \omega^2\mathbf{I} - \omega^2\mathbf{\Theta}^H\Delta\mathbf{M}\mathbf{\Theta}\Big]\vec{\beta}_{mis} &= \vec{0} \\ \Big[\mathbf{\Omega}^2 + \mathbf{\Theta}^H\Delta\mathbf{K}\mathbf{\Theta} - \omega^2\mathbf{\Theta}^H\Delta\mathbf{M}\mathbf{\Theta}\Big]\vec{\beta}_{mis} &= \omega^2_{mis}\vec{\beta}_{mis}\,.\end{aligned} \tag{4.7}$$

It can be deduced from Eq. (4.7) that the FMM establishes an eigenproblem with the mistuned frequencies ω_{mis} being the eigenvalues and the weighting factors $\vec{\beta}_{mis}$ the eigenvectors of the mistuned configuration. As mentioned before, it is not obvious at first glance that the eigenproblem implicitly and solely assumes a perturbation of the stiffness matrix. In general, the eigenvectors of a eigenproblem

fulfill the orthogonality character. As a consequence, in this case, recalling that the tuned eigenvectors are mass normalized and likewise i sthe weighting vector, the eigenvectors of the eigenproblem in Eq. (4.7) have to fulfill the following relation

$$\vec{\beta}_{mis}^{H}\vec{\beta}_{mis} = 1 \tag{4.8}$$

where a similarity can be seen to the tuned normalization, Eq. (4.6). Accordingly, the mass normalization of the mistuned mass matrix $\mathbf{M}_{mis}$ to any mistuned eigenmode $\vec{\beta}_{mis}$ equals unity,

$$\begin{aligned}\vec{\Theta}_{mis}^{H}\mathbf{M}_{mis}\vec{\Theta}_{mis} &= \vec{\beta}_{mis}^{H}\boldsymbol{\Theta}^{H}\Big(\mathbf{M}+\Delta\mathbf{M}\Big)\boldsymbol{\Theta}\vec{\beta}_{mis} \\ &= \vec{\beta}_{mis}^{H}\boldsymbol{\Theta}^{H}\mathbf{M}\boldsymbol{\Theta}\vec{\beta}_{mis} + \vec{\beta}_{mis}^{H}\boldsymbol{\Theta}^{H}\Delta\mathbf{M}\boldsymbol{\Theta}\vec{\beta}_{mis} \\ &= \underbrace{\vec{\beta}_{mis}^{H}\vec{\beta}_{mis}}_{=1} + \vec{\beta}_{mis}^{H}\boldsymbol{\Theta}^{H}\Delta\mathbf{M}\boldsymbol{\Theta}\vec{\beta}_{mis}\,.\end{aligned} \tag{4.9}$$

The orthogonality property in Eq. (4.9) can only be fulfilled when $\Delta\mathbf{M}$ is zero and based on that, this automatically implies that no mistuning is attributed to the mass. If the premultiplied and on the tuned mode shapes projected stiffness perturbation is expressed as $\hat{\mathbf{P}}$,

$$\hat{\mathbf{P}} = \frac{\boldsymbol{\Theta}^{H}\Delta\mathbf{K}\boldsymbol{\Theta}}{m^{*}}\,, \tag{4.10}$$

then Eq. (4.7) simplifies to

$$\Big(\boldsymbol{\Omega}^{2} + \hat{\mathbf{P}}\Big)\vec{\beta}_{mis} = \omega^{2}\vec{\beta}_{mis}\,. \tag{4.11}$$

The remaining difficulty of the eigenproblem is dedicated to quantify $\hat{\mathbf{P}}$ in terms of a frequency deviation.

When the perturbation of the bladed disk is confined within individual sectors, $\Delta\mathbf{K}$ become a diagonal matrix. Consequently, the entries of $\hat{\mathbf{P}}$ can be rewritten as

$$\hat{P}_{k,l} = \frac{1}{m^{*}}\vec{\Theta}_{k}^{H}\begin{bmatrix}\Delta K_0 & 0 & ... & 0\\ 0 & \Delta K_1 & ... & 0\\ \vdots & \vdots & \ddots & \vdots\\ 0 & 0 & .... & \Delta K_{N-1}\end{bmatrix}\vec{\Theta}_{l}\,. \tag{4.12}$$

The indices k and l in Eq. (4.12) range from 0 to $(N-1)$. The next step is to split the eigenvector according to

$$\vec{\Theta} = \Big[\vec{\Theta}_0 + \vec{\Theta}_1 + ... + \vec{\Theta}_{N-1}\Big] \tag{4.13}$$

$$\vec{\Theta}^{H} = \Big[\vec{\Theta}_0^{H} + \vec{\Theta}_1^{H} + ... + \vec{\Theta}_{N-1}^{H}\Big] \tag{4.14}$$

where each single eigenvector of $\vec{\Theta}$ and $\vec{\Theta}^{H}$ specifies the displacement of a particular DOF. This allows to look at each DOF separately and thereupon, considering only the mistuning in one sector, e.g.

sector 0, Eq. (4.12) becomes

$$\frac{1}{m^*}\vec{\Theta}_k^H \begin{bmatrix} \Delta K_0 & 0 & ... & 0 \\ 0 & 0 & ... & 0 \\ \vdots & \vdots & \ddots & \vdots \\ 0 & 0 & .... & 0 \end{bmatrix} \vec{\Theta}_{mis} = \frac{1}{m^*}\vec{\Theta}_{k,0}^H \Delta\mathbf{K}_0 \vec{\Theta}_{l,0}\,. \tag{4.15}$$

Equation (4.15) is valid since the perturbation is confined and the equations of motion are decoupled for each blade in the traveling wave space. Repeating this step for every sector, i.e. individual perturbation of each sector, the entries of the structural mistuning matrix $\hat{P}_{k,l}$ can be expressed as a sum over all sectors

$$\hat{P}_{k,l} = \frac{1}{m^*}\sum_{i=0}^{N-1} \vec{\Theta}_{k,i}^H \Delta\mathbf{K}_i \vec{\Theta}_{l,i}\,. \tag{4.16}$$

As done for the tuned configuration in Sect. 2.2, Lane's theorem says that each mode shape of a sector i is the phase-shifted eigenvector of the 0^{th} sector. Using this theorem, Eq. (4.16) can be simplified to

$$\hat{P}_{k,l} = \frac{1}{m^*}\sum_{i=0}^{N-1} exp\left(j(k-l)\frac{2\pi i}{N}\right)\vec{\Theta}_{k,0}^H \Delta\mathbf{K}_i \vec{\Theta}_{l,0}\,. \tag{4.17}$$

Since the tuned sector modes $\vec{\Theta}_{k,0}$ and $\vec{\Theta}_{l,0}$ of the k^{th} and l^{th} standing or traveling wave mode, respectively, are part of an isolated family of nodes, they can be approximated by an average sector mode $\vec{\Theta}_b$. The difference between the amplitudes, i.e. strain energy, of an averaged sector mode and $\vec{\Theta}_{k,0}$ as well as $\vec{\Theta}_{l,0}$ is the product of $1/\sqrt{N}$ and a scaling factor which is given by the ratio of the k^{th} and l^{th} tuned natural frequencies to the averaged natural frequency ω_b squared. Applying the average sector mode approximation to Eq. (4.17), the entries of the structural mistuning matrix can be rewritten as

$$\hat{P}_{k,l} = \frac{1}{m^*}\sum_{i=0}^{N-1} exp\left(j(k-l)\frac{2\pi i}{N}\right)\frac{\omega_k^0\omega_l^0}{N\omega_b^2}\vec{\Theta}_b^H \Delta\mathbf{K}_i \vec{\Theta}_b\,. \tag{4.18}$$

This approximation might be crucial for applying the FMM to bladed disks with strong structural coupling or shrouded bladed disks, because their strain energy of modes corresponding to different nodal diameter might vary considerably. Utilizing the Rayleigh quotient for each sector i and dropping higher order terms, allows to establish a relation between the fractional change of frequency $\Delta\omega_{mis}$ and the stiffness perturbation $\Delta\mathbf{K}_i$

$$\begin{aligned} \left(\omega_b(1+\Delta\omega_{mis})\right)^2 &= \frac{\vec{\Theta}_b^H(\mathbf{K}_b+\Delta\mathbf{K}_i)\vec{\Theta}_b}{\vec{\Theta}_b^H\mathbf{M}_b\vec{\Theta}_b} = \omega_b^2 + \frac{\vec{\Theta}_b^H\Delta\mathbf{K}_i\vec{\Theta}_b}{\vec{\Theta}_b^H\mathbf{M}_i\vec{\Theta}_b} \\ &= \omega_b^2 + \vec{\Theta}_b^H\Delta\mathbf{K}_i\vec{\Theta}_b\mathbf{I}^{-1} = \omega_b^2 + \vec{\Theta}_b^H\Delta\mathbf{K}_i\vec{\Theta}_b \\ \rightarrow 2\omega_b^2\Delta\omega_{mis} &\approx \vec{\Theta}_b^H\Delta\mathbf{K}_i\vec{\Theta}_b \end{aligned} \tag{4.19}$$

where $\mathbf{K}_b$ and $\mathbf{M}_b$ are the stiffness and mass matrices of the averaged sector respectively. Since higher

order terms are dropped, the mistuning amplitude or fractional change in frequency should be relatively small. Introducing Eq. (4.19) into Eq. (4.18) results in

$$\hat{P}_{k,l} = \frac{1}{m^*} \frac{2\omega_k^0 \omega_l^0}{N} \sum_{i=0}^{N-1} exp\left(j(k-l)\frac{2\pi i}{N}\right) \Delta\omega_{mis,i}\,. \tag{4.20}$$

It can be deduced from Eq. (4.20) that each summation is performed over the diagonal of $\hat{P}_{k,l}$ and equals the discrete Fourier transform $\Delta\tilde{\omega}_{mis,l}$ of the mistuning pattern

$$\Delta\tilde{\omega}_{mis,l} = \frac{1}{N} \sum_{i=0}^{N-1} exp\left(\frac{-j2\pi li}{N}\right) \Delta\omega_{mis,i}\,. \tag{4.21}$$

Considering this fact, the mistuning matrix can be rewritten as

$$\hat{\mathbf{P}} = 2\mathbf{\Omega} \begin{bmatrix} \Delta\tilde{\omega}_{mis,0} & \Delta\tilde{\omega}_{mis,1} & ... & \Delta\tilde{\omega}_{mis,N-1} \\ \Delta\tilde{\omega}_{mis,N-1} & \Delta\tilde{\omega}_{mis,0} & ... & \Delta\tilde{\omega}_{mis,N-2} \\ \vdots & \vdots & \ddots & \vdots \\ \Delta\tilde{\omega}_{mis,1} & \Delta\tilde{\omega}_{mis,2} & .... & \Delta\tilde{\omega}_{mis,0} \end{bmatrix} \mathbf{\Omega} = 2\mathbf{\Omega}\Delta\tilde{\mathbf{\Omega}}\mathbf{\Omega}\,. \tag{4.22}$$

$\Delta\tilde{\mathbf{\Omega}}$ in Eq. (4.22) is circulant and its component in the l^{th} traveling wave number couples the k^{th} traveling wave with the $(k \pm l)^{th}$ traveling wave. Finally, the aim to quantify the mistuning matrix $\hat{\mathbf{P}}$ is achieved and by inserting Eq. (4.22) into Eq. (4.11), the result becomes

$$\left(\mathbf{\Omega}^2 + \hat{\mathbf{P}}\right)\vec{\beta}_{mis} = \left(\mathbf{\Omega}^2 + 2\mathbf{\Omega}\Delta\tilde{\mathbf{\Omega}}\mathbf{\Omega}\right)\vec{\beta}_{mis} = \omega^2\vec{\beta}_{mis}\,. \tag{4.23}$$

4.2 Aeroelastic Analysis

To determine the aeroelastic stability of the system, another input, the tuned aerodynamic influence coefficients, are required for the FMM. They can be obtained from unsteady CFD calculations for each inter-blade phase angle in traveling wave space or in physical space, by shaking the reference blade in the desired mode shape and measuring the modal forces on the other blades. In the latter procedure, a discrete Fourier transformation gives the harmonic coefficients in the TW space.

The modal aeroelastic equation of motion in traveling wave space without external forces is

$$m^*\left[\mathbf{\Omega}^2 + \hat{\mathbf{P}} - \omega_{a,\sigma_n}^2\mathbf{I}\right]\vec{\beta}_{mis} = \vec{\hat{G}}\,. \tag{4.24}$$

To take into account aerodynamic asymmetries, the modal forces are expressed by summing the symmetric (tuned) $\mathbf{A}_{\sigma_n}^0$ and asymmetric (mistuned) aerodynamic matrices $\hat{\mathbf{A}}_{\sigma_n}$ as

$$\vec{\hat{G}} = \mathbf{A}_{\sigma_n}\vec{\beta}_{mis} = \left(\mathbf{A}_{\sigma_n}^0 + \hat{\mathbf{A}}_{\sigma_n}\right)\vec{\beta}_{mis}\,. \tag{4.25}$$

Inserting Eq. (4.25) in Eq. in (4.24), an aeroelastic eigenvalue problem is formed

$$\left|\mathbf{\Omega}^2 + \hat{\mathbf{P}} - \hat{\mathbf{A}}^0_{\sigma_n}/m^* - \hat{\mathbf{A}}_{\sigma_n}/m^* - \omega^2_{a,\sigma_n}\mathbf{I}\right| = \vec{0} \tag{4.26}$$

and the aerodynamic damping can be calculated by

$$\zeta = \frac{\Im(\omega_{a,\sigma_n})}{\Re(\omega_{a,\sigma_n})}\,. \tag{4.27}$$

5 Case Description and Numerical Setup

Bladed disks in turbomachinery applications have a high mass to air ratio which implies that the structural terms are comparatively large in comparison to the aerodynamic work. Consequently, this leads to a great simplification for studying aeroelastic systems: The structural and aerodynamic parts can be treated decoupled for the most of the cases where the blades are relatively stiff. When such a simplification can be made, the structural eigenmodes are determined assuming no-flow (i.e. vacuum) or steady-flow conditions, while the aerodynamic contribution to stability is obtained from a purely unsteady aerodynamic analysis [13]. This is in consistency with the energy method discussed in Sect. 2.3.

5.1 Case Description and Characteristics

The test case is a high aspect ratio aeronautical low-pressure turbine with a z-shape interlock shroud and 146 blades as depicted in Fig. 5.1. The bladed disk was designed as part of the FUTURE (Flutter Free Turbomachinery Blades) project which is an European project aiming at improving and validating current state-of-the-art prediction tools for flutter in turbomachines. The studied blade geometry is representative of a modern low-pressure turbine with high deflection, high lift blading and high subsonic Mach number at the exit. The inlet and exit Mach number as well as the Reynolds number based on the semi-chord at the half-span location are listed in Tab. 5.1. As part of the FUTURE test

Table 5.1: Aerodynamic Parameters of the Test Case

Design inlet Mach number	**Design exit Mach number**	**Reynolds number**
0.44	0.75	$1.35 \cdot 10^5$

campaign, a cantilevered bladed disk and the interlock configuration sharing the same airfoil shape and aerodynamic loading were experimentally investigated at Centro de Tecnologías Aeronauticas (CTA) in Spain. Despite all the efforts that were undertaken to design an unstable rotor within the constraints of the facility, flutter was not observed during the experiments. It was concluded that the interlock possibly stabilizes the system due to non-linear friction of the system. In addition, it was shown that the mechanical damping changes significantly with the rotational shaft speed. More details about the FUTURE project and the test campaign can be found in the project summary report [65].

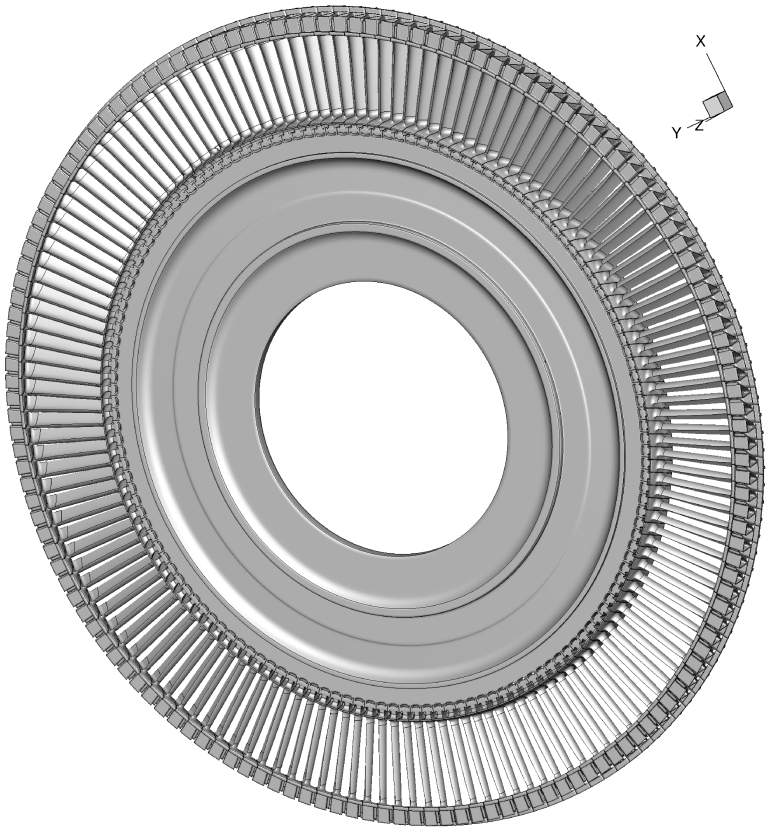

Figure 5.1: Geometry of the Whole CTA Interlock Low-Pressure Turbine Rotor

The FE mesh and the geometry of one sector of the CTA turbine is shown in Fig. 5.2. The disk is made of a martensitic steel whereas the material of the blade is an aluminium alloy. At the top of the blade a mass is added and the material of the mass holder as well as the mass itself is a stainless steel. Since the bladed disk was externally excited during the experiment, a magnet is fixed in the vicinity of the additional mass. The mechanical properties of the single materials normalized with respect to the aluminum alloy are shown in Tab. 5.2.

Table 5.2: Normalized Material Properties of the CTA Interlock Low-Pressure Turbine

	Young's modulus	**Poisson's ratio**	**Density**
Martensitic steel	2.79	0.91	2.74
Aluminium alloy	1	1	1
Stainless steel	1.30	0.91	2.88
Magnet material	2.09	0.91	2.63

The flutter analysis within this thesis will be performed for the first mode family of the shrouded bladed disk. Because of the strong structural coupling due to the interlock, the first family is a flex-dominated mode for low harmonics and changes to a torsion mode for higher harmonics. In addition

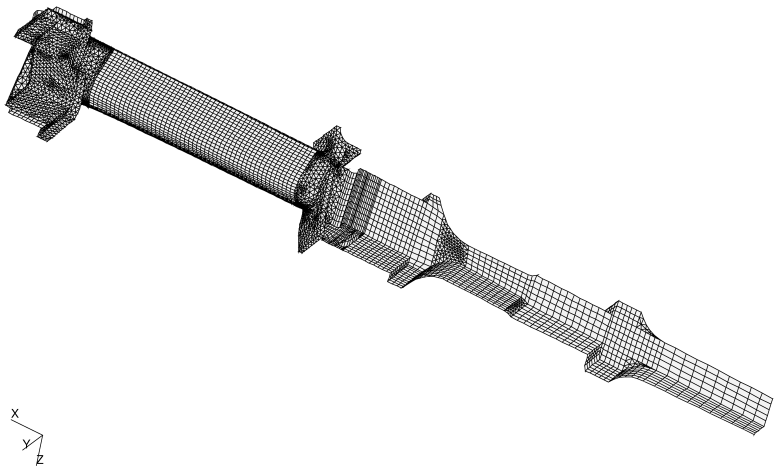

Figure 5.2: FE Mesh of One Sector of the CTA Interlock Low-Pressure Turbine

to the shrouded bladed disk, a cantilevered configuration is analyzed to have a direct comparison between a structurally weakly coupled and a strongly coupled bladed disk. At this point, a clear distinction should be made between the coupling of the fluid-structure interaction and the structural coupling. As already briefly mentioned in Sect. 1.2, the term coupling does not refer to the strength of the fluid-structure interaction but solely to the structural coupling within this thesis. In fact, both the cantilevered as well as the shrouded case are weakly coupled in terms of the numerical modeling approach for the fluid-structure interaction due to their high mass to air ratio. So both cases are equally modeled regarding their aeroelastic behavior but their is a considerable difference in the results of the modal analysis.

Furthermore, the thesis focuses on an alternate mistuning pattern which means that every second blade is mistuned in the same manner. A proportional alternate mistuning is chosen at first place and implemented by physically varying the Young's moduli of all materials by the same factor. The scaling of the Young's moduli results in a change in structral frequency so that a direct comparison to the FMM, which use a frequency deviation as the input, can be made. The same effect of frequency variation can be achieved by globally varying the density but a global scaling of the Young's moduli is chosen here without any preference. The impact or physical effects of both scaling procedures are different. On the one hand, varying the Young's moduli has a greater impact on the blade root since the bending or torsion moment is the greatest at this blade location. On the other hand, scaling the density would have almost no impact on the blade root but a high effect on the blade tip where the displacement and therefore the momentum is the highest. This considerations are of importance when the effects of mistuning, for instance, due to uneven wear at the tip should be studied so that a local variation of the mass is preferable. When the geometry variation due to manufacturing tolerances is the focus of the study and it is assumed that the most challenging area is the radius at the blade root, locally altering the Young's modulus should be favored. Anyhow, a global scaling is chosen in the present case since no specific type of mistuning is studied but rather the general behavior and the differences between a structurally strongly and weakly coupled bladed disk.

Alternate mistuning is often analyzed since it is widely accepted that an alternate pattern has a stabilizing effect on flutter [24, 64, 66]. Additionally, by considering an alternating pattern, the computational cost can be kept relatively low as it is explained in Sect. 5.3 or 5.4. When random mistuning would be considered, full rotor modal analyses and aeroelastic computations are required which increase considerably the computational demand and time.

5.2 Numerical Approach

The following section describes the setup of the FE model including a single sector and a two sector model since the latter is used for the implementation of the alternate mistuning pattern. While CFD results, i.e. mesh convergence, as well as the tuned and mistuned susceptibility to flutter are presented in Chap. 6, intermediate findings, i.e. modal analysis results, will already be shown here. All results are normalized due to proprietary reasons and hence, no absolute values are shown.

Previous studies have shown that the steady aerodynamic forces might have a considerable stiffening effect on the blade. However, the studies were performed on flexible fan blades and the effect on the frequencies and eigenvectors were relatively small. For massive blades, such as the CTA low-pressure turbine blade, the aerodynamic stiffening will be even smaller. In addition, the mapping of the pressure forces on the FE mesh can be quite challenging and therefore, taking into account the above arguments, the static aerodynamic forces are not included in the FE analysis in the present case. Furthermore, since the considered ROM has its input from the FE analysis, omitting the steady aerodynamic forces in the FE analysis produces a small error compared to fully-coupled aeroelastic computations but would not compromise the proof of accuracy of the ROM.

5.2.1 Structural Analysis for the Shrouded Bladed Disk

The structural and modal analyses are performed in the multidisciplinary finite element analysis solver Nastran. The preparation of the finite element mesh as well as other preprocessing task are done in Patran. The FE mesh was not created as part of this thesis since it was already present before and was used for several analyses which were not externally published. The results of tuned modal analysis of this thesis are compared against available unpublished FUTURE projectt results and the thesis results are proven to be reliable. For that reason, no mesh sensitivity study for the modal analysis is conducted.

The FE mesh shown in Fig. 5.2 of the one sector model has in overall 22,968 nodes resulting in 46,424 solid elements consisting of 31,615 tetrahedral, 4,982 wedge and 9,827 hexahedral elements with linear shape functions. The tetrahedral elements are mainly placed in the vicinity of the blade shroud and at the lower section of the blade. The blade leading and trailing edge and some areas of the disk are meshed with wedge elements. Rectangular hexagons are utilized for the mass, magnet, massholder, the straight geometry of the airfoil and the rest of the disk. Due to the complex geometry of the bladed disk, it is convenient to use different finite element types so that an acceptable mesh quality and connectivity can be achieved while keeping the total number of nodes as low as possible.

Two sets of boundary conditions are applied: Firstly, the nodes at the flange, which is located at the leading edge side of the disk, are fixed in all 6 directions (3 translations, 3 rotations) so that rigid body modes are prevented. Secondly, a cyclic symmetry boundary condition is applied between the dependent and the independent surface of the disk and at the shroud interface. Consequently, 9 nodes at the z-shape shroud geometry are relatively fixed between each other resembling a full-stick condition at the interlock. The dependent and independent regions are surfaces with a $(360° \, S)/N$ angle in between the two areas in the circumferential direction where S is the number of bladed disk sectors implemented in the FE model. The dependent region always has a higher angle around the z-axis according to the right hand rule than the independent region. When a different coordinate system is used compared to the one in Fig. 5.2, the axis has to be adequately adjusted. The cyclic symmetry boundary condition automatically adjusts the phase-angle between the dependent and independent based on the chosen analyzed harmonic. Apart from that, a centrifugal load is globally applied to all nodes representing the rotation of the shaft speed. The bladed disk may experience a centrifugal stiffening or softening effect due to thermal effects while the former is observed for the CTA interlock configuration at the nominal speed compared to a shaft at rest.

The normalized structural frequency versus the harmonic index h_{FEM} specified in Nastran for different mode families is shown in Fig. 5.3. It can be observed that the first mode family (connected

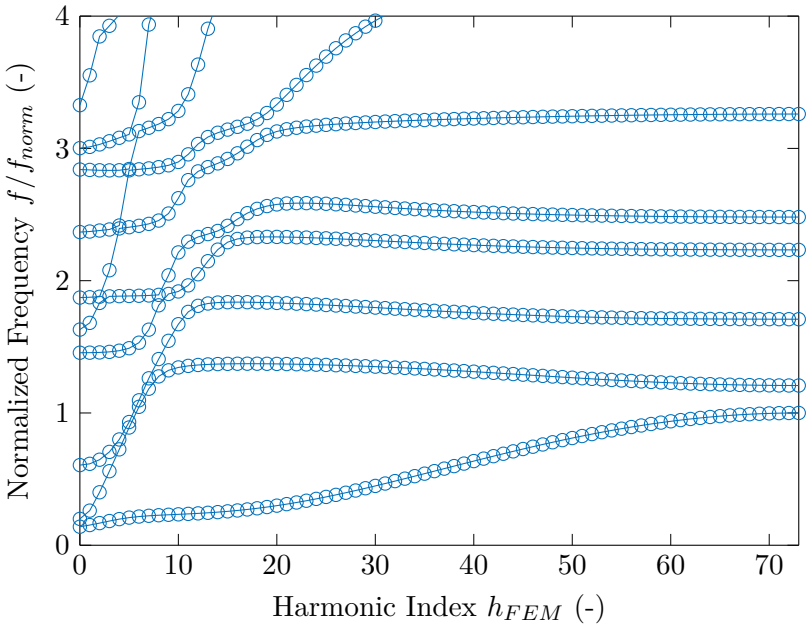

Figure 5.3: Normalized Natural Frequencies versus Nodal Diameter for the Shrouded Bladed Disk

dots with lowest frequencies) is close to the second family at low and high harmonic indices. There are several veering and crossing regions between higher mode families, especially in the region around a harmonic index of 10. The first family is more or less well separated from the others and consequently, the FMM may produce reasonable results. However, it should also be kept in mind that the first mode family also experiences a relatively high variation of frequency as a function of the harmonic index in

conjunction with a blade-alone mode shape change from flex to torsion. This violates the assumption of FMM that all mode shapes can be approximated by an average mode shape if the modes do not significantly change with the harmonic index as this is not true for the present case.

A linear modal analysis is conducted which outputs the structural eigenfrequencies as shown in Fig. 5.3 and eigenvectors. The computation is linear in the sense that the whole centrifugal load is applied in one step and based on that, the stiffness matrix is updated once prior to the modal analysis. On the other hand, in a non-linear analysis, the centrifugal load is incrementally increased and in each step, a balance between the internal and external forces is assured through the Newton-Raphson approach resulting in an update of the stiffness matrix after each iteration. It is worth to mention that the relation between displacement and force is linear according to Hooke's law but this is not true for centrifugal load balancing so that a non-linear analysis might be required for flexible blades. Nevertheless, it is not expected to be necessary for the considered case here since the blade is comparatively stiff and in consequence, a linear modal analysis is regarded to be sufficient. Yet, a comparison between the linear and non-linear analysis should be performed to verify the assumption, which is shown for the 0^{th} harmonic index in Fig. 5.4. The normalized frequencies of different system

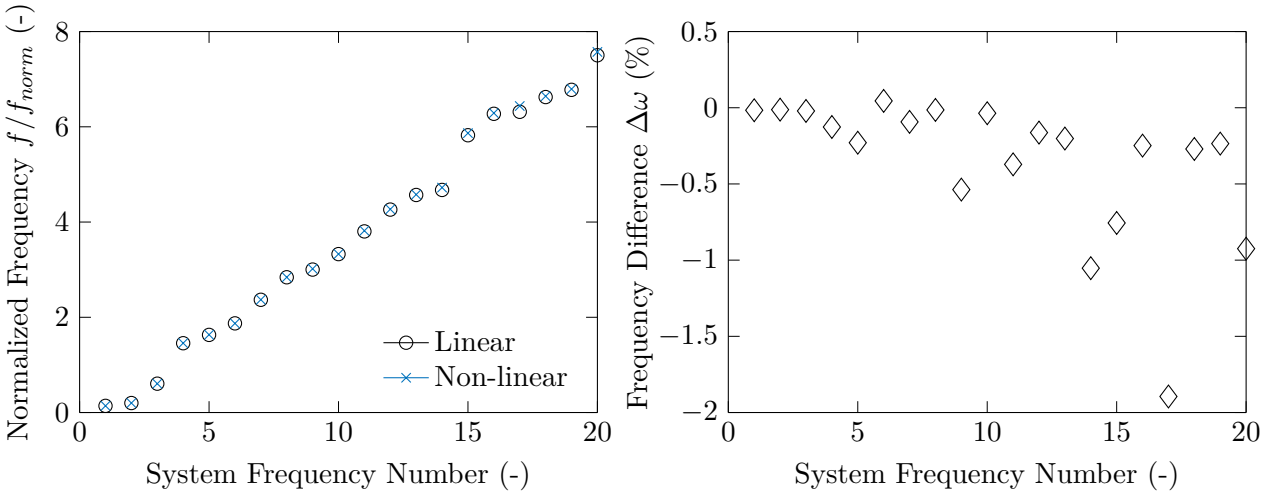

(a) Frequency **(b)** Frequency Difference

Figure 5.4: Comparison of a Linear and a Non-Linear Calculation for the 0^{th} Harmonic Index for an One Sector Model of the Shrouded Configuration

frequency numbers or mode families are depicted in Fig. 5.4a for the linear and non-linear approach and the relative difference between these two in Fig. 5.4b. The frequency difference is less than 0.5% for a system frequency number below 5 whereas the flutter analysis should be performed for the first mode family where the difference is even lower than 0.1%. The preprocessing steps of the non-linear approach are more complicated and the CPU time is higher so that a linear analysis is preferred.

In all the analyses, material damping is set to zero because it is unknown for the current rotor configuration. Material damping would act in a favorable way regarding the system stability so that the presented approach can be seen as a conservative one.

5.2.2 Structural Analysis for the Cantilevered Bladed Disk

In order to analyze the cantilevered configuration, which is representative of a structurally weakly coupled system, the cyclic symmetry boundary condition at the shroud interface is removed while the overall geometry is kept the same. By removing the cyclic symmetry boundary condition at the shroud interface, the blades are free to move independently of each other. Similar to the (strongly coupled) shrouded configuration, the first mode family is considered which is a pure flex mode for the cantilevered bladed disk.

There are two considerable differences in the modal results between the cantilevered and the shrouded case. Firstly, there is not such a great variation in the structural frequency over the harmonic index as can be seen for the cantilevered case in Fig. 5.5 compared to a structurally strongly coupled bladed disk in Fig. 5.3. Secondly, while there is a transition from a predominantly bending mode to a predominantly torsion mode for the shrouded case, the bending mode remains almost the same for the cantilevered case.

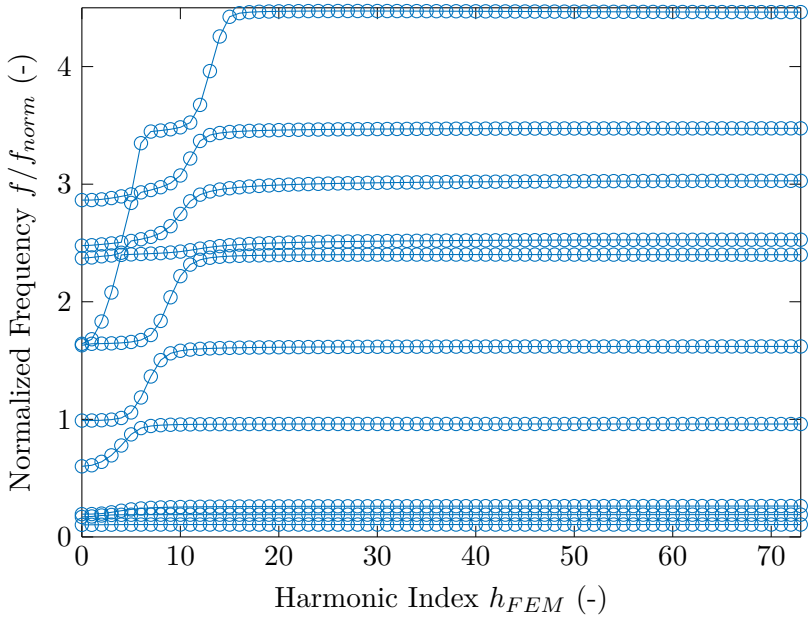

Figure 5.5: Normalized Natural Frequencies versus Nodal Diameter for the Cantilevered Bladed Disk

5.2.3 Flow Solver and CFD Mesh

In order to perform an unsteady flutter calculation, a steady-state result of the flow field is needed. The steady-state computations are conducted with the non-linear solver TRACE which solves the Reynolds Averaged Navier-Stockes equations (RANS). TRACE is an DLR finite volume in-house code for turbomachinery applications that was used and validated over years with support from several German universities and industrial partners.

Flutter simulations require an unsteady approach which can be an explicit or implicit solution of the time-dependent flow equations also known as time accurate approaches. Explicit schemes need a suffi-

ciently small time discretization to guarantee accurately enough gradient approximations while implicit schemes solve several time-dependent equations simultaneously which is computationally demanding. Therefore, in order to save computational time, the flow solver used throughout the unsteady flutter calculation is linearTRACE which is a time-linearized Unsteady Reynolds Averaged Navier-Stockes (URANS) solver [67]. The time-linearized code was successfully applied to many cases, see for instance in recent publications [68] or [69], and should be explained briefly here based on the work of May [12].

The utilized time-linearized solver is actually a forced motion calculation which means that a harmonic motion is enforced in a steady fluid flow. For that reason, the aeroelastic angular frequency ω_{a,σ_n} is approximated by the structural frequency ω_{σ_n} and no correction of the harmonic oscillation frequency is taken into account. Using the Arbitrary-Lagrangian-Euler formulation, the Navier-Stokes equations of the decoupled fluid-structure problem can be rewritten in a semi-discrete form (space but not time discretized) for every individual volume cell

$$\frac{\partial(V\vec{U})}{\partial t} + \vec{R}(\vec{U},\vec{x},\dot{\vec{x}}) = \vec{0}\,. \tag{5.1}$$

V is the cell volume, $\vec{U}$ the vector of conservative flow variables and $\vec{R}$ the residual vector containing the numerical flux variables. Assuming small perturbations amplitudes, which is sufficient to calculate the onset of flutter, the CFD mesh vertices as well as other flow variables can be decomposed into a steady, time-independent and a time-dependent harmonic perturbation as follows

$$\vec{x}(t) \approx \vec{x}_0 + \Delta\vec{x}(t) = \vec{x}_0 + \Re\Big(\hat{\vec{x}}(\vec{x}_0)e^{j\omega t}\Big) \tag{5.2}$$

$$\vec{U}(\vec{x}_0,t) \approx \vec{U}_0(\vec{x}_0) + \Delta\vec{U}(t) = \vec{U}_0(\vec{x}_0) + \Re\Big(\hat{\vec{U}}(\vec{x}_0)e^{j\omega t}\Big)\,. \tag{5.3}$$

Expanding the non-linear residual vector $\vec{R}$ with a Taylor series around the steady-state solution (denoted by the subscript 0) and dropping higher order terms results in a linear expression of the numerical flux variables

$$\vec{R}(\vec{U},\vec{x},\dot{\vec{x}}) \approx \vec{R}(\vec{U}_0,\vec{x}_0,\vec{0}) + \frac{\partial R}{\partial U}\bigg|_{\vec{U}_0,\vec{x}_0,\vec{0}}\Delta\vec{U} + \frac{\partial R}{\partial x}\bigg|_{\vec{U}_0,\vec{x}_0,\vec{0}}\Delta\vec{x} + \frac{\partial R}{\partial \dot{x}}\bigg|_{\vec{U}_0,\vec{x}_0,\vec{0}}\Delta\dot{\vec{x}}\,. \tag{5.4}$$

For a well converged steady-state solution, the residual vanishes so that the first term on the right hand side of Eq. (5.4) is approximately, $\vec{R}(\vec{U}_0,\vec{x}_0,\vec{0}) \approx 0$. Taking into account this approximation and inserting Eq. (5.4) in conjunction with Eqn. (5.2) and (5.3) into Eq. (5.1) gives a complex linear system of equations

$$\left(j\omega V_0\hat{\vec{U}} + j\omega\hat{V}\vec{U}_0 + \frac{\partial R}{\partial U}\bigg|_0\hat{\vec{U}} + \frac{\partial R}{\partial x}\bigg|_0\hat{\vec{x}} + \frac{\partial R}{\partial \dot{x}}\bigg|_0 j\omega\hat{\vec{x}}\right)e^{j\omega t} = \vec{0} \tag{5.5}$$

which can be further simplified to

$$\left(j\omega V_0 \vec{I} + \left.\frac{\partial R}{\partial U}\right|_0\right)\hat{\vec{U}} = -\left(\left.\frac{\partial R}{\partial x}\right|_0 \hat{\vec{x}} + \left.\frac{\partial R}{\partial \dot{x}}\right|_0 j\omega\hat{\vec{x}} + j\omega\hat{V}\vec{U}_0\right). \tag{5.6}$$

The final result, Eq. (5.6), enables the direct calculation of the unsteady flow variables, i.e. linear system of equations, which is considerably faster than solving the flow field using a time-accurate approach. However, there are two main drawbacks of the linearized system due to the assumption of small perturbation amplitudes: Firstly, transient effects cannot be taken into account since a harmonic motion is enforced and as a consequence, the flow solution is also harmonic. Secondly, the perturbations have to remain small which makes it difficult to get an accurate solution when non-linearities, such as shocks or separated flow, appear.

All steady-state simulations are computed with the two-equations Wilcox $k-\omega$ turbulence model [70]. Since the turbulence model has not been linearized yet, a constant viscosity approach is used for the unsteady computations. For the steady-state as well as the unsteady computations, a low Reynolds approach is utilized at the airfoil boundaries. Since it is cumbersome to resolve the boundary layer in detail and to achieve an appropriate wall distance value y^+ at the hub and tip wall within a reasonable CPU time, wall functions are used at these viscous walls. While the y^+ value at the airfoil does not exceed 1, it varies at the hub and tip walls between 10 and 25. To get accurate results using wall functions the y^+ value should normally be in the range of $30 \leq y^+ \leq 300$. However, the boundary layer at the tip and hub wall is not expected to have a high impact on the flutter results. As the blade has a large aspect ratio, end-wall effects are practically negligible and the flow inside the annulus is almost two-dimensional. The steady-state TRACE solver is implicit and has a second order accuracy in space and time. For the flow field in the circumferential direction, a phase-lagged boundary condition is imposed where an inter-phase angle is enforced for each traveling wave.

The computational domain is discretized with a structured grid with areas of different mesh topologies. An O-grid is used around the airfoil surrounded by a C-grid and an H-grid is applied in the rest of the domain. The mesh is extended up- and downstream and gradually coarsened to minimize numerical reflections at the inlet and outlet.

Three different meshes are created to study the steady-state solution with respect to the mesh density. The coarse mesh is shown from the radial and tangential direction in Fig. 5.6 and 5.7 respectively.

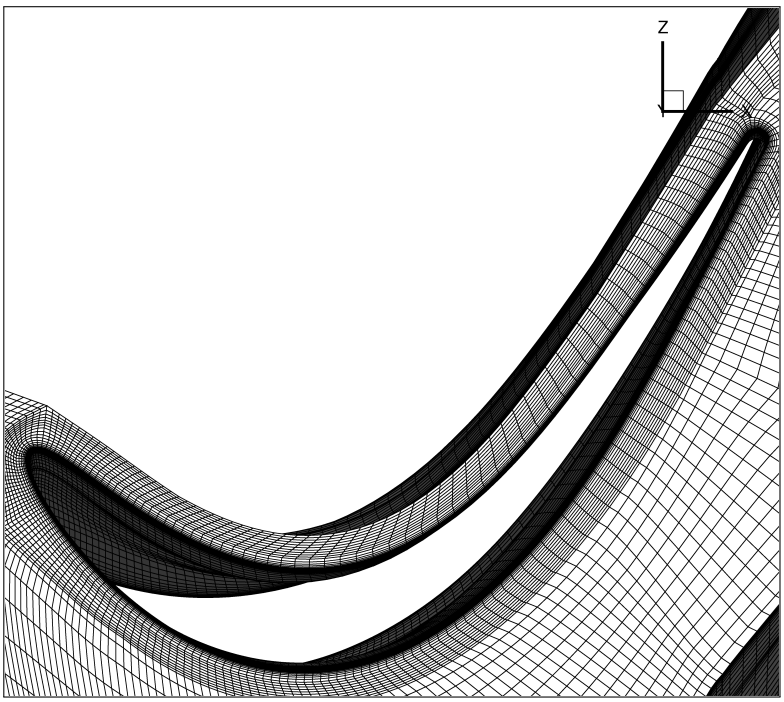

Figure 5.6: Radial View on the Coarse CFD Mesh

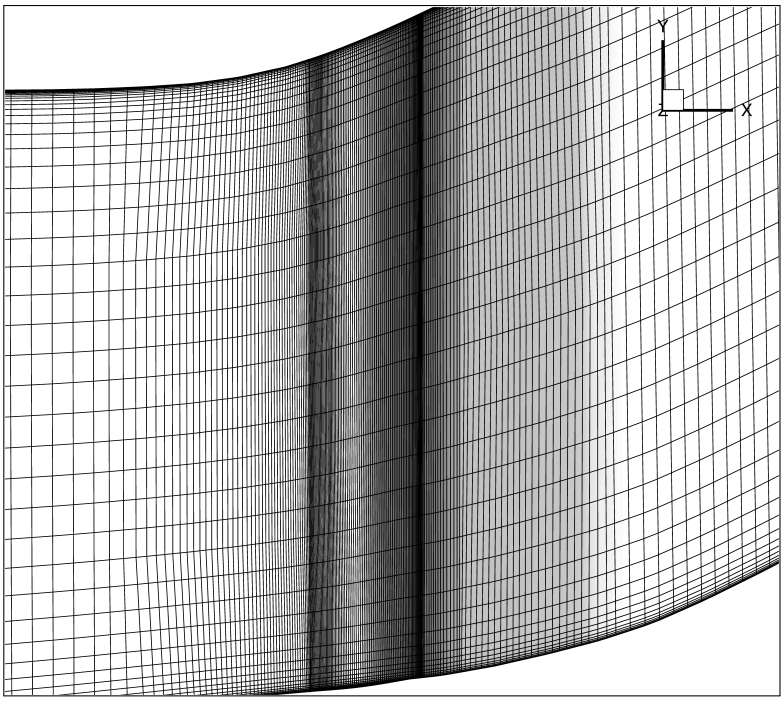

Figure 5.7: Tangential View on the Coarse CFD Mesh

The number of nodes is globally increased by about a factor of 3 between each refining step resulting in 574,812 elements for the coarse mesh, 1,659,100 for the medium and 3,778,144 elements for the fine mesh. The mesh sensitivity study is solely conducted using the steady-state results.

5.2.4 Aeroelastic Method

The aeroelastic method used for the flutter calculations is the energy method discussed in Sect. 2.3. As mentioned before, linearTRACE which utilizes the energy method is not capable to take into account the effects of the aerodynamics on the oscillation frequency nor on the modal characteristics. In consequence, the structural and fluid dynamics are completely uncoupled.

The procedure of the energy method is schematically shown in Fig. 5.8. The first step is to obtain

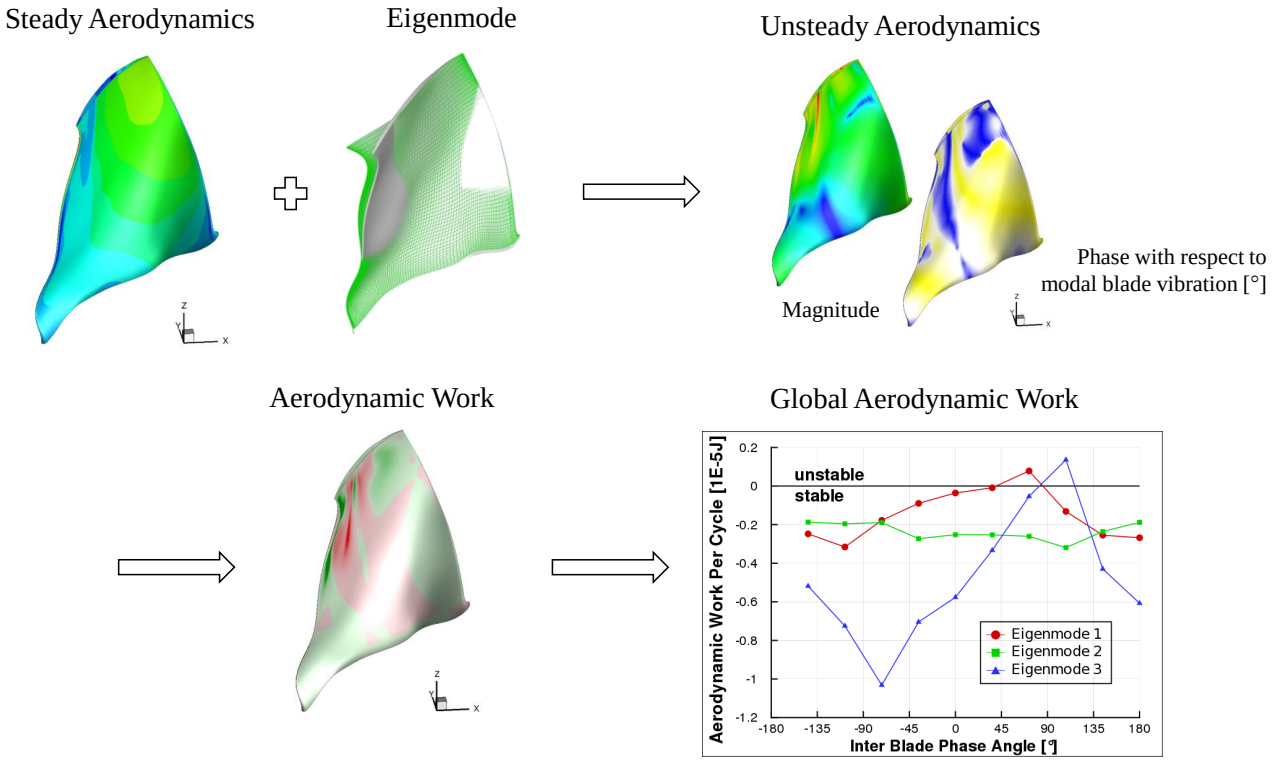

Figure 5.8: Procedure and Different Steps of the Energy Method

a converged steady-state solution of the flow field and the modal characteristics of the bladed disk as shown on the top left of Fig. 5.8. Afterwards, the aeroelastic mode shapes in the traveling wave domain have to be constructed. In the case of an even blade count, using the $N/2+1$ structural complex eigenvectors, 2 standing and $N-2$ traveling waves have to be built by two different combinations of the real and imaginary part of a particular mode shape. Since this step is not really straightforward, a brief explanation should be given for the output obtained in Nastran but the procedure can be easily generalized and is applicable for other structural solvers.

When a modal analysis with cyclic symmetry is performed in Nastran, the output for each harmonic consists of two eigenvectors with exactly the same structural frequency. One of the eigenvectors is the real part of the aeroelastic mode shape and the second one the complex part. Two questions arise, namely, which structural mode shape is the real part of the aeroelastic eigenform and what complex part corresponds to a positive nodal diameter? To answer this two questions, two corresponding nodes from the cyclic symmetric boundary condition — one from the independent and one from the

dependent surface — with a relatively high displacement amplitude have to be selected. Then, without any preference, one eigenvector is assumed to be the real part and the other the imaginary part, and the phase between the real and the imaginary parts is determined at the chosen nodes. It has to be taken care of that the angle lies between $-\pi$ and π. The phase of the node at the dependent surface always has to be higher than the phase of the node at the independent side. If this is not the case, the aforementioned assumption about the real and imaginary part of the eigenvector is incorrect and has to be reversed. After the reversal, the above condition should be true and the difference between the two phases is the inter-blade phase angle. When this procedure is followed correctly, a traveling wave in the positive direction of rotation (positive nodal diameter) is obtained. Consequently, the complex conjugate corresponds to the traveling wave in the negative direction. Throughout the whole thesis, the following sign convention is used: A positive nodal diameter represents a forward traveling wave, i.e. a wave in the positive direction of rotation, and a negative nodal diameter backward traveling wave.

After the traveling wave modes have been identified, the eigenvector has to be interpolated and mapped on the CFD mesh as indicated in the right top corner of Fig. 5.8. Using the linearized solver linearTRACE, the aerodynamic work on the blade surface is computed and tracked, Fig. 5.8 bottom left, until a certain convergence criterion is reached. Similar to the logarithmic decrement in Eq. (2.38), the aerodynamic damping ζ_{σ_n} can be expressed as an energy ratio of the aerodynamic work to the kinetic energy of a cascade oscillating in the n^{th} traveling wave mode,

$$\zeta_{\sigma_n} \approx \frac{\Lambda}{2\pi} = -\frac{1}{4\pi}\frac{W_{aero,\sigma_n}}{E_{kin,max}} = -\frac{1}{2\pi}\frac{\Re(W_{aero,\sigma_n})}{m^*\omega_{\sigma_n}^2}\,. \tag{5.7}$$

The procedure is repeated as many times as there are blades in the bladed disk and the aerodynamic damping can be plotted versus the nodal diameter, akin to the work per cycle versus the inter-blade phase angle plot in 5.8 bottom right, and the unstable region determined.

5.3 Implementation of Mistuning

Since an alternate mistuning pattern is utilized in this study, a two sector structural as well as CFD model is decided to be appropriate for the determination of the aeroelastic stability. When every second blade disk sector is equally mistuned, the pattern repeats after every two sectors and in consequence, a tuned system is recovered. In general, for a harmonic mistuning pattern, the number of required sectors in the computational domain equals the number of blades needed to repeat the pattern. However, the remainder of $N/(\#\,\text{sectors in one domain} \cdot \#\,\text{domains})$ has to be zero which is not always easy to implement or not possible at all. When a random mistuning pattern has to be analyzed, a full annulus structural and CFD model is necessary which is computationally expensive. To obtain the two sector model, a copy of the structural model or computational domain is rotated by $2\pi/N$, the overlapping nodes merged with the original nodes so that the number of elements is about twice of the initial one sector model. More information about the method and some issues are discussed in the next Sect. 5.4.

In order to establish a physical mistuning pattern, the Young's moduli of all the materials defined

in Tab. 5.2 are scaled simultaneously with the same factor. A prior analysis is conducted with the one sector model so that the change in Young's modulus can be quantitatively related to a change in frequency. The result is shown in Fig. 5.9 where the solid lines represent an increase in Young's modulus and the dashed lines a decrease. As can be seen from Fig. 5.9a, an increase or decrease of the

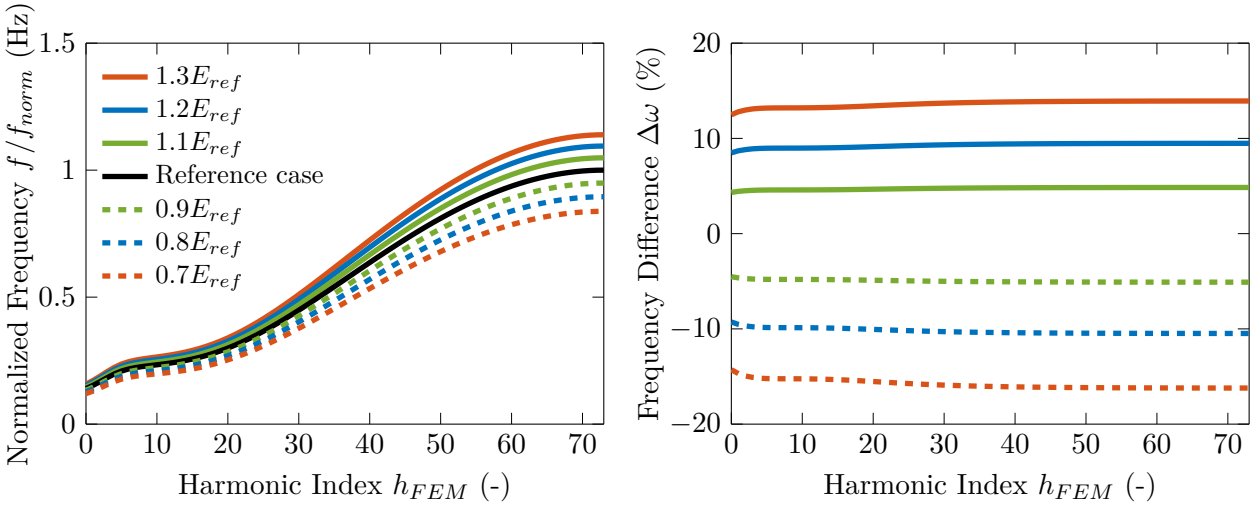

(a) Frequency **(b)** Frequency Difference

Figure 5.9: Structural Frequency Change due to the Change in Young's Modulus E for the Shrouded Configuration

Young's modulus causes the frequency curves to spread but the shapes remain the same. In many of the reduced order models, the strength of mistuning is expressed as a chance in frequency as plotted in Fig. 5.9b. The relative difference $\Delta\omega$ is always related to each specific harmonic of the reference case. Two observations can be made from Fig. 5.9b. Firstly, the frequency difference is not the same when the Young's modulus is scaled up or down. The effect of altering the Young's modulus is higher when E is reduced compared to an increase in E. Secondly, the frequency difference changes slightly for lower harmonics and gets more or less constant for higher harmonics. In the following analysis, the terms frequency difference or mistuning amplitude are an approximation of a single value. For instance, a change in the Young's modulus of 20% results in a mistuning amplitude of $\Delta\omega = 10\%$. The mistuning amplitude represents a rounded mean value of the two frequency difference curves, i.e. solid and dashed blue lines in Fig. 5.9b. However, in the actual computations, the real exact values for each harmonic is used. The mistuning amplitude is always about half of the relative change in Young's modulus.

Both points are quantitatively visible in Tab. 5.3. To give an example, an alternation of the Young's modulus of ±30% should be considered which results in a mistuning amplitude of $\Delta\omega = 15\%$. Regarding the aforementioned first point, the relative change in frequency for the 0^{th} harmonic index, $h_{FEM} = 0$, is -14.29% and 12.48% when the Young's modulus is scaled downwards or upwards, respectively. A similar behavior can be observed for the highest harmonic $h_{FEM} = 73$. Now, looking only at the downward scaling of E, i.e. $0.7E_{ref}$, the change in the structural frequency rises by about

Table 5.3: Structural Frequency Change in Percent due to the Change in Young's Modulus E for the Lower and Highest Nodal Diameter for the Shrouded Bladed Disk

	$\mathbf{0.7E_{ref}}$	$\mathbf{0.8E_{ref}}$	$\mathbf{0.9E_{ref}}$	$\mathbf{1.1E_{ref}}$	$\mathbf{1.2E_{ref}}$	$\mathbf{1.3E_{ref}}$
$\mathbf{h_{FEM} = 0}$	-14.29%	-9.27%	-4.52%	4.33%	8.45%	12.48%
$\mathbf{h_{FEM} = 73}$	-16.21%	-10.48%	-5.31%	4.85%	9.48%	13.93%

1.92% from the lowest harmonic index to the highest index.

To sum up, at this point, all the observations show that the change in the modal properties is non-linear in the present case. Therefore, a pre-analysis prior to the mistuned flutter calculations is required. Referring to the published studies using ROMs in the literature where, in most of the cases, a change in frequency is considered, it is actually not straightforward to relate the frequency change directly to the actual physical alternation.

To get a better imagination of the analyzed tuned and mistuned eigenforms, Fig. 5.10 illustrates the mode shapes of the first mode family for the 1^{st} and 72^{nd} harmonic. Although, due to the partial destruction of the cyclic symmetry, there are no real harmonic indices or nodal diameters in the mistuned configuration, the terms "equivalent mistuned harmonic" or "equivalent mistuned nodal diameter" (n_{eq}) are used throughout the analysis to represent mistuned eigenmodes that are in the same frequency range as their tuned counterparts. By looking at Fig. 5.10a, it is obvious that the lower harmonic indices are predominantly bending modes, and the higher harmonics resemble torsion modes, see Fig. 5.10b. The higher harmonic mistuned mode shape shown in Fig. 5.10d has a similar form as the tuned mode apart from being slightly amplified but the lower harmonic mistuned mode, see Fig. 5.10c, deviates considerably compared to the tuned configuration. Nevertheless, it is difficult to judge at this stage whether the deviation stems from the mistuning or from the numerical setup. It has to be kept in mind that the complex eigenform calculated by the structural solver is randomly placed in the complex space and in consequence, the computed eigenforms can be the same but with a different real and imaginary part.

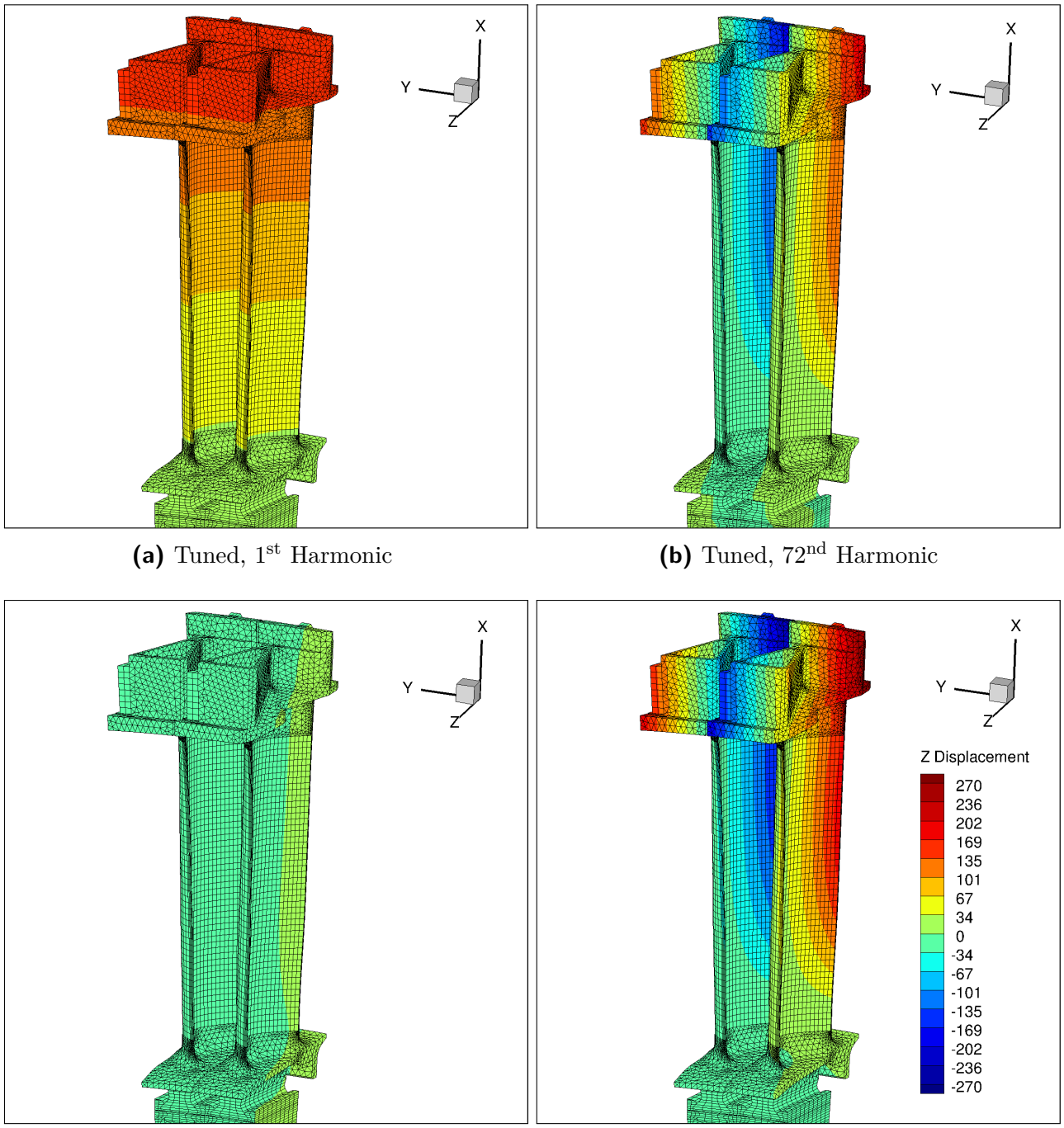

(a) Tuned, 1st Harmonic

(b) Tuned, 72nd Harmonic

(c) Equivalent Mistuned 1st Harmonic

(d) Equivalent Mistuned 72nd Harmonic

Figure 5.10: Real Displacement in Z-Direction for a Pair of Eigenvector of a Tuned and 5% Alternate Mistuned Two Sector Model of the Shrouded Bladed Disk

5.4 Two Sector Method

In this case, the one sector method consists of one modeled bladed disk sector for which 74 harmonics (0,1, ..., $N/2$) can be calculated corresponding to N distinct inter-blade phase angles (IBPA) (-177.5°, 175,1°, ..., 0°, ..., 177.5°, 177.5°, 180°). Each IBPA is a characteristic property of a traveling wave or a standing wave and every harmonic is assigned to a distinct nodal diameter.

This does not apply in the same way for the two sector method. When two blades are included into the model, the number of possible harmonics is reduced to $(N-1)/2$ for an even blade count. Consequently, the number of possible nodal diameters for the complete 2-blade sector is reduced to the same amount as the harmonics. The solution for the complete 2-blade sector consists of two different pairs of eigenmodes with its individual real and imaginary part. The second opposite pair is the actual higher harmonic of the one sector model.

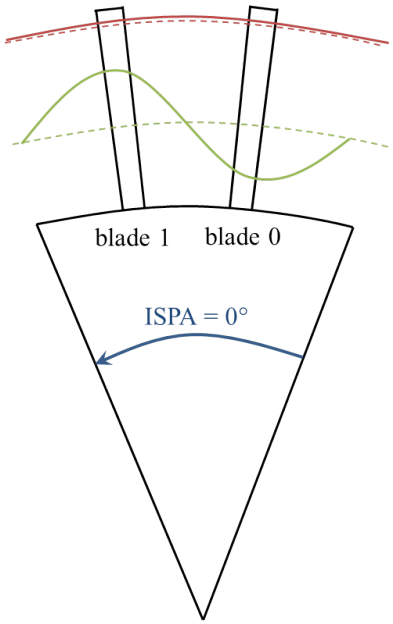

(a) Harmonic 0; Red: ISPA = 0°; Green: ISPA = 180°

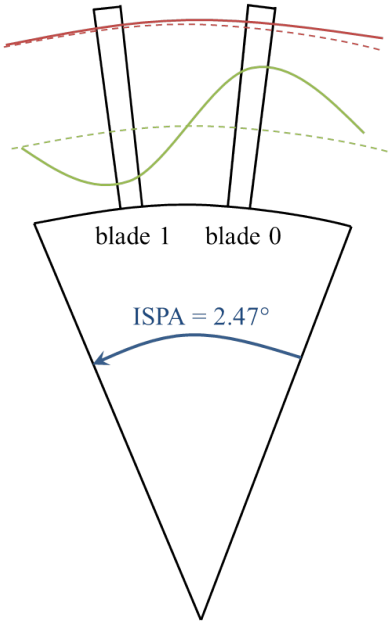

(b) Harmonic 36; Red: ISPA = 2.47°; Green: ISPA = 177.53°

Figure 5.11: Effect of Recovered Nodal Diameter of a Tuned Two Sector Model where only One Harmonic is Calculated in the Structural Model

For instance, as shown in Fig. 5.11, when the 0^{th} harmonic is specified in Nastran, the first calculated eigenmode with the lowest frequency corresponds to the harmonic 0. The same result contains higher harmonics as well and the following relationship holds for a two sector model with an even blade count N

$$n = \begin{cases} h_{FEM} & n \leq \frac{1}{2}\left(\frac{N}{2} - 1\right) \quad (5.8a) \\ \frac{N}{2} - h_{FEM} & n > \frac{1}{2}\left(\frac{N}{2} - 1\right) \quad . \quad (5.8b) \end{cases}$$

This can be explained by the fact that when the model is enlarged from one sector to two sectors, the possible numerical numbers of harmonics is also halved. Since the characteristics of the system cannot be lost, the individual two-sectors-harmonics have to contain multiple one-sector-harmonics. This methodology can be extended for models with a higher number of sectors within the numerical domain.

This effect influences the post-processing of the modal results obtained in Nastran. When a certain harmonic is specified in the Nastran solver, the output contains four eigenmodes corresponding to a real and imaginary part for both cases according to Eq. (5.8). Depending on the available structural post-processing utilities, it might get troublesome to efficiently extract all the modal information from one solution. Another approach would be to conduct a pre-calculation with the one sector model and limit the expected range of frequencies in which one eigenform is expected to appear. In the present case, the lower and higher harmonics are separated by a high frequency difference for the shrouded case but they would be calculated as one harmonic when a two sector method is used. Therefore, the solution can be separated by narrowing the expected frequency range so that two separate solutions are obtained. This methodology makes the post-processing easier and is implemented in the analysis of this thesis.

Apart from that, there are no more inter-blade phase angles but rather inter-sector phase angles (ISPA) for an alternate mistuning pattern as highlighted in Fig. 5.11 in blue. Theoretically, the inter-blade phase angle can be calculated for a tuned bladed disk but it is unknown when mistuning is present. When mistuning is present, solely the inter-sector phase angle or the phase between the dependent and independent surface is known and an inter-blade phase angle automatically establishes in the FE calculation based on the mistuning amplitude but the IBPA cannot be determined beforehand. Surely, an approximated IBPA can be calculated for the mistuned two sector method by post-processing the results of the modal analysis, but there is no direct advantage in applying an approximated IBPA in this case.

Furthermore, another issue is encountered when setting up the CFD calculations from the two sector structural model. A tuned system should be considered for which the first structural Nastran harmonic is computed, $h_{FEM} = 1$. Based on the structural solution, traveling waves corresponding to the $\pm 1^{\text{st}}$ and $\pm 72^{\text{nd}}$ nodal diameter can be constructed using the approach described in Sect. 5.2.4. Since the IBPAs are known for the tuned configuration, the phase angles inside the structure as depicted in blue in Fig. 5.12 establish. For the lower half of the harmonics, i.e. 5.8a, the resulting phases are as expected based on the preceding discussion. However, even though the inter-phase angle of the 72^{nd} nodal diameter equals the phase of the first nodal diameter, the actual IBPA has a negative sign in the modal analysis results as illustrated in the phase between the dependent and independent surface in Fig. 5.12b. This was detected by a discontinuity in the stability curves for nodal diameters corresponding to the higher half of the harmonics as stated in Eq. 5.8b. So when the simulations are set up for a positive traveling wave mode, the corresponding backward mode is actually calculated. The reason for this behavior of the Nastran solver could not be explained but the results can be easily corrected by flipping or vertically mirroring the flutter results of the higher positive and negative nodal diameter.

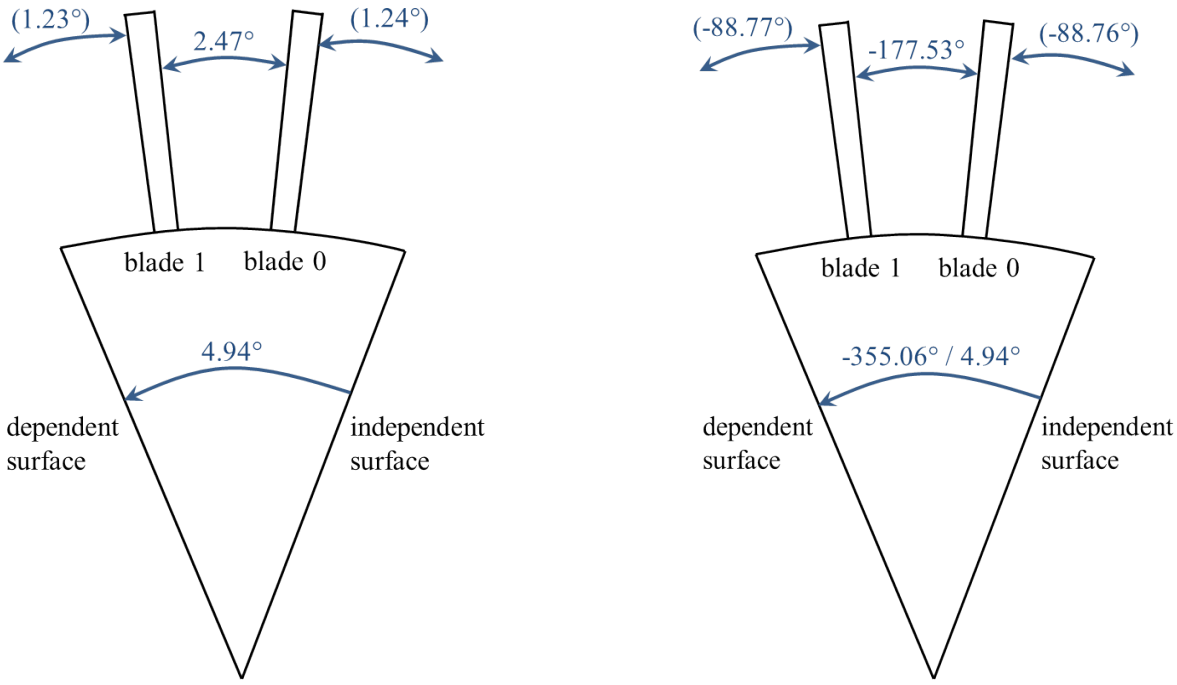

(a) Nodal Diameter 1 **(b)** Nodal Diameter (-) 72

Figure 5.12: Inter-Sector Phase Angle of a Tuned Two Sector Model as well as Phase-Lagged Boundary Conditions for CFD Calculations for a Bladed Disk with 146 Blades

To validate the setup of the two sector model and also to get a feeling for the differences between the approaches, a one sector model, a two sector model as well as a full annulus FE model are built and analyzed. The difference in frequency relative to the full annulus results are shown in Fig. 5.13 for the analyzed first mode family and also the second mode family. It can be observed from Fig. 5.13 that the relative frequency difference for the second mode family is in the same order but smaller. In general, the difference decreases with increasing harmonic index. The one as well as the two sector model agree comparatively well and the differences are acceptable.

The model size and the required CPU time for the three different structural models is listed in Tab. 5.4. It should be noted that the full rotor computations are conducted using a parallel approach with six processors and hence, the real CPU time for the full rotor model is actually considerably higher. The two sectors model requires about 37% more CPU time compared to the one sector model.

Table 5.4: Mesh Properties for the Modal Analysis with Different Amount of Cyclic Symmetric Sectors

	# Elements	# Element ratio	CPU time	CPU time ratio
1 sector model	46,424	1	30 min	1
2 sectors model	92,848	2	41 min	1.37
Full rotor model	6,777,904	146	1,077 min	35.9

When a random mistuning would be the case of study, the CPU time for the modal analysis would rise

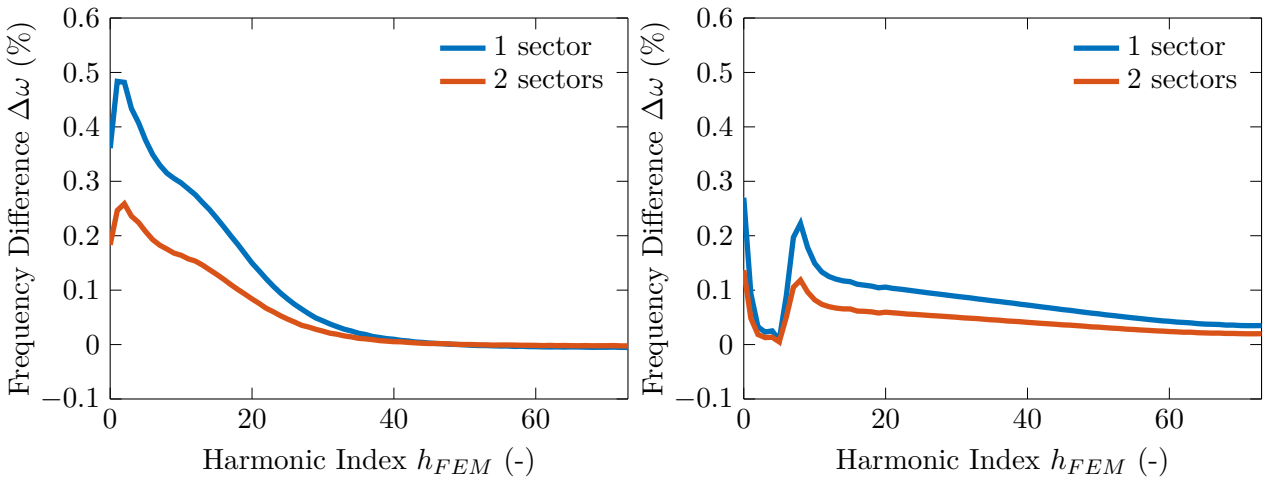

(a) 1st Blade Frequency

(b) 2nd Blade Frequency

Figure 5.13: Frequency Difference of 1 and 2 Sector Models with respect to Full Rotor Model

by about 3,490% relatively to a tuned analysis which unveils the high computional demand required to study a mistuning pattern that, for instance, is caued by manufacturing tolerances.

As a side note, while the one as well as the two sector model obtain the same frequency for the real and imaginary part of the eigenvector, there is a small difference between the frequencies for the full annulus model. However, this is not a physical phenomena but has rather a numerical background. On the one hand, for the one sector model, the Nastran cyclic symmetry solver calculates the frequency once, for instance for the real part, and copies it for the imaginary part. On the other hand, for a full annulus model, N explicit eigenvectors are computed separately without any cyclic symmetry assumption so that a small numerical error appears.

Lastly, an error has been detected at the end of this work. When the structural two sector model was created, the overlapping nodes of each sector have to be merged. This can be accomplished in Nastran by specifying a global tolerance and if the distance between overlapping node is lower, the nodes are merged. The selected global tolerance worked successfully for all nodes apart from the nodes at the blade root as shown in Fig. 5.14 An overlapped region can be observed for the uncorrected interface, see Fig. 5.14a, where element surfaces are visible between the two fir trees. When the interface is corrected, the element surfaces disappear as shown in Fig. 5.14b. The error was identified quite lately where many computations have already been performed. Nevertheless, it is believed that the error has a small impact on the flutter results since the displacement at the blade root is small and hence, the results are expected to be in quite good agreement compared to the model with a corrected interface. In spite of this prediction, two exemplary reference calculations are performed for a small as well as a low mistuning amplitude to verify this assumption. The results, which can be found in the appendix, show that the differences are quite small and do not compromise the fundings.

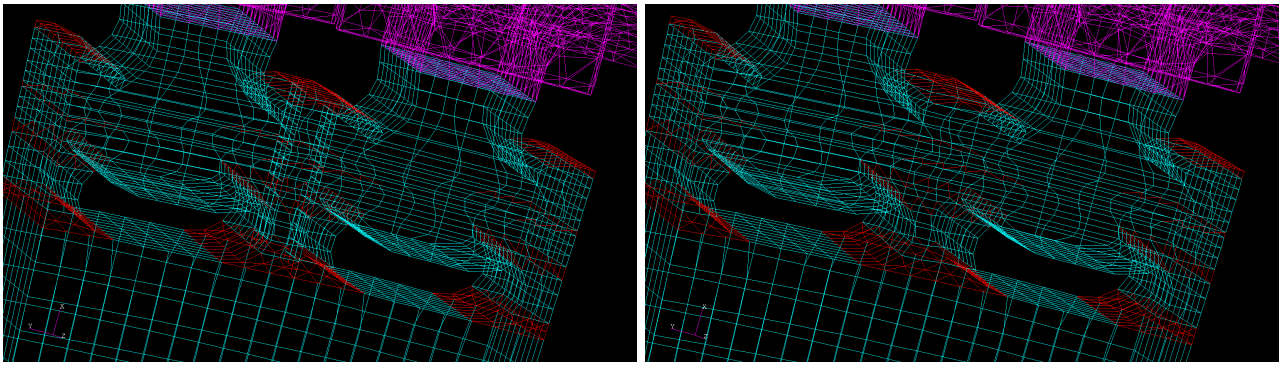

(a) Uncorrected Interface **(b)** Corrected Interface

Figure 5.14: Node Connection Issue at the Blade Root Interface of Structural Two Sector Model

5.5 Update of the Process Chain for the Analysis of Strongly Coupled Bladed Disks

One of the characterization of strongly coupled bladed disks is the occurrence of complex eigenvectors. At the beginning of this thesis, only few suitable pre- and post-processing scripts for the analysis of bladed disks with complex eigenvectors were available at the DLR Institute of Aeroelasticity. Therefore, the existing scripts needed to be updated and new scripts have to be coded in Python. This section describes the update of the process chain for the analysis of strongly coupled bladed disks. Rather than giving details about each individual script, a summary of the main changes is provided.

Firstly, the major points to analyze strongly coupled systems are identified and the procedure to create a two sector model to incorporate alternate mistuning is established. The issues related to alternate mistuning using two sector models as discussed in Sect. 5.3 and 5.4 are tackled and solved.

Also, a script is made to post-process the Nastran output with the aim to extract the complex eigenvalues. To map the eigenvectors on the CFD mesh, one eigenvector has to be present for each individual blade. However, for a two sector structural model, the modal analysis result contains the eigenform of the whole domain, i.e. both blades, so that the result has to be split.

To implement mistuning, the frequencies of each tuned harmonic have to be found first. Then, based on the tuned frequencies, a frequency range, where the mistuned eigenvector is expected, can be specified which is easily possible when the frequencies greatly vary over the harmonics. This is helpful since with the two sector structural model, it is required to recover the second half of the harmonics as mentioned in Sect. 5.4.

Another newly implemented post-processing script enables to identify the real and complex part of the mode shapes. This code is able to transform the Nastran results from the FE method coordinate system to the CFD coordinate system and to construct all standing and traveling wave modes.

Apart from that, several automatization scripts including among others, running Nastran calculations for all harmonics, eigenvector mapping, preparation of TRACE runs are coded, verified and utilized throughout this thesis. In the case of different mistuned structural analysis and many inter-

blade phase angles due to a high number of blades, such an automatization is crucial to avoid a manual setup of each structural and CFD analysis.

Lastly, the Fundamental Mistuning Model is implemented and checked for different cases. With the aid of the FMM, not only an alternate mistuning pattern but also a randomly distributed mistuning can be analyzed.

6 Results

In this chapter, the independence of the steady state CFD flow field for meshes with a different number of elements is presented first. Then, the tuned flutter results for the cantilevered and the shrouded bladed disk are shown utilizing a one sector and a two sectors model. Lastly, the effect of mistuning on the flutter stability is analyzed with the reduced order model FMM and as well as with the CFD solver linearTRACE.

6.1 Mesh Convergence

In order to show the mesh indenpence of the CFD results, the three meshes described in Sect. 5.2.3 are compared against each other using the one sector model. Normally, the mesh independence study has to be performed for the steady as well as for the unsteady computations. However, only the differences between the steady state results are compared in this thesis due to two reasons: Firstly, the unsteady solver linearTRACE is quite sensitive to the steady state solution. When a good converged steady state solution can be achieved, it is assumed that the differences in the unsteady results small. Also, by setting the convergence criteria, i.e. residual values, of the steady and unsteady computations to a low value, a better solution can be guaranteed. Therefore, by selecting a reasonable low convergence criteria and making a relatively good mesh at the beginning, the impact of the grid refinement on the unsteady results is expected to be low providing that a good steady state solution exists. Secondly, to verify the mesh independence of the unsteady computations, N different simulations have to be performed for each mesh. Since the blade number is quite high in the analyzed configuration, the required computational resources rise considerably. Consequently, to save computional time, solely the mesh independence for the steady state solution is studied.

Table 6.1 gives an overview over the three considered meshes with its element number and the required CPU time. The element and the CPU time ratio are always given with respect to the coarse mesh. It can be observed from Tab. 6.1 that the CPU time ratio rises faster than the element ratio. Hence, with more elements in the computational domain, the CPU time may rise noticeably.

To compare the steady state solution, the blade loading in terms of the static pressure on the airfoil surface is shown in Fig. 6.1 at two different span positions. The blade oscillation and in consequence, the aerodynamic work, is larger at a higher span position. For that reason, the differences between the three meshes is of more importance at the higher position, i.e. 80% span here. It can be observed that all three meshes agree quite well among each other apart from a small difference at the trailing edge.

Table 6.1: Mesh Properties for the Three Different Meshes with One Passage used within the Mesh Convergence Study

	# Elements	# Element ratio	CPU time	CPU time ratio
Coarse mesh	574,812	1	15 min	1
Medium mesh	1,659,100	2.89	50 min	3.33
Fine mesh	3,778,144	6.57	139 min	9.27

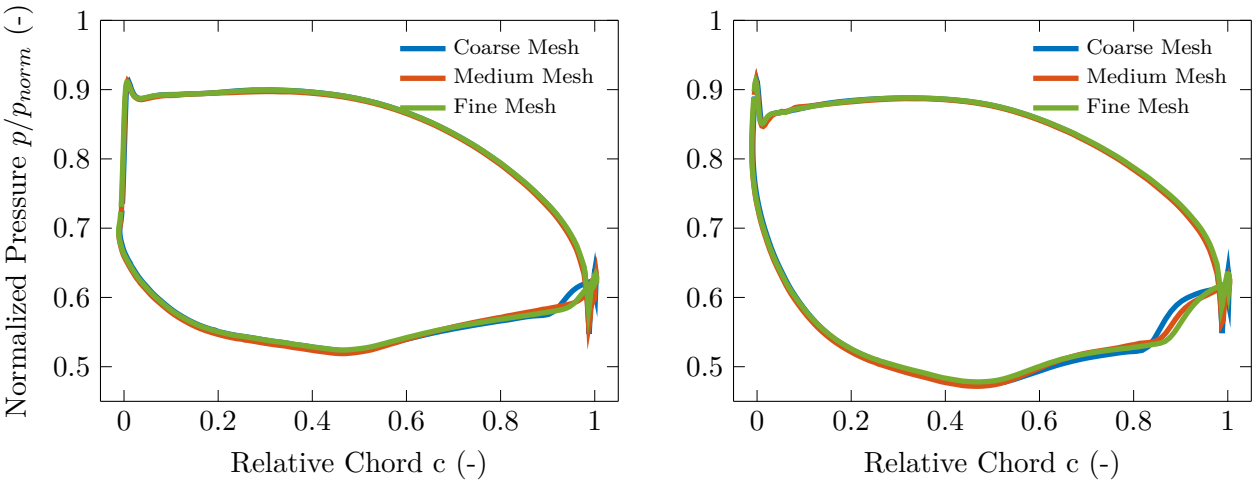

(a) 50% Span **(b)** 80% Span

Figure 6.1: Comparison of the Blade Loading at Two Different Span Positions for the Mesh Convergence Study

The discrepancy is the highest at 80% span, see Fig. 6.1b. Nevertheless, the differences are reasonably small and keeping in mind the large CPU time required for the two finer meshes, it is decided to use the coarse mesh for the proceeding unsteady computations.

6.2 Tuned Flutter Analysis

The aerodynamic damping for all the nodal diameters using the one, two sectors model and the FMM is shown in Fig. 6.2 for the tuned shrouded bladed disk. It can be observed from Fig. 6.2 that some backward TWs are unstable while the most unstable backward TW appears for the -19$^{\text{th}}$ nodal diameter. There is a distinct peak for the most stable mode which occurs for the 9$^{\text{th}}$ nodal diameter. Also, the shape of the damping curve is not smooth around $n = 0$ which might be due to coupling effects. All three models match each other quite well apart from some negligible differences.[1]

[1]What is worth to mention at this point is that the aerodynamic damping of the two sectors model has to be scaled by the factor of two. The reason is that the structural two sectors model has double the mass compared to the one sector model. Both modal analysis results are equaly mass normalized to one causing the amplitude of the eigenvectors of the two sectors model to be smaller by a factor of $1/\sqrt{2}$. This implies in turn that the unsteady pressure is smaller by the factor of $1/\sqrt{2}$ and the aerodynamic work by a factor of $1/2$.

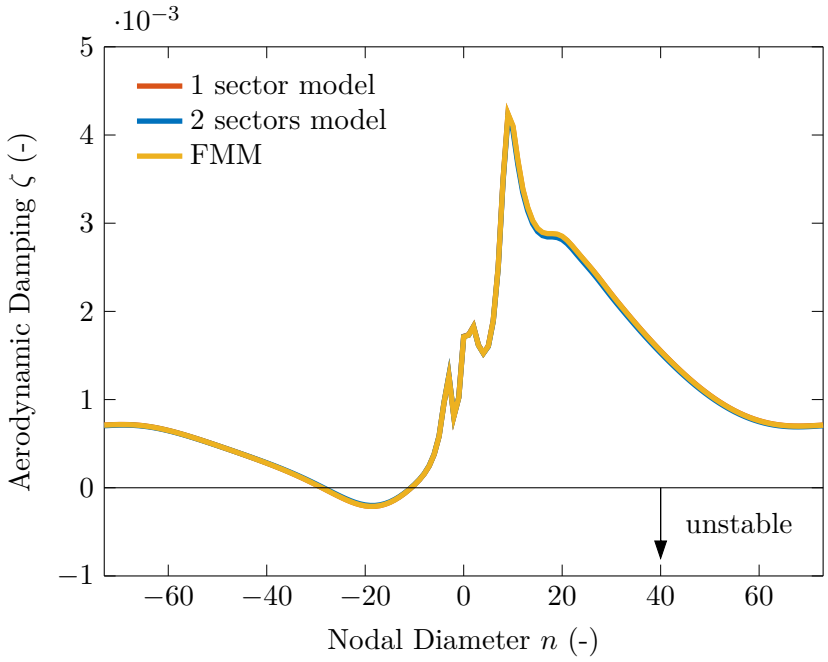

Figure 6.2: Aerodynamic Damping versus Nodal Diameter for the Tuned Shrouded Configuration

The aerodynamic damping versus the nodal diameter utilizing the one, two sectors model and the FMM is shown in Fig. 6.3 for the cantilevered bladed disk. The aerodynamic damping curve has a S-shape which is typical for weakly coupled bladed disks. While most of the backward TWs are unstable, all forward TWs are stable. Both models as well as the ROM predict the most unstable mode for the -29$^{\text{th}}$ nodal diameter. With respect to the shrouded bladed disk, Fig. 6.3, more unstable modes are present and the most unstable mode has a lower aerodynamic damping. In general, the aerodynamic damping for the cantilevered blade is a magnitude higher. Also, the damping peaks of the first positive nodal diameter are still present similar to the shrouded configuration.

There are some outliers in the aerodynamic damping curve at around ± 40 for the two sectors model. The reason for that might be due to acoustic resonance at this specific nodal diameter.[2] However, it is difficult to provide a reliable explanation without conducting more simulations and observing the flow field more in detail. The aerodynamic damping of this outliers is mostly due to numerical issues and can be disregarded. Further inconsistencies in the aerodynamic damping curve can be found at around $+60$ and ± 73 for the two sectors model which might occur due to the same reason as stated above. Apart from that, all three models agree quite well between each other with some minor differences in the range around the most stable and unstable nodal diameter.

In summary, several unstable TW modes occur for the shrouded and the interlocked bladed disk. There are some discrepancies in the damping between the one sector and two sectors model. Never-

[2]When one reference blade oscillates in a given mode shape, it induces a pressure wave which travels towards its neighboring blades. The blades in the vicinity of the reference blade oscillate phase-shifted and in consequence, the neighboring blades reach the same amplitude as the reference blade shifted in time. So, when the traveling time of the pressure wave equals the inter-blade phase angle, the pressure wave impinges at the leading or trailing edge of the neighboring blade and amplifies the oscillation resulting in a change in aerodynamic work and damping.

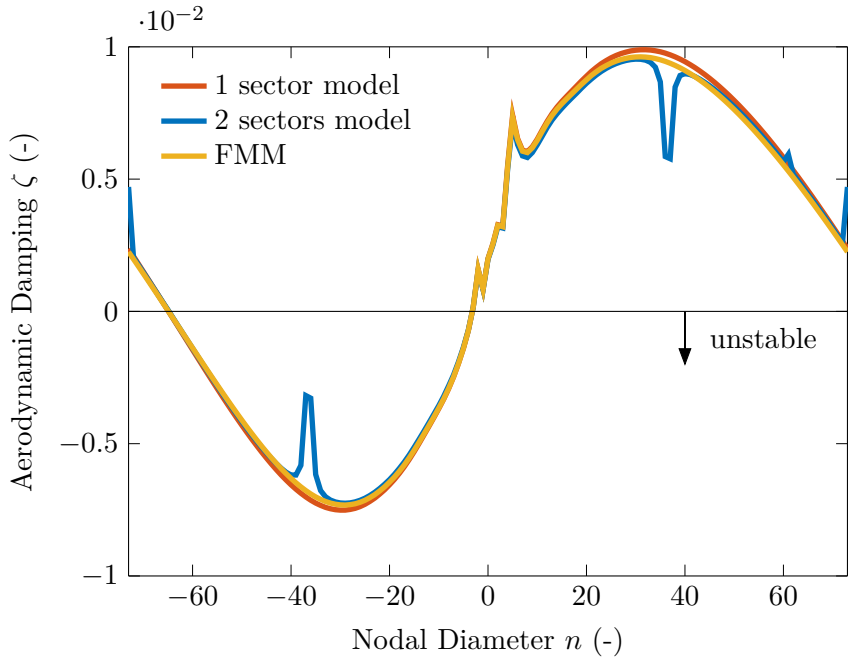

Figure 6.3: Aerodynamic Damping versus Nodal Diameter for the Tuned Cantilevered Configuration

theless, to account for mistuning, the two sectors model is preferred and all further mistuned flutter results are obtained by this method. Based on the tuned damping curves, potential outliers should be kept in mind when discussing the mistuned results.

6.3 Mistuned Flutter Analysis

An alternate mistuning amplitude up to 15% is implemented and analyzed with linearTRACE. Since the output of the FMM is random, i.e. equivalent mistuned nodal diameters and the corresponding dampings are distributed randomly, only the most unstable mode is compared against the linearTRACE solution.

The aerodynamic damping for several mistuning amplitudes together with the tuned damping is shown in Fig. 6.4 for the shrouded bladed disk. What is striking at first glance is the minor effect of mistuning upon the damping. Even with a high mistuning amplitude of $\Delta\omega_{mis} = 15\%$, the damping curve remains almost unchanged. Some local peaks apear in the curve for $n_{eq} = \pm 37$ and $n_{eq} = \pm 67$ which get more pronounced with increasing mistuning amplitude. None of the introduced alternate mistunings is able to stabilize the system with shroud interlocks.

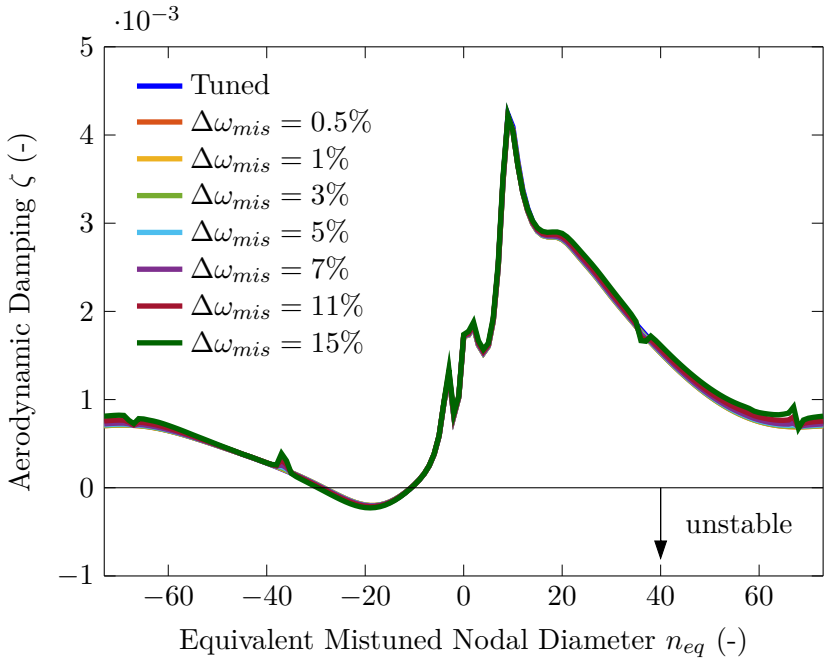

Figure 6.4: Aerodynamic Damping versus Equivalent Mistuned Nodal Diameter for the Mistuned Shrouded Configuration

To show the appearing local peaks, Fig. 6.5 provides a zoom to the negative nodal diameter range.

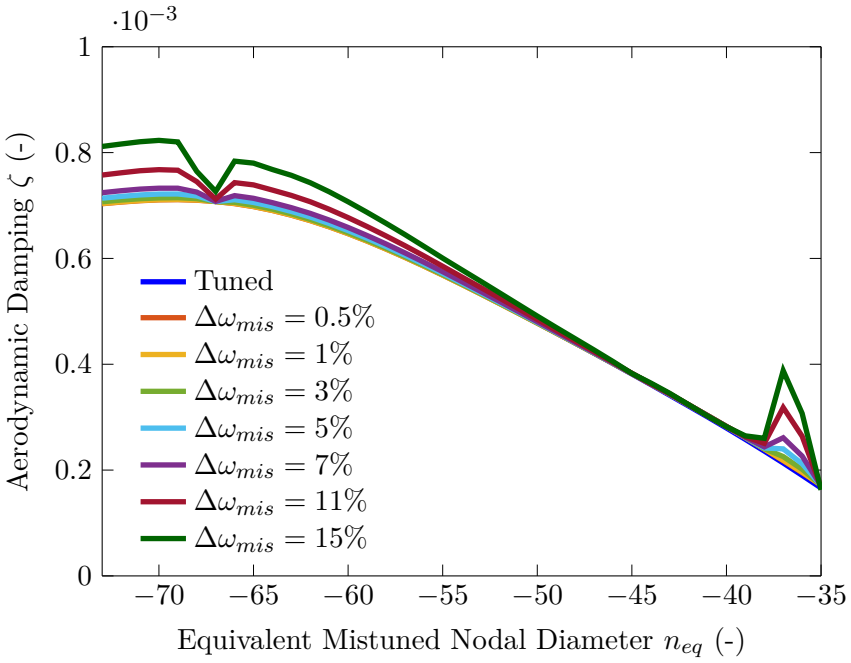

Figure 6.5: Zoom to the Aerodynamic Damping in the Range of Interest for the Mistuned Shrouded Configuration

While most of the damping changes smoothly with the equivalent mistuned nodal diameter, some

abrupt decrease or increase in damping appears at these local peaks. The reason for the occurance of the peaks is difficult to determine and has to be analyzed in further studies. Also, what is visible from Fig. 6.5 is the fact that mistuning increases the aerodynamic damping of stable modes.

The absolute difference between the mistuned damping ζ_{mis} and the tuned damping ζ^0 is depicted in Fig. 6.6. A value greater than zero means that mistuning stabilizes the system at a particular equivalent mistuned nodal diameter and a negative value implies a destabilization. There is no distinct

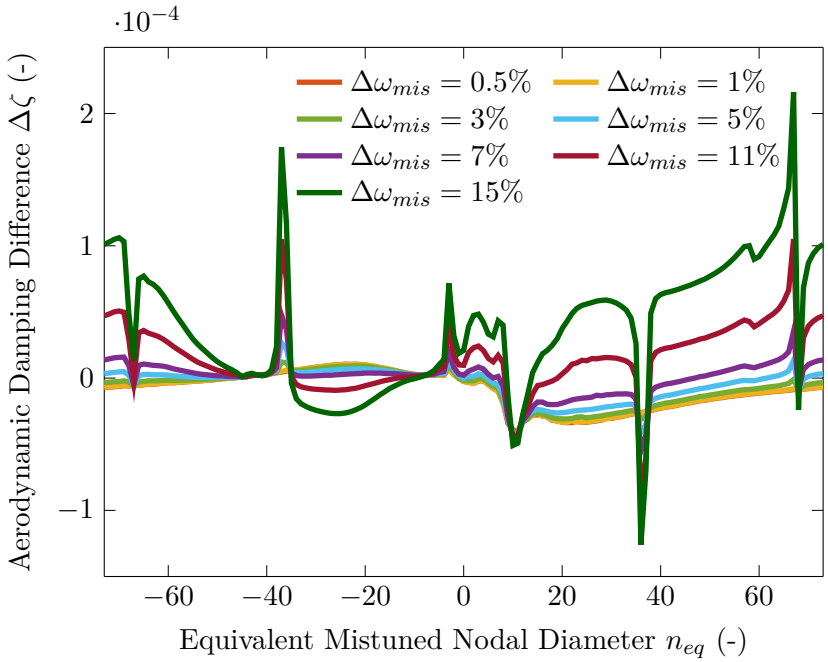

Figure 6.6: Difference in Aerodynamic Damping $\Delta\zeta = \zeta_{mis} - \zeta^0$ versus Equivalent Mistuned Nodal Diameter for Different Levels of Mistuning of the Shrouded Bladed Disk

pattern which n_{eq} gets more stable, however, some interesting remarks can still be made. Up to a mistuning amplitude of $\Delta\omega_{mis} = 5\%$, the majority of n_{eq} are destabilized but little difference between the mistuned and tuned system is noticeable. When the mistuning is increased further, the impact of mistuning on the system changes and many of the positive equivalent mistuned nodal diameters and some of the negative ones experience a stabilizing effect. The local peaks detected in Fig. 6.4 or Fig. 6.5 have direct repercussions on the damping. Looking at the most unstable tuned mode $n_{eq} = -19$, a decrease in damping can be quantified.

A system is unstable if one of the modes has an unfavorable damping. With this in mind, it is desired to visualize the most unstable mode with respect to the mistuning amplitude which is done in Fig. 6.7. The most unstable mode remains unchanged with mistuning and always appears at $n_{eq} = -19$. The aerodynamic damping calculated with the Fundamental Mistuning Model using tuned aerodynamic influence coefficients is also added. What is quite surprising is that the aerodynamic damping of the most unstable mode decreases with the mistuning amplitude. This is remarkable since the normal expectation is an increase in mistuning. The behavior is addressed and discussed further in Chap. 7. The FMM predicts the opposite where the minimum aerodynamic damping continuously

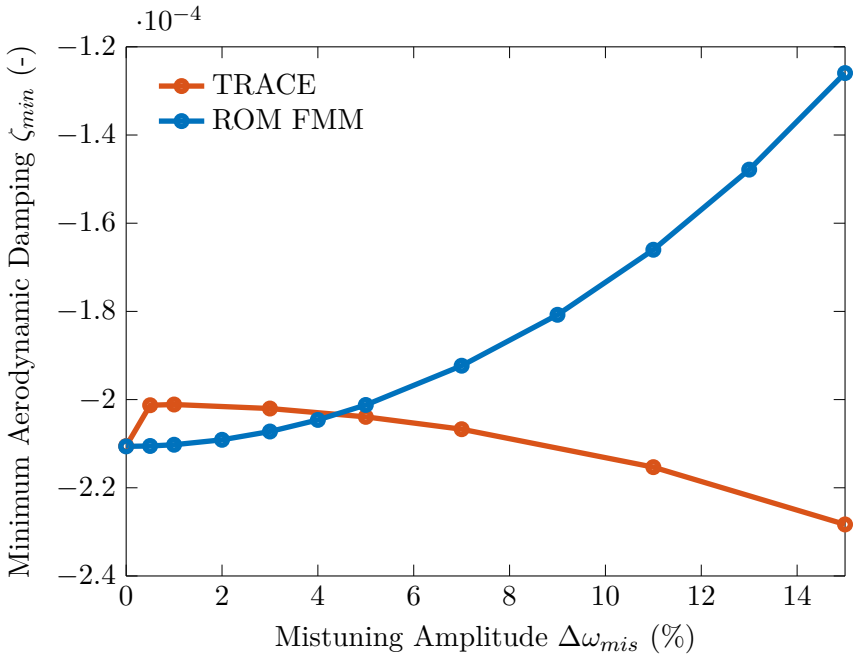

Figure 6.7: Minimum Aerodynamic Damping Calculated Using TRACE and FMM for the Shrouded Configuration

increases with mistuning. Therefore, the ROM completely fails to capture the behavior of the system in theT presence of mistuning, even for small mistuning amplitudes.

The aerodynamic damping of the cantilevered bladed disk for several levels of mistuning together with the tuned damping can be seen in Fig. 6.8. It can be observed that the damping greatly changes even for a small mistuning amplitude of $\Delta\omega_{mis} = 0.2\%$. While a small fraction of the modes is still unstable for $\Delta\omega_{mis} = 0.4\%$, the system gets completely stabilized for $\Delta\omega_{mis} = 3.5\%$. The aerodynamic damping converges towards the tuned average value with increasing mistuning as has been detected in several publications. In this case, a similar trend establishes but the converging trend appears to happen much more moderately. What is surprising here is that some unstable modes experience a higher damping than the tuned mean. Two reasons can be provided for this trend. Firstly, the attribution of each mistuned mode to a specific equivalent mistuned nodal diameter is difficult for the cantilevered blade because the structural frequencies are clustered together. In consequence, some modes could be incorrectly assigned to n_{eq} so that the modes with a higher damping compared to the tuned mean would actually correspond to a stable tuned nodal diameter instead to an unstable mode which occurs for instance for $n_{eq} = -50$. Secondly, the converging behavior published in the literature is mostly demonstrated by a reduced order model and not by a higher order compuations as it is done here. Hence, the herein presented result could be either seen as an exception or as a basis for further studies to reverify whether the converging trend holds for every possible case of a bladed disk.

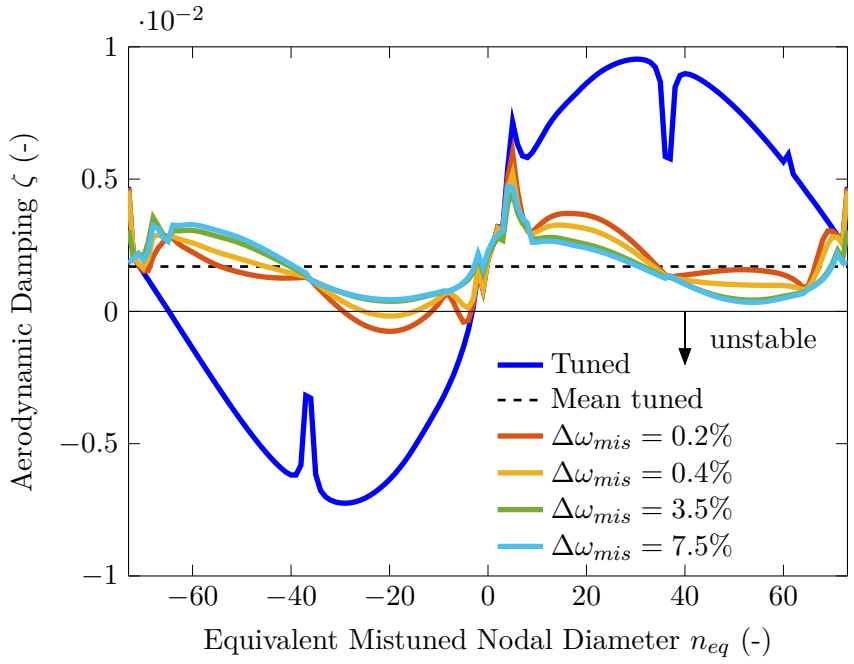

Figure 6.8: Aerodynamic Damping versus Equivalent Mistuned Nodal Diameter for the Mistuned Cantilevered Configuration

Similar to the shrouded bladed disk, Fig. 6.9 depicts the minimum aerodynamic damping as a function of the mistuning amplitude $\Delta\omega_{mis}$. FMM as well as linearTRACE predict a stabilizing effect

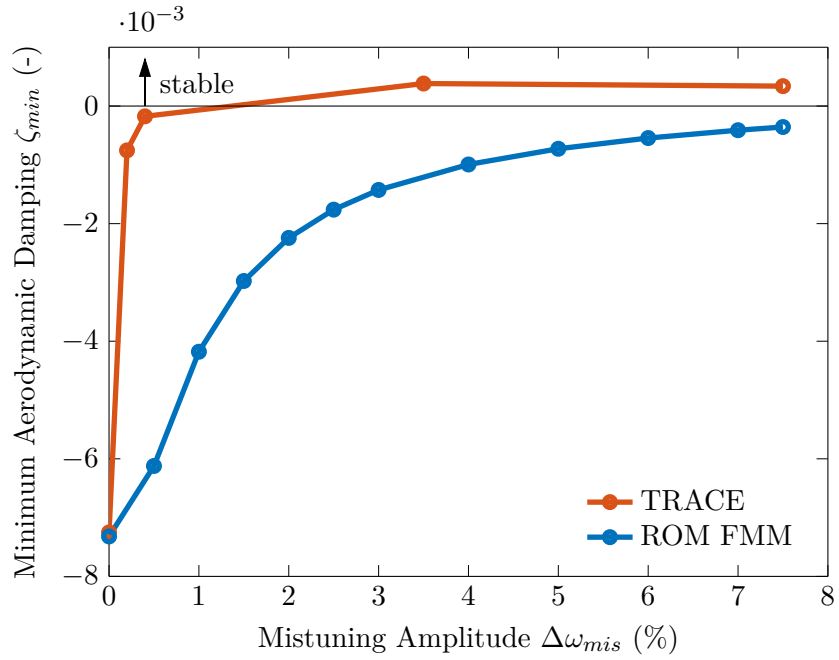

Figure 6.9: Minimum Aerodynamic Damping Calculated Using TRACE and FMM for the Cantilevered Configuration

with increasing mistuning amplitude. However, the increase in damping appears more rapidly for linearTRACE compared to the ROM. A saturation regarding stability can be observed which is qualitatively similar for both methods. After a certain mistuning amplitude, the stabilizing effect of mistuning decreases and only a small increase in damping can be detected. While the saturation effect establishes for linearTRACE already around $\Delta\omega_{mis} = 3.5\%$, it is shifted to a higher mistuning level for the ROM which occurs at about $\Delta\omega_{mis} \approx 4\%$. In addition, a small decrease in damping is observed for the linearTRACE results between the mistuning amplitudes of $\Delta\omega_{mis} = 3.5\%$ and $\Delta\omega_{mis} = 7.5\%$.

7 Discussion of Results

This chapter discusses the previous results more thoroughly and tries to give answers to specific questions, such as why does the aerodynamic damping decrease with the mistuning amplitude for the shrouded bladed disk or for the cantilevered case, where does the difference in the minimum aerodynamic damping between linearTRACE and the FMM come from? The first part of the discussion is done from a structural point of view whereas the second part focuses on the observations from the CFD computations.

7.1 Structural Considerations

The modal assurance criterion (MAC) gives the linearity independence of two eigenvectors or in other words, the similarity between two modes. A value of one indicates that eigenvectors are completely the same and a value of zero results from two orthogonal eigenforms. Using mass normalized eigenforms, the MAC factor is defined by

$$\mathrm{MAC} = \frac{\left(\vec{\Psi}^H\,\vec{\Psi}_{mis}\right)^H\left(\vec{\Psi}^H\,\vec{\Psi}_{mis}\right)}{\left(\vec{\Psi}^H\,\vec{\Psi}\right)\left(\vec{\Psi}_{mis}^H\,\vec{\Psi}_{mis}\right)}. \tag{7.1}$$

The eigenforms in Eq. (7.1) are arranged according to

$$\vec{\Psi} = \left(\vec{\Psi}_0, \vec{\Psi}_0 e^{j\,\gamma}, \vec{\Psi}_0 e^{2j\,\gamma}, ..., \vec{\Psi}_0 e^{h_{FEM}j\,\gamma}\right)^T \tag{7.2}$$

with γ being the inter-sector phase angle while $\vec{\Psi}_0$ is the eigenform of the 0^{th} blade or reference domain which consists of all real and imaginary displacements as follows

$$\vec{\Psi}_0 = \left(\Re(\vec{\Psi}_{0,x}),\, \Re(\vec{\Psi}_{0,y}),\, \Re(\vec{\Psi}_{0,z}),\, \Im(\vec{\Psi}_{0,x}),\, \Im(\vec{\Psi}_{0,y}),\, \Im(\vec{\Psi}_{0,z})\right)^T. \tag{7.3}$$

Equation (7.2) is expressed in a general form, i.e. the computational domain consists of several blades with an inter-sector phase angle as the phase-difference at the boundaries. When only one sector is considered, γ can be replaced by the inter-blade phase angle and h_{FEM} by $(N-1)$. In the present case, the vector $\vec{\Psi}$ consists of all the degrees of freedom of the two sectors model and of the nodes which are mapped on the CFD mesh.

To verify the implemented script for the calculation of the MAC factor and to also visualize a tuned system, Fig. 7.1 illustrates the MAC factors for the tuned shrouded configuration. It can be concluded

from Fig. 7.1 that the MAC factor of the tuned system is an identity matrix. Forward TW modes are in the range $0 \leq h_{FEM} \leq N/2$ and backward TW modes in the range $N/2 \leq h_{FEM} \leq N-1$. All values outside the diagonal are zero due to the orthogonality property of eigenvectors.

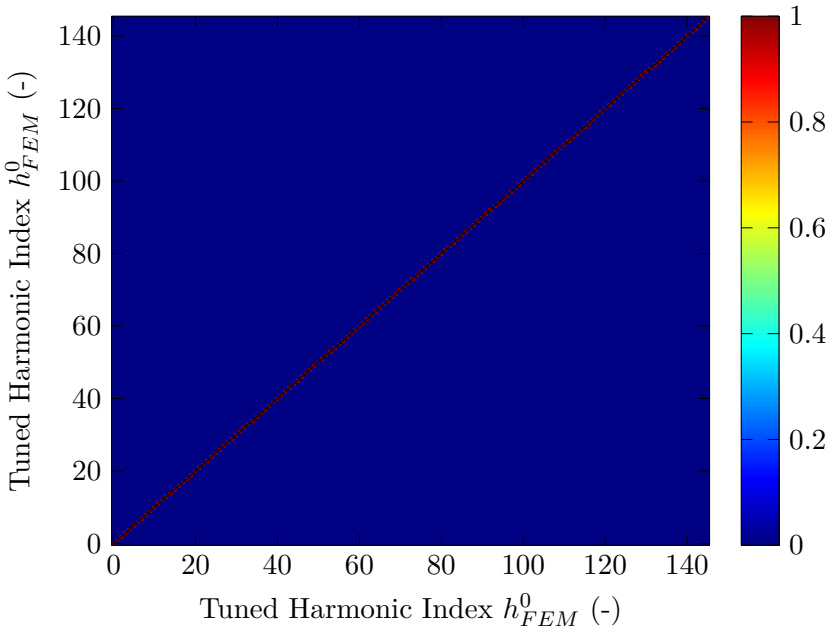

Figure 7.1: Verification of the MAC Factor for the Tuned System of the Shrouded Bladed Disk

The MAC factor is presented for a low and a high mistuning amplitude to see both extrema. It should be noted that the scale of every plot is not identical and attention has to be paid when comparing the plots.

Figure 7.2 shows the MAC factors for a mistuning amplitude of $\Delta\omega_{mis} = 0.5\%$ for the lower scale range, i.e. magnitude of 10^{-4}. When a higher scale is selected, no differences would be visible apart from an identity matrix. It can be observed that that no coupling between forward and backward TW modes takes place. A mistuned forward TW h_{FEM} mode shows a similarity to the tuned mode h^0_{FEM} as well as to the tuned mode $h^0_{FEM} = N/2 - h_{FEM}$ for the given case. This is not surprising due to the fact that a two sectors structural model is used for the modal analysis. Behind every computational domain consisting of two sectors, a cyclic symmetry is recovered in the case of alternate mistuning. In consequence, the amplitude of the mass normalized eigenvector of every two sectors is the same but phase-shifted by the inter-sector phase angle. The orthogonality principle holds true for each two sectors domain but it does not apply within the two sectors domain itself where the mode of each of the two sectors can be linearly dependent since the tuned inter-blade phase angle is not present anymore due to mistuning. As a result, only modes calculated with the same harmonic index can be linearly dependent.

Similarly, the mistuned backward mode h_{FEM} is coupled to a tuned mode with the same harmonic index h^0_{FEM} and to the tuned mode $h^0_{FEM} = \frac{3}{2}N - h_{FEM}$. In fact, mistuned forward and backward modes have the same MAC factors which is expressed through a point symmetry around the higher

standing wave index, i.e. $h_{FEM} = N/2 = 73$, in Fig. 7.2.

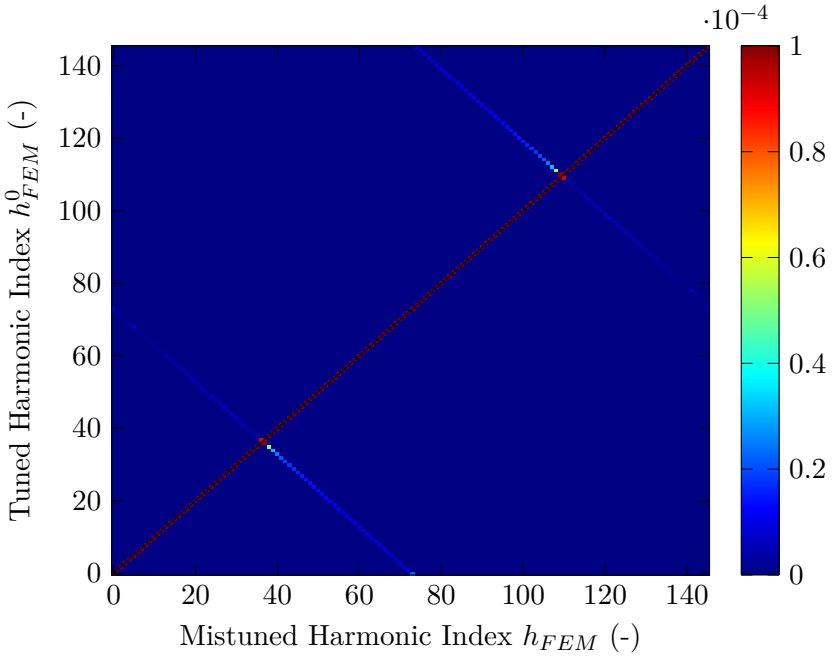

Figure 7.2: MAC Factor for an Alternate Mistuning Amplitude of $\Delta\omega_{mis} = 0.5\%$ for the Shrouded Configuration, Lower Scale Range

The MAC factor for the same configuration as in Fig. 7.2 but with an increased mistuning amplitude from 0.5 to 15% is plotted in Fig. 7.3 in the lower range scale.Apart from the increased linear dependency, it can be also noticed that the order of magnitude rises from 10^{-4} to 10^{-2}. For the same mistuning amplitude of $\Delta\omega_{mis} = 15\%$ the upper scale range, i.e. from 0.95 to 1, is shown in Fig. 7.4. Some markers along the diagonal become blue but this does not mean that the modes are independent but simply that the MAC factor of this modes gets below 0.95. Apart from that, what can be noticed is the deviation of the modes with a higher mistuned harmonic index from the tuned modes while the lower mistuned modes are still quite similar. This leads to the conclusion that the effect of mistuning on the higher modes is greater compared to the lower modes. In return, regarding the aerodynamic damping, the lower negative traveling wave modes are unstable for the shrouded case and the mistuning is not able to alter them sufficiently enough to have an impact on the aerodynamics. The low alternation of the mode shapes due to mistuning and the greater effect on the higher modes might be one of the explanations why mistuning is not able to efficiently stabilize the lower modes of the shrouded system.

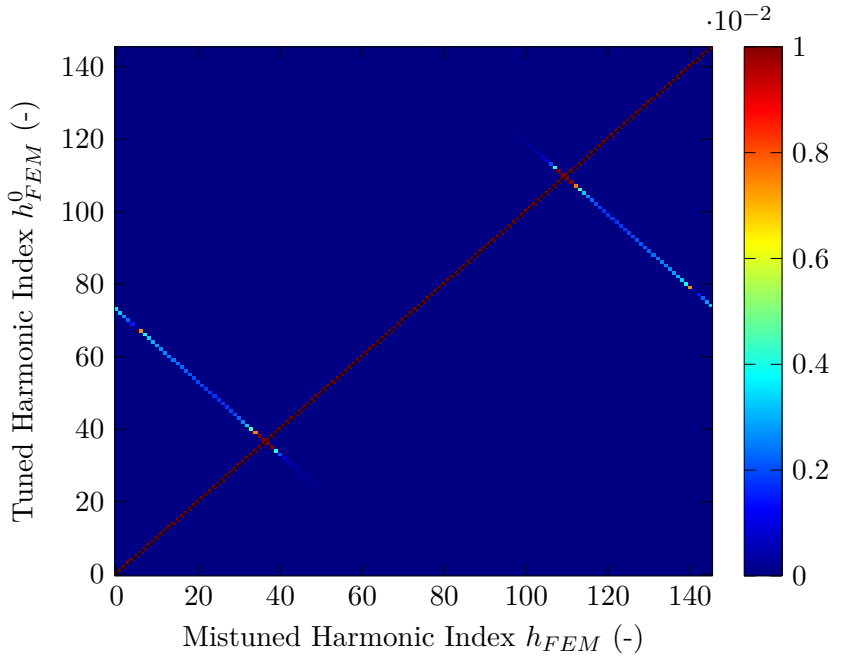

Figure 7.3: MAC Factor for an Alternate Mistuning Amplitude of $\Delta\omega_{mis} = 15\%$ for the Shrouded Configuration, Lower Scale Range

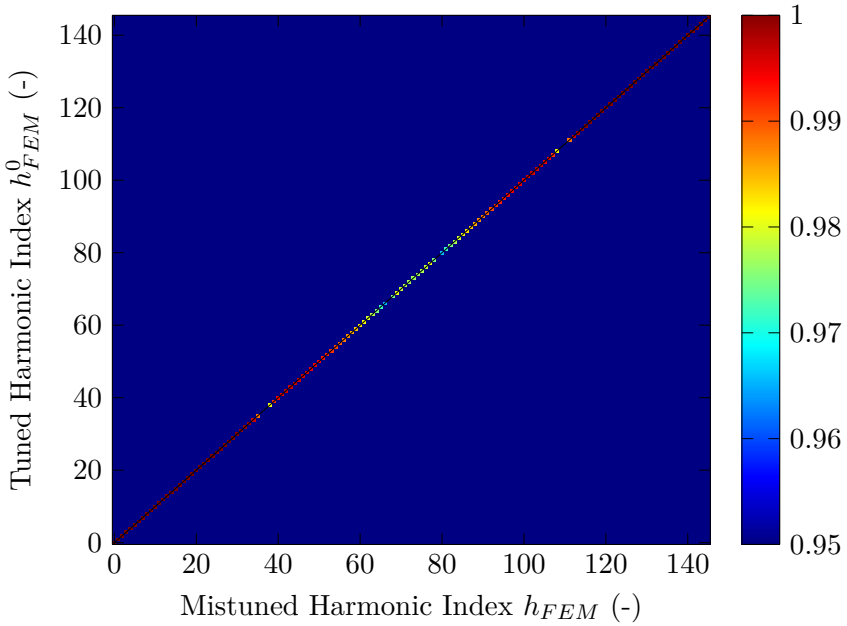

Figure 7.4: MAC Factor for an Alternate Mistuning Amplitude of $\Delta\omega_{mis} = 15\%$ for the Shrouded Configuration, Upper Scale Range

The MAC factor for the cantilevered bladed disk is shown for a mistuning amplitude of 0.4% and 7.5% in the Fig. 7.5 and 7.6 respectively. Similar to the shrouded configuration, there is no coupling between forward and backward TW modes and the deviation along the main diagonal (from

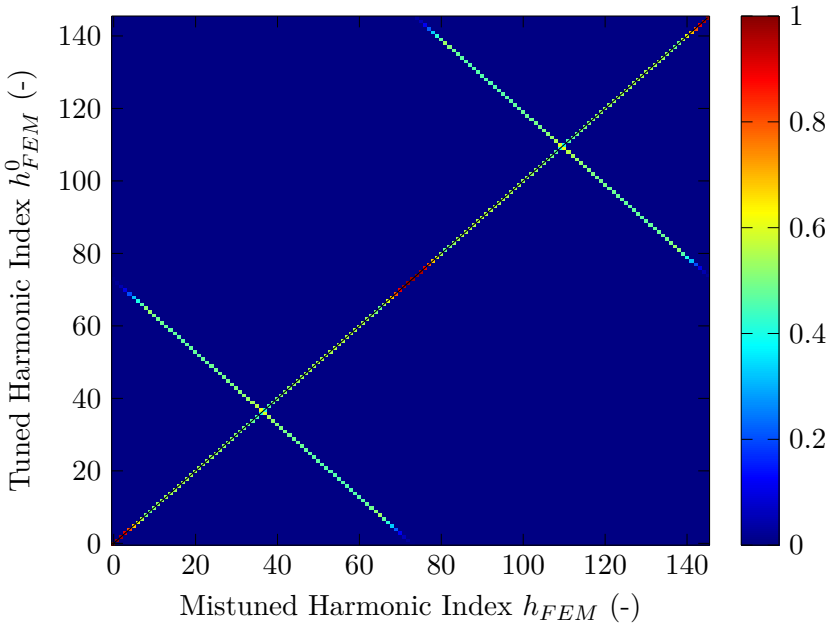

Figure 7.5: MAC Factor for an Alternate Mistuning Amplitude of $\Delta\omega_{mis} = 0.4\%$ for the Cantilevered Configuration

left bottom to top right) increases with increasing mistuning. On the other hand, one of the main differences is the magnitude of the MAC factor variation. This implies that when no contact at the interlock interface is present, i.e. there is no cyclic symmetry boundary condition from the numerical perspective, the coupling or effect of mistuning on the modes is more pronounced. An explanation for this might be the wide variation of the structural frequency for the shrouded case. Due to the use of a two sectors model and alternate mistuning, the lower modes can only couple the higher modes which have a considerably higher frequency. On the contrary, the variation of the structural frequency is much less for the cantilevered bladed disk so that the coupling can take place more easily. The larger change in the eigenform might result in a considerable change of the aerodynamic behavior and hence, a greater effect on the stability curve compared to the shrouded bladed disk.

At this point, an attempt is made to explain the decrease in aerodynamic damping with increasing mistuning amplitude predicted by linearTRACE. Based on the assumption that the mistuned aerodynamic damping can be combined in the same manner as the related modes, this brings up the question whether the damping of the mistuned system can be smaller if both modes are substracted instead of added. In case of alternate mistuning, a mistuned mode is composed of two tuned modes and the mistuned eigenform can be linearly expressed as a sum or difference of these two modes by

$$\vec{\Psi}_{mis} = \alpha\vec{\Psi}_{\alpha} \pm \beta\vec{\Psi}_{\beta} \tag{7.4}$$

where α and β are scaling factors related to the tuned modes $\vec{\Psi}_{\alpha}$ and $\vec{\Psi}_{\beta}$ respectively and are directly proportional to the MAC factor as it is shown in Eq. (7.6). In a linear aeroelastic solver, the aerodynamic work is linearly dependent on the eigenvector and hence, the mistuned aerodynamic damping

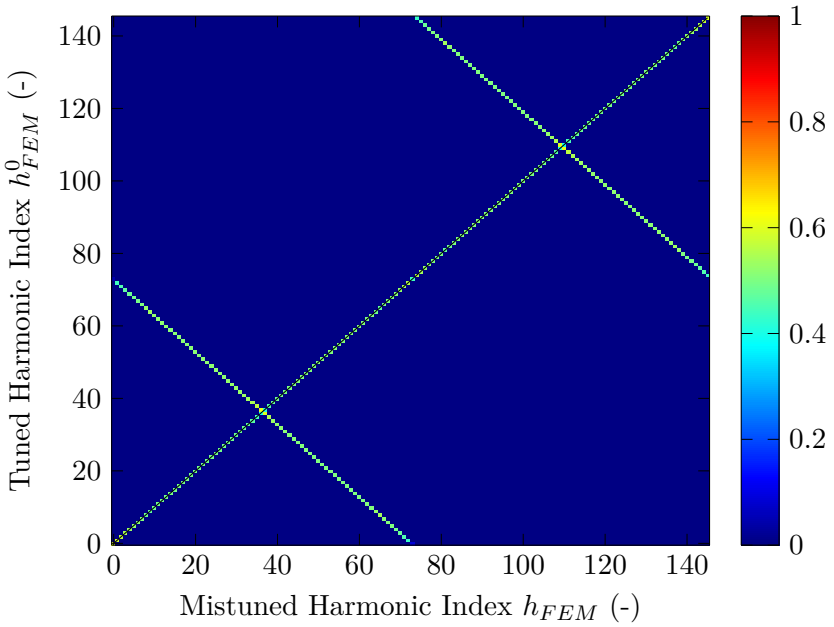

Figure 7.6: MAC Factor for an Alternate Mistuning Amplitude of $\Delta\omega_{mis} = 7.5\%$ for the Cantilevered Configuration

can be expressed with the same scaling factors as in Eq. (7.4) through

$$\zeta_{mis} \overset{?}{\propto} \alpha\zeta_\alpha \pm \beta\zeta_\beta \,. \tag{7.5}$$

The question arises whether the distinction between an addition and subtraction in Eq. (7.4) is reflected in Eq. (7.5). If the two MAC factors are independent of the sign of Eq. (7.4), it means that the mistuned eigenvector would also be independent of the sign. However, the mistuned aerodynamic damping in Eq. (7.5) is linearly proportional to the mistuned mode and one can conclude that the sign is not reflected in Eq. (7.5). In consequence, it means that the mistuned aerodynamic damping might be the difference of the tuned damping and therefore, a decrease in damping is thinkable. However, the above consideration does not represent a physical effect but clarifies if a conclusion from the distribution of the MAC factor on the damping is possible and might only serve as an explanation for the decrease in damping from a numerical point of view.

Multiplying Eq. (7.4) with $\vec{\Psi}_\alpha^H$ and considering the addition gives

$$\begin{aligned} \vec{\Psi}_\alpha^H \vec{\Psi}_{mis} &= \alpha \vec{\Psi}_\alpha^H \vec{\Psi}_\alpha + \underbrace{\beta \vec{\Psi}_\alpha^H \vec{\Psi}_\beta}_{=0} \\ \frac{\left(\vec{\Psi}_\alpha^H \vec{\Psi}_{mis}\right)^H \left(\vec{\Psi}_\alpha^H \vec{\Psi}_{mis}\right)}{\left(\vec{\Psi}_\alpha^H \vec{\Psi}_\alpha\right)\left(\vec{\Psi}_{mis}^H \vec{\Psi}_{mis}\right)} &= \alpha \frac{\left(\vec{\Psi}_\alpha^H \vec{\Psi}_{mis}\right)^H \left(\vec{\Psi}_\alpha^H \vec{\Psi}_\alpha\right)}{\left(\vec{\Psi}_\alpha^H \vec{\Psi}_\alpha\right)\left(\vec{\Psi}_{mis}^H \vec{\Psi}_{mis}\right)} = \mathrm{MAC}_{\alpha+} \end{aligned} \tag{7.6}$$

where $\beta \vec{\Psi}_\alpha^H \vec{\Psi}_\beta$ is zero due to orthogonality. As can be seen from the left hand side of Eq. (7.6), it is

exactly the MAC factor as specified in Eq. (7.1) and α is proportional to $\mathrm{MAC}_{\alpha+}$. Inserting Eq. (7.4) into Eq. (7.6) results in

$$\begin{aligned}\mathrm{MAC}_{\alpha+} &= \alpha \frac{\left[\vec{\Psi}_\alpha^H\left(\alpha\vec{\Psi}_\alpha + \beta\vec{\Psi}_\beta\right)\right]^H\left(\vec{\Psi}_\alpha^H\vec{\Psi}_\alpha\right)}{\left(\vec{\Psi}_\alpha^H\vec{\Psi}_\alpha\right)\left[\left(\alpha\vec{\Psi}_\alpha + \beta\vec{\Psi}_\beta\right)^H\left(\alpha\vec{\Psi}_\alpha + \beta\vec{\Psi}_\beta\right)\right]} \\ &= \alpha^2 \frac{\left(\vec{\Psi}_\alpha^H\vec{\Psi}_\alpha\right)^2}{\alpha^2\left(\vec{\Psi}_\alpha^H\vec{\Psi}_\alpha\right)^2 + \beta^2\left(\vec{\Psi}_\alpha^H\vec{\Psi}_\alpha\right)\left(\vec{\Psi}_\beta^H\vec{\Psi}_\beta\right)}\end{aligned} \tag{7.7}$$

and by substituting $\left(\vec{\Psi}_\alpha^H\vec{\Psi}_\alpha\right) = A$ and $\left(\vec{\Psi}_\beta^H\vec{\Psi}_\beta\right) = B$ in

$$\mathrm{MAC}_{\alpha+} = \alpha^2\frac{A^2}{\alpha^2A^2 + \beta^2AB} = \alpha^2\frac{A}{\alpha^2A + \beta^2B}\,. \tag{7.8}$$

The same procedure can be applied for a multiplication with $\vec{\Psi}_\beta^H$ which gives

$$\mathrm{MAC}_{\beta+} = \beta^2\frac{B^2}{\beta^2B^2 + \alpha^2AB} = \beta^2\frac{B}{\beta^2B + \alpha^2A}\,. \tag{7.9}$$

Now the subtraction in Eq. (7.4) is considered. While $\mathrm{MAC}_{\alpha-}$ is unchanged, i.e. $\mathrm{MAC}_{\alpha+} = \mathrm{MAC}_{\alpha-}$, premultiplying with $\vec{\Psi}_\beta^H$ gives

$$\begin{aligned}\mathrm{MAC}_{\beta-} &= -\beta \frac{\left[\vec{\Psi}_\beta^H\left(\alpha\vec{\Psi}_\alpha - \beta\vec{\Psi}_\beta\right)\right]^H\left(\vec{\Psi}_\beta^H\vec{\Psi}_\beta\right)}{\left(\vec{\Psi}_\beta^H\vec{\Psi}_\beta\right)\left[\left(\alpha\vec{\Psi}_\alpha - \beta\vec{\Psi}_\beta\right)^H\left(\alpha\vec{\Psi}_\alpha - \beta\vec{\Psi}_\beta\right)\right]} \\ &= \beta^2 \frac{\left(\vec{\Psi}_\beta^H\vec{\Psi}_\beta\right)^2}{\beta^2\left(\vec{\Psi}_\beta^H\vec{\Psi}_\beta\right)^2 + \alpha^2\left(\vec{\Psi}_\alpha^H\vec{\Psi}_\alpha\right)\left(\vec{\Psi}_\beta^H\vec{\Psi}_\beta\right)} \\ &= \beta^2\frac{B}{\beta^2B + \alpha^2A}\,.\end{aligned} \tag{7.10}$$

By comparing Eq. (7.10) to Eq. (7.9), it can be concluded that the MAC factor is independent of the sign of the two composed vectors. In consequence, it is impossible to distinguish if the two parts are added or substracted and hence, the mistuned damping ζ_{mis} in Eq. (7.5) might get more unstable. On the other hand, if $\vec{\Psi}_{mis}$ would be dependent on the sign, i.e. $\mathrm{MAC}_{\beta+} \neq \mathrm{MAC}_{\beta-}$, the damping could be estimated by calculating α and β with the aid of the MAC factors.

Also, a relation between $\mathrm{MAC}_{\alpha+}$ and $\mathrm{MAC}_{\beta+}$ can be established by adding Eq. (7.8) to Eq. (7.9)

$$\begin{aligned} \mathrm{MAC}_{\alpha+} + \mathrm{MAC}_{\beta+} &= \alpha^2 \frac{A}{\alpha^2 A + \beta^2 B} + \beta^2 \frac{B}{\beta^2 B + \alpha^2 A} = 1 \\ \mathrm{MAC}_{\alpha+} &= 1 - \mathrm{MAC}_{\beta+} \,. \end{aligned} \tag{7.11}$$

From Eq. (7.11) it can be concluded that the sum of the MAC factors always has to be one whereas the sum of α and β is unequal to one.

7.2 Effect of Mistuning on the Aerodynamic Influence Coefficients

To investigate the background of the results more in detail, the aerodynamic influence coefficients which are representative for the aerodynamic work are analyzed in traveling wave space. The aerodynamic influence coefficients for the shrouded configuration are shown in Fig. 7.7 where the solid and the dashed line is the real and imaginary of the AICs respectively. The vertical black lines show the range in which the tuned system is unstable. The mistuning does not alter the aerodynamics almost at all apart from some local peaks which might be due to numerical reasons. The minor effect on the aerodynamics is due to the fact that the tuned mode perturbation is almost negligible as shown using the MAC factors.

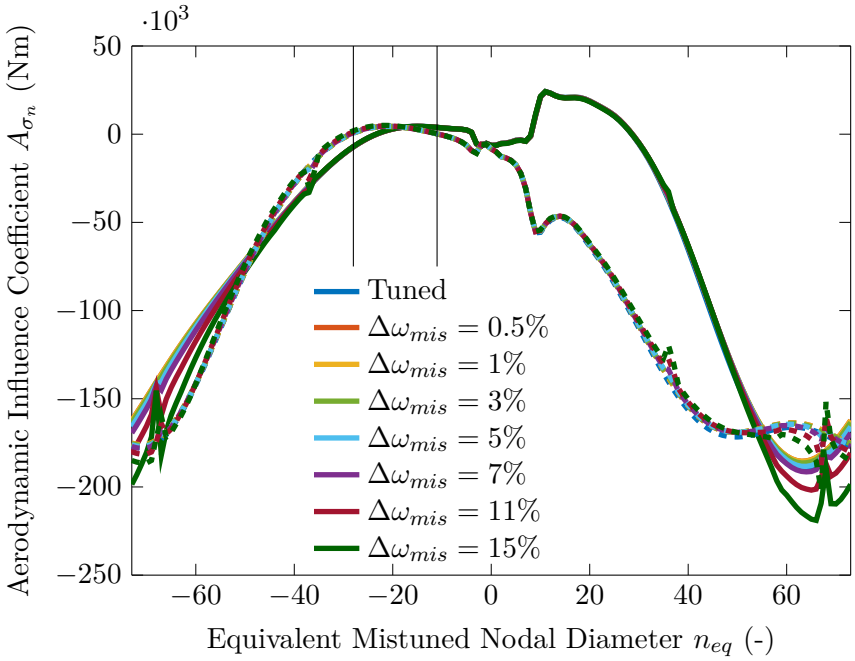

Figure 7.7: Aerodynamic Influence Coefficients in Traveling Wave Space versus Equivalent Mistuned Nodal Diameter for Different Alternate Mistuning Amplitudes of the Shrouded Configuration; Solid Line: Real Part, Dashed Line: Imaginary Part

The AICs in traveling wave space can be seen in Fig. 7.8 for the cantilevered configuration. Once again, the vertical black lines define the region where the tuned system is unstable. Compared

to the shrouded case, the aerodynamics of the cantilevered bladed disk change significantly with the mistuning. The curve of the tuned AICs has a harmonic shape similar to the S-shape of the aerodynamic damping plot. With increasing mistuning, the curve for the real as well as imaginary part of AICs flattens and is almost constant over the equivalent mistuned nodal diameter for a mistuning amplitude of $\Delta\omega = 7.5\%$. In physical space, this would mean that aerodynamic forces in a cascade are independent of the inter-sector phase angle. Since the aerodynamic work is directly connected to the damping, the

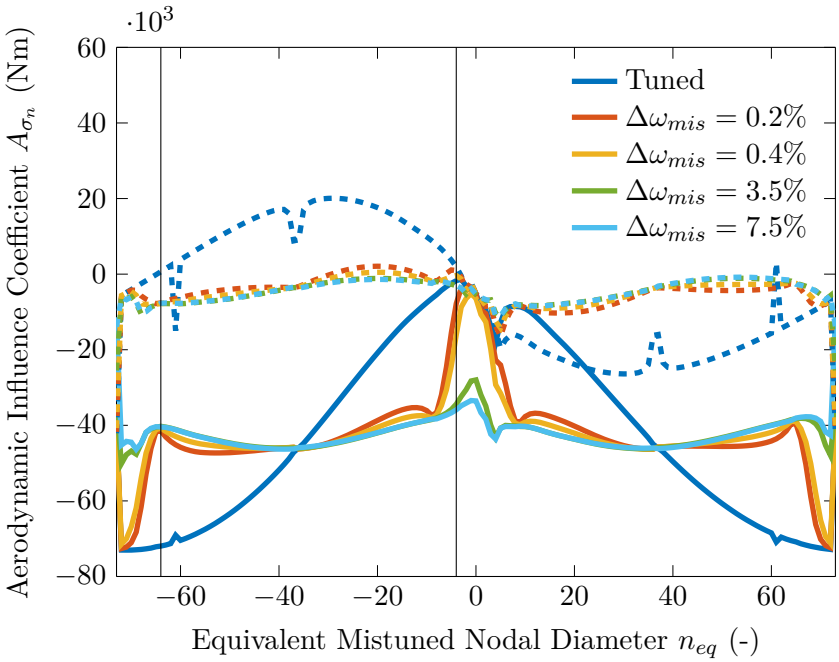

Figure 7.8: Aerodynamic Influence Coefficients in Traveling Wave Space versus Equivalent Mistuned Nodal Diameter for Different Alternate Mistuning Amplitudes of the Cantilevered Configuration; Solid Line: Real Part, Dashed Line: Imaginary Part

converging behavior towards the tuned value with increasing mistuning is also visible for the AICs. A quite similar geometry was analyzed by Franz et al. [66] and the converging behavior of the aerodynamic damping was more pronounced compared to this case. However, their analysis is conducted solely using the FMM where the change in frequency has a linear effect on the damping. In the current study, however, a geometrical mistuning is implemented in conjunction with a higher order approach in which the mistuning alters the eigenvectors as well as the aerodynamics. In conclusion, the converging behavior might, in general, not be as pronounced as predicted by low order reduced models.

As a last step, the phase of the aerodynamic influence coefficients should be looked at. Figure 7.9 shows the phase between the real and imaginary part of the AICs for the shrouded configuration. The system becomes unstable when the phase gets positive. Similar to the damping, only minor differences can be observed for different mistuning amplitudes. With increasing mistuning amplitude, more modes lie outside of the vertical blank lines which indicate the tuned unstable modes. Therefore, it seems like the mistuning causes not only the most unstable damping to decrease but also to destabilize modes which were unstable before. This is surprising since recent publications always suggest the opposite to

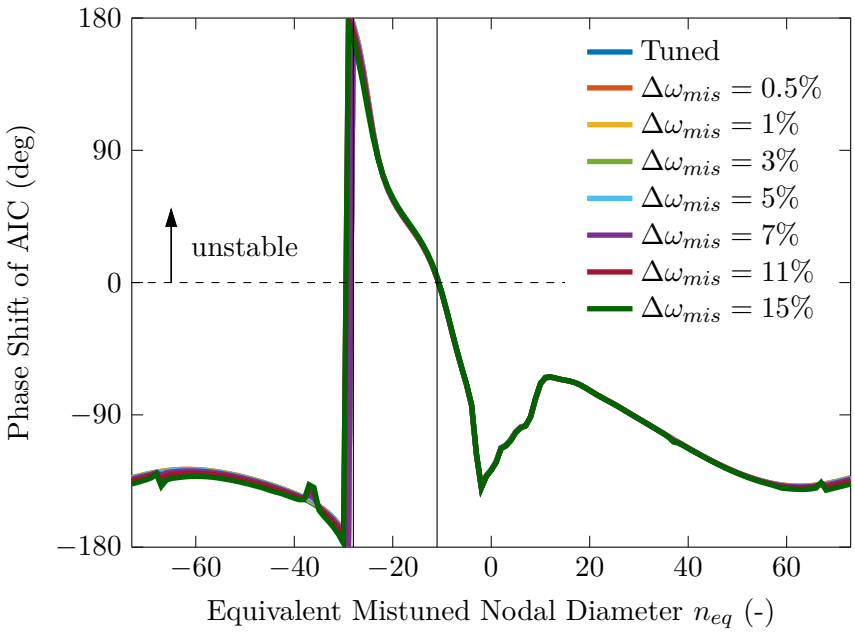

Figure 7.9: Phase Shift between Real and Imaginary Part of the Aerodynamic Influence Coefficients in Traveling Wave Space for Different Alternate Mistuning Amplitudes of the Shrouded Configuration

happen but it should be noted, that they all focuses on weakly coupled blades [64, 66].

The phase of the most unstable equivalent mistuned nodal diameter $n_{eq} = -19$ as a function of the mistuning amplitude is depicted in Fig. 7.10 for the shrouded bladed disk. The phase decreases firstly indicating a stabilizing behavior but increases continuously for a mistuning amplitude higher than 0.5%. A decrease in damping was reported once by Srinisivan and Tavares who used an alternate mistuning pattern to perturb the mode shapes while the eigenfrequencies were kept constant [71]. Similar to the work of Srinisivan and Tavares, the decrease in damping of the present case might also be attributed to the perturbation of the eigenform. Comparing the order of magnitude, the small decrease of the damping would be in conformity with the small alternation of the eigenvectors. This has to be addressed in more detail in further analyses.

The phase of the cantilevered case behaves completely different compared to the shrouded case, see Fig. 7.11. Firstly, there is not such a great variation of the phase with respect to n_{eq} neither for the tuned stable modes nor for the mistuned modes. Secondly, when the system is slightly perturbed, the curves flatten immediately inside the stable region.

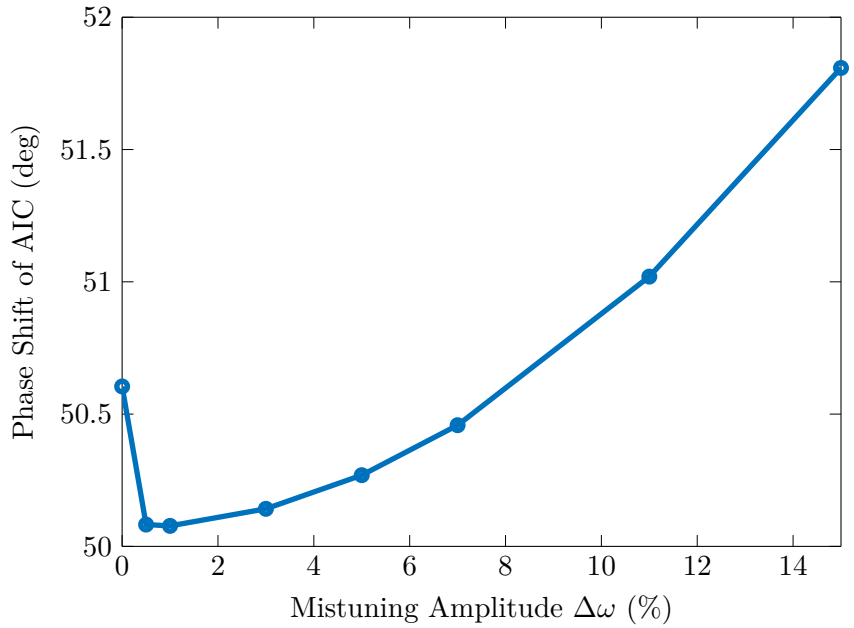

Figure 7.10: Phase Shift between Real and Imaginary Part of the Aerodynamic Influence Coefficients in Traveling Wave Space versus Alternate Mistuning Amplitude for the Most Unstable Equivalent Mistuned Nodal Diameter $n_{eq} = -19$ of the Shrouded Configuration

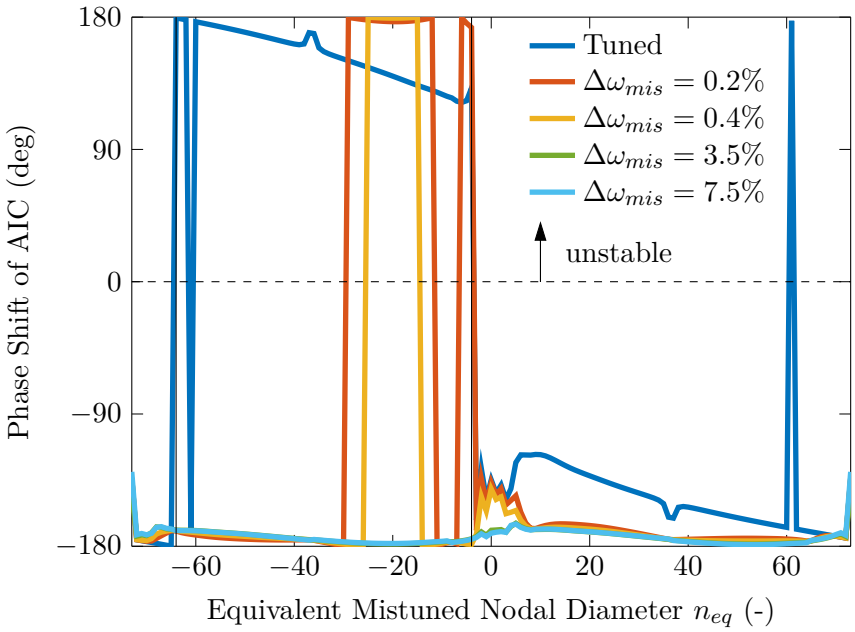

Figure 7.11: Phase Shift between Real and Imaginary Part of the Aerodynamic Influence Coefficients in Traveling Wave Space for Different Alternate Mistuning Amplitudes of the Cantilevered Configuration

7.3 Summary

Several attempts are made to explain the effect of mistuning on the flutter stability. While the behavior of the cantilevered blade is relatively well understood, it is difficult to interpret the results for the shrouded bladed disk.

For the shrouded configuration, the impact of mistuning on the aerodynamics is quite low. It is shown that in spite of high mistuning amplitude, the perturbation of the mode shapes remains low. One of the reasons might be the wide variation of the structural frequencies which disables the mistuning to couple the appropriate modes. As a consequence, when utilizing a linear aeroelastic solver, the damping also remains almost unchanged. Therefore, it is concluded that mistuning is not able stabilize the strongly coupled system in this case. On the contrary, mistuning even destabilizes previously stable modes and induces a decrease of damping of the most unstable tuned mode. Such a decrease is scarcely seen in the literature but was reported by Srinisivan and Tavares [71]. They attributed the decrease in damping to a perturbation of the mode shape which could also be the explanation for the current case. Another possibility is the unfavorable coupling of modes which might couple the aerodynamics in such a way that the phase of the aerodynamic work increases and thereby, destabilizes the system even more. However, the latter hypothesis should be seen from a numerical point of view and does not necessarily represent the physical behavior of the mistuned system. Nevertheless, the shrouded configuration remains still superior compared to the cantilevered blade disk. If material damping would be taken into account, it would shift the stability curve toward the stable region and probably stabilize the system.

For the cantilevered bladed disk, on the other hand, all frequencies lie in the same range, which fasciliates the coupling, so that in the presence of alternate mistuning, the mistuned mode consists of two modes with about the same MAC factor. The great change in the eigenvectors directly affects the aerodynamics and even a small mistuning is enough to stabilize the system. Aerodynamic work attains an approximately constant value for all harmonics when a small amount of mistuning is introduced and does not change for larger mistuning amplitudes.

The FMM fails to predict the mistuned stability of the shrouded bladed disk and qualitatively predicts the trend correctly for the cantilevered case. The shrouded case experiences a great change in frequency and in modes which the FMM is not able to capture. The quantitative aerodynamic damping difference between linearTRACE and the FMM might be attributed to the fact that the reduced order model ignores any changes in the eigenform and utilizes tuned aerodynamic influence coefficients which change significantly with mistuning. However, the latter aerodynamic effect is usually smaller than the structural [66].

8 Conclusions and Future Work

A bladed disk with a full-stick interlock connection representative of a strongly coupled system was analyzed within this thesis. In addition, by removing the cyclic symmetry boundary condition at the shroud interface, the same geometry but with a lower coupling was also part of the study as a cantilevered counterpart. Since the blade is relatively stiff, a linear modal analysis was favored. The aeroelastic analysis was conducted through a forced motion calculation in the linearized CFD solver linearTRACE. An alternate mistuning pattern was applied by proportionally scaling the Young's modulus. Several models were compared among each other including a one and a two sectors higher order model as well as the Fundamental Mistuning Model.

The key question raised in the beginning of this thesis, Sect. 1.2, were successfully addressed throughout the thesis.

1. A review of several reduced order models was conducted and it was concluded that while the FMM and AMM are more suitable for weakly coupled systems, the SNM and CMM approaches are able to predict the behavior of stronger coupled blade disk reasonably well. However, the set up of the latter two models is more complicated and for these reasons, the FMM was implemented and compared against higher order approaches in the present work.

2. For the tuned system, the predicted aerodynamic damping agreed quite well between the three methods. Some local peaks were encountered in the aerodynamic damping plot for the two sectors method. These local peaks might be due to a resonance condition of the forced motion computations.

   It was found that the effect of mistuning has less influence on the strongly coupled system compared to the weakly coupled bladed disk. The MAC factor showed that the mistuned modes of the shrouded bladed disk are quite similar to the tuned modes, especially the lower nodal diameters. In consequence, mistuning is not able to successfully couple modes among each other to stabilize the system due to the wide variation of the structural frequencies. On the contrary, higher levels of mistuning destabilized tuned stable modes and decreased the minimum aerodynamic damping. The decrease of the aerodynamic damping might be of numerical nature but further studies are needed to be conducted to analyze this behavior.

   A small mistuning level positively affected the cantilevered bladed disk. Further increase in mistuning stabilized the system and the aerodynamic work became independent of the inter-sector phase angle.

3. The existing process chain for the analysis of strongly coupled systems had to be adapted. In particular, several routines to pre- and post-process complex eigenforms were coded and verified. Furthermore, a code was implemented which allows to split the output of the modal analysis of the two sectors model into single modes for both sectors. This step is essential for the setup of the linear CFD computation.

4. The Fundamental Mistuning Model correctly predicted the stabilizing trend with increasing mistuning for the cantilevered case. There were some quantitative differences in the aerodynamic damping between the higher order method and the reduced model. The higher order approach included the perturbation of the modal frequencies and eigenforms which directly affected the aerodynamics. However, the selected reduced model assumed a linear relation between frequency, aerodynamic influence coefficients and damping, which explains the difference between the two approaches.

   On the other hand, the reduced order model failed to qualitatively and quantitatively resemble the mistuned results compared to the higher order approach for the shrouded case. Therefore, it is recommended to employ a more sophisticated and complex reduced model for the analysis of strongly coupled bladed disk.

Based on the results of this thesis, several points arise which might be the topic of further studies. Firstly, the decrease in the aerodynamic damping predicted by the linear solver linearTRACE has to be studied more in detail. It has to be identified whether the decrease is because of numerical issues or due to physical reasons. It is advisable to analyze the effects of mistuning on a geometrically different bladed disk to support or compromise the findings of this thesis. Secondly, a suitable reduced order model has to be implemented and the process chain further adapted to effectively study mistuned bladed disks at the DLR Institute of Aeroelasticity. Lastly, it is worth to investigate the quantitative damping differences of the cantilevered case between the FMM and linearTRACE more in depth. Several published analyses utilize reduced order models to study the effects of mistuning but the mistuned results are scarcely verified against a higher order approach. Additional quantitative comparisons would serve as a good basis so that the ROMs could be applied with more confidence in the development of industry projects.

References

[1] T. Klauke, U. Strehlau, and A. Kühhorn. Integer Frequency Veering of Mistuned Blade Integrated disks. *Journal of Turbomachinery*, 135(6), 2013.

[2] D. J. Ewins. *Modal Testing: Theory, Practice and Application.* Research Studies Press Ltd., 2nd edition, 2000.

[3] H. Grieb. *Verdichter für Turbo-Flugtriebwerke.* Springer Verlag, 2009.

[4] J. Nipkau. *Analysis of Mistuned Bladed Blisk Vibrations Using a Surrogate Lumped Mass Model with Aerodynamic Influences.* PhD thesis, Brandenburg University of Technology, 2011.

[5] F. Lane. System Mode Shapes in the Flutter of Compressor Blade Rows. *Journal of Aeronautical Sciences*, 23(1):54–66, 2000.

[6] C. Martel, R. Corral, and J. M. Llorens. Stability Increase of Aerodynamically Unstable Rotors Using Intentional Mistuning. *Journal of Turbomachinery*, 130(1), 2008.

[7] D. S. Whitehead. Effect of Mistuning on Vibration of Turbomachine Blades Induced by Wakes. *Journal of Mechanical Engineering Science*, 8(1):15–21, 1966.

[8] Y. Hanamura, H. Tanaka, and K. Yamaguchi. A Simplified Method to Measure Unsteady Forces Acting on the Vibrating Blades in the Cascade. *Bulletin of JSME*, 23(180):880–887, 1980.

[9] E.F. Crawley. Aeroelastic Formulation for Tuned and Mistuned Rotors. *AGARD Manual on Aeroelasticity in Axial-Flow Turbomachines. Volume 2. Structural Dynamics and Aeroelasticity*, 2:19–24, 1987.

[10] M. Nowinski and J. Panovsky. Flutter Mechanisms in Low Pressure Turbine Blades. *Journal of Engineering for Gas Turbines and Power*, 122(1):82–88, 2000.

[11] F. O. Carta. Coupled Blade-Disk-Shroud Flutter Instabilities in Turbojet Engine. *Journal of Engineering for Power*, 89(3):419–426, 1967.

[12] M. May. *Linearized Flutter Investigations of Mistuned Turbomachinery Blading.* PhD thesis, Technical University of Berlin, 2011.

[13] D. Vogt. *Experimental Investigations of Three-Dimensional Mechaninisms in Low-Pressture Turbine Flutter.* PhD thesis, Royal Institute of Technology, 2005.

[14] D. J. Ewins. Vibration Characteristics of Bladed Disk Assemblies. *Journal of Mechanical Engineering*, 15(3):165–186, 1973.

[15] P. W. Anderson. Absence of Diffusion in Certain Random Lattices. *Physical Review*, 109(5):1495–1505, 1958.

[16] D. J. Ewins. The Effects of Detuning Upon the Forced Vibrations of Bladed Disks. *Journal of Sound and Vibration*, 9(1):65–79, 1969.

[17] C. H. Hodges. Confinement of Vibration by Structural Irregularity. *Journal of Sound and Vibration*, 82(3):411–424, 1982.

[18] G. Ottarson and C. Pierre. A Transfer Matrix Approach to Free Vibration Localization in Mistuned Blade Assemblies. *Proceedings of the International Gas Turbines and Aeroengine Congress and Exposition*, 1993. Paper No. 93-GT-115.

[19] A. V. Srinisivan. Flutter and Resonant Vibration Characteristics of Engine Blades. *Journal of Engineering for Gas Turbines and Power*, 119(4):742–775, 1997.

[20] Y. Han, B. Xiao, and M. P. Mignolet. Expedient Estimation of the Maximum Amplification Factor in Damped Mistuned Bladed Disks. *Proceedings of the ASME Turbo Expo 2007: Power for Land, Sea and Air*, 2007. Paper No. GT2007-27353.

[21] M.P. Castanier and C. Pierre. Modeling and Analysis of Mistuned Bladed Disk Vibration: Status and Emerging Directions. *Journal of Propulsion and Power*, 22(2):384–396, 2006.

[22] S.-T. Wei and C. Pierre. Localization Phenomena in Mistuned Assemblies with Cyclic Symmetry Part I: Free Vibrations. *Journal of Vibration Acoustics, Stress and Reliability in Design*, 110(4):429–438, 1988.

[23] S.-T. Wei and C. Pierre. Localization Phenomena in Mistuned Assemblies with Cyclic Symmetry Part I: Forced Response. *Journal of Vibration Acoustics, Stress and Reliability in Design*, 110(4):439–449, 1988.

[24] E.F. Crawley and K.C. Hall. Optimization and Mechanism of Mistuning in Cascades. *Journal of Engineering for Gas Turbines and Power*, 107(2), 1984.

[25] R. E. Kielb, K. C. Hall, and T. Miyakozawa. The Effect of Unsteady Aerodynamic Asymmetric Perturbations on Flutter. *Proceedings of ASME Turbo Expo 2007: Power for Land, Sea and Air*, 2007. Paper No. GT2007-27503.

[26] K. Ekici, R. E. Kielb, K. C. Hall, and T. Miyakozawa. The Effect of Aerodynamic Asymmetries on Turbomachinery Flutter. 2009. Paper presented at the 47th AIAA Aerospace Sciences Meeting including The New Horizons Forum and Aerospace Exposition. Paper No. AIAA 2009-893.

[27] T. Miyakozawa. *Flutter and Forced Response of Turbomachinery with Frequency Mistuning and Aerodynamic Asymmetries*. PhD thesis, Duke University, 2008.

[28] D. L. Thomas. Dynamics of Rotionally Periodic Structures. *Journal for Numerical Methods in Engineering*, 14(1):81–102, 1979.

[29] W. C. Hurty. Dynamic Analysis of Structural Systems Using Component Modes. *AIAA Journal*, 3(4):678–685, 1965.

[30] R. R. Craig and M. C. C. Bampton. Coupling of Substructures for Dynamic Analyses. *AIAA Journal*, 6(7):1313–1319, 1968.

[31] R. R. Craig. *Structural Dynamics: An Introduction to Computer Methods*. Wiley, 1981.

[32] M. Myhre. *Numerical Investigation of the Sensitivity of Forced Response Characteristics of Bladed Disks to Mistuning*. Licentiate thesis, Royal Institute of Technology, 2003.

[33] C. H. Menq, J. H. Griffin, and J. Bielak. The Forced Response of Shrouded Fan Stages. *Journal of Vibration, Acoustics, Stress and Reliability in Design*, 108(1):50–55, 1986.

[34] M.-T. Yang and J. H. Griffin. A Reduced Order Approach for the Vibration of Mistuned Bladed Disk Assemblies. *Journal of Engineering for Gas Turbines and Power*, 119(1):161–167, 1997.

[35] G. Ottarson and C. Pierre. On the Effects of Interblade Coupling on the Statistics of Maximum Forced Response Amplitudes in Mistuned Bladed Disks. *Proceedings of the 36th Structures, Structural Dynamics and Materials Conference*, 5:3070–3078, 1995.

[36] F. Moyroud, G. Jacquet-Richardet, and T. Fransson. A Comparison of Two Finite Element Reduction Techniques for Mistuned Bladed Disks. *Journal of Engineering for Gas Turbines and Power*, 124(4):942–952, 2002.

[37] D.-M. Tran. Component Mode Synthesis Methods Using Interface Modes. Application to Structures with Cyclic Symmetry. *Computers and Structures*, 79(2):209–222, 2001.

[38] R. Bladh, M. P. Castanier, and C. Pierre. Component-Mode-Based Reduced Order Modeling Techniques for Mistuned Bladed Disks —Part I: Theoretical Models. *Journal of Engineering for Gas Turbines and Power*, 123(1):88–99, 2001.

[39] R. Bladh, M. P. Castanier, and C. Pierre. Component-Mode-Based Reduced Order Modeling Techniques for Mistuned Bladed Disks —Part II: Appppplication. *Journal of Engineering for Gas Turbines and Power*, 123(1):100–108, 2001.

[40] R. Bladh, M. P. Castanier, and C. Pierre. Reduced Order Modeling Techniques for Dynamic Analysis of Mistuned Multi-Stage Turbomachinery. *Proceeding of the ASME Turbo Expo 2001: Power for Land, Sea and Air*, 2001. Paper No. 2001-GT-0276.

[41] M. P. Castanier, Y.-C. Tan, and C. Pierre. Characteristic Constraint Modes for Component Mode Synthesis. *AIAA Journal*, 39(6):1182–1187, 2001.

[42] M. P. Castanier, G. Óttarson, and C. Pierre. A Reduced-Order Modeling Technique for Mistuned Bladed Disks. *Journal of Vibration and Acoustics*, 119(3):439–447, 1997.

[43] R. Bladh, M. P. Castanier, and C. Pierre. Reduced Order Modeling and Vibration Analysis of Mistuned Bladed Disk Assemblies with Shrouds. *Journal of Engineering for Gas Turbines and Power*, 121(3):515–522, 1999.

[44] J.M. Brown. *Reduced Order Modeling Methods for Turbomachinery Design.* PhD thesis, Wright State University, 2008.

[45] F. Schreyer, J. Gross, P. Reuss, M. Junge, and H. Schoenenborn. *Consideration of Interface Damping in Shrouded Mistuned Turbine Blades*, pages 105–112. Springer International Publishing, 2014.

[46] M.-T. Yang and J. H. Griffin. A Reduced-Order Model of Mistuning Using a Subset of Nominal System Modes. *Journal of Engineering for Gas Turbines and Power*, 123(4):893–900, 2001.

[47] D. Feiner and J. Griffin. A Fundamental Model of Mistuning for a Single Family of Modes. *Journal of Turbomachinery*, 124(4):597–605, 2002.

[48] D. Feiner and J. Griffin. Mistuning Identification of Bladed Disks Using a Fundamental Model —Part I: Theory. *Journal of Turbomachinery*, 126(1):150–158, 2004.

[49] D. Feiner and J. Griffin. Mistuning Identification of Bladed Disks Using a Fundamental Model —Part II: Application. *Journal of Turbomachinery*, 126(1):159–165, 2004.

[50] S.-H. Lim, R. Bladh, and M. P. Castanier. A Compact, Generalized Component Mode Mistuning Representation for Modeling Bladed Disk Vibration. *Proceedings of the 44th AIAA/ASME/ASCE/AHS Structures, Structural Dynamics and Material Conference*, 2003. Paper No. AIAA 2003-1545.

[51] A. Sinha. Reduced-Order Model of a Bladed Disk With Geometric Mistuning. *Journal of Turbomachinery*, 131(3), 2009.

[52] J. T. Wagner. Coupling of Turbomachine Blade Vibrations Through the Rotor. *Journal of Engineering for Power*, 89:502–512, 1967.

[53] A. Sinha and S. Chen. Higher Order Technique to Compute the Statistics of Forced Response of a Mistuned Bladed Disk Assembly. *Journal of Sound and Vibration*, 130(2):207–221, 1989.

[54] G. S. Happawana, O. D. I Nwokah, A. K. Bajaj, and M. Azene. Free and Forced Response of Mistuned Linear Cyclic Systems: A Singular Perturbation Approach. *Journal of Sound and Vibration*, 211(5):761–789, 1998.

[55] J. H. Griffin and T. M. Hoosac. Model Development and Statistical Investigation of Turbine Blade Mistuning. *Journal of Vibration Acoustics, Stress and Reliability in Design*, 106(2):204–210, 1984.

[56] J. H. Griffin. On Predicting the Resonant Response of Bladed Disk Assemblies. *Journal of Engineering for Gas Turbines and Power*, 110(1):45–50, 1988.

[57] P. Basu and J. H. Griffin. The Effect of Limiting Aerodynamic and Structural Coupling in Models of Mistuned Bladed Disk Vibration. *Journal of Vibration Acoustics, Stress and Reliability in Design*, 108(2):132–139, 1986.

[58] C.-C. Lin and M. P. Mignolet. An Adaptive Perturbation Scheme for the Analysis of Mistuned Bladed Disks. *Journal of Engineering for Gas Turbines and Power*, 119(2):153–160, 1997.

[59] E. P. Petrov, K. Y. Sanliturk, D. J. Ewins, and R. Elliot. Quantitative Prediction of the Effects of Mistuning Arrangement on Resonant Response of a Practical Turbine Bladed Disk. *Proceedings of the 5th National Turbine Engine High Cycle Fatigue Conference*, 2000.

[60] E. P. Petrov, K. Y. Sanliturk, and D. J. Ewins. A new method for dynamic analysis of mistuned bladed disks based on the exact relationship between tuned and mistuned systems. *Journal of Engineering for Gas Turbines and Power*, 124(3):586–597, 2002.

[61] P.-Y. Peng and M. T. Yang. Neural Networks Based Diagnostics for Mistuned Bladed Disk. *Proceedings of ASME Turbo Expo 2000: Power for Land, Sea, and Air*, 2000. Paper No. 2000-GT-0035.

[62] L. Lecce, G. Scarcelli, and R. D'Ischia, M. Guiseppe. Evaluation of the Mistuned Bladed Disk Dynamic Behavior by ANN (Artificial Neural Network). *The 9th Int. Symposium on Transport Phenomena and Dynamics of Rotating Machinery*, 2002.

[63] R. Corral, J. M. Gallardo, and C. Vasco. Aeroelastic Stability of Welded-in-Pair Low Pressure Turbine Rotor Blades: A Comparative Study Using Linear Methods. *Journal of Turbomachinery*, 129(1):72–83, 2007.

[64] R. E. Kielb, R. E. Feiner, J. H. Griffin, and T. Miyakozawa. Flutter of Mistuned Bladed Disks and Blisks with Aerodynamic and FMM Structural Coupling. *Proceedings of ASME Turbo Expo 2004: Power for Land, Sea, and Air*, 2004. Paper No. GT2004-54315.

[65] T. Fransson. FUTURE Project Final Report. http://www.transport-research.info/sites/default/files/project/documents/8541/final1-ftr-5-93.pdf. Accessed: 4.07.2016.

[66] D. Franz, L. Salles, and S. Stapelfeldt. Analysis of a Turbine Bladed Disk With Structural and Aerodynamic Mistuning. *Proceedings of ASME Turbo Expo 2017: Turbomachinery Technical Conference and Exposition*, 2017. Paper No. GT2017-64586.

[67] H.-P. Kersken. Time-Linearized and Time-Accurate 3D RANS Methods for Aeroelastic Analysis in Turbomachinery. *Journal of Turbomachinery*, 134(5), 2012.

[68] C. Reiber and M. Blocher. Potential of Aeroelastic Tailoring to Improve Flutter Stability of Turbomachinery Compressor Blades. *12th European Turbomachinery Conference*, 2017. Paper No. ETC2017-180.

[69] M. Schuff, T. Lengyel-Kampmann, and N. Forsthofer. Influence of the Steady Deformation on Numerical Flutter Prediction for Highly Loaded and Flexible Fan Blades. *Proceedings of ASME Turbo Expo 2017: Turbomachinery Technical Conference and Exposition*, 2017. Paper No. GT2017-64027.

[70] D. C. Wilcox. Reassessment of the Scale-Determining Equation for Advanced Turbulence Models. *AIAA Journal*, 26(11):1299–1310, 1988.

[71] A. V. Srinisivan and G. G. Tavares. Direct Use of Unsteady Aerodynamic Pressures in the Flutter Analysis of Mistuned Blades. *Proceedings of ASME 1994 International Gas Turbine and Aeroengine Congress and Exposition*, 2017. Paper No. 94-GT-347.

Appendix

The error introduced by not connecting the nodes in the vicinity of the blade root as discussed in the end of Sect. 5.4 is quantified. The verification is solely shown for the shrouded bladed disk for a low and a high mistuning amplitude of $\Delta\omega_{mis} = 1\%$ and $\Delta\omega_{mis} = 15\%$. Figure A1 shows the modal difference in frequency between a model with a corrected and an uncorrected interface for a mistuning amplitude of $\Delta_{mis} = 1\%$ and $\Delta_{mis} = 15\%$. As can be seen from the plot, the difference is quite low

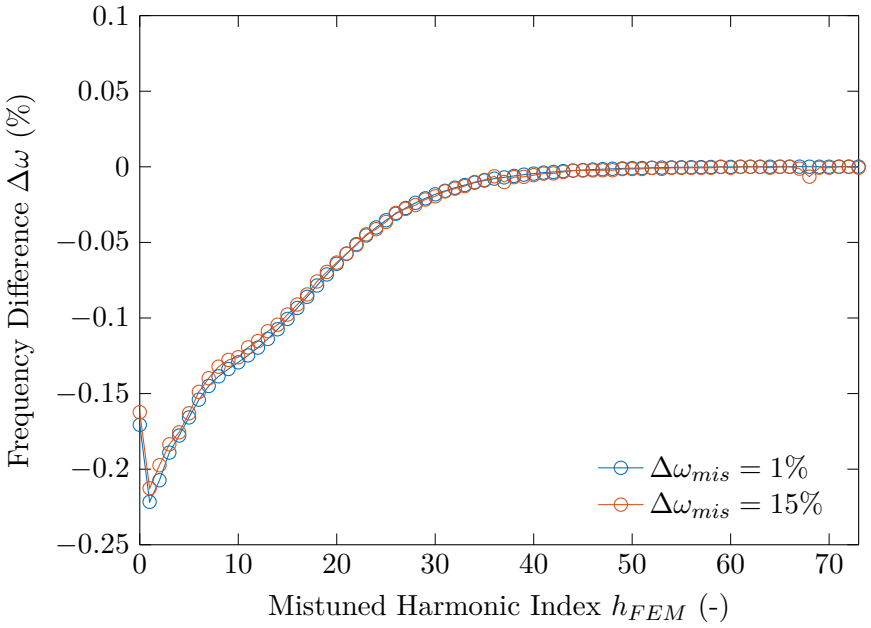

Figure A1: Frequency Difference Between Uncorrected and Corrected Two Sector Structural Model for a Low and a High Frequency Amplitude of the Shrouded Configuration

and in about the same order of magnitude for models with a different amount of sectors, compare Fig. 5.13a.

A direct comparison of the aerodynamic damping can be seen in Fig. A2a and the absolute difference between the corrected and the uncorrected in Fig. A2b. The introduced error in the damping is in the magnitude of 10^{-5} while the actual aerodynamic damping varies within a magnitude of 10^{-3}. Due to the magnitude difference of the error of 10^{-2}, it can be concluded that the results obtained by the uncorrected model are satisfying. In general, due to correction, the damping can be higher or lower as seen in Fig. A2b. The highest difference occurs at lower n_{eq} and at the local peaks,

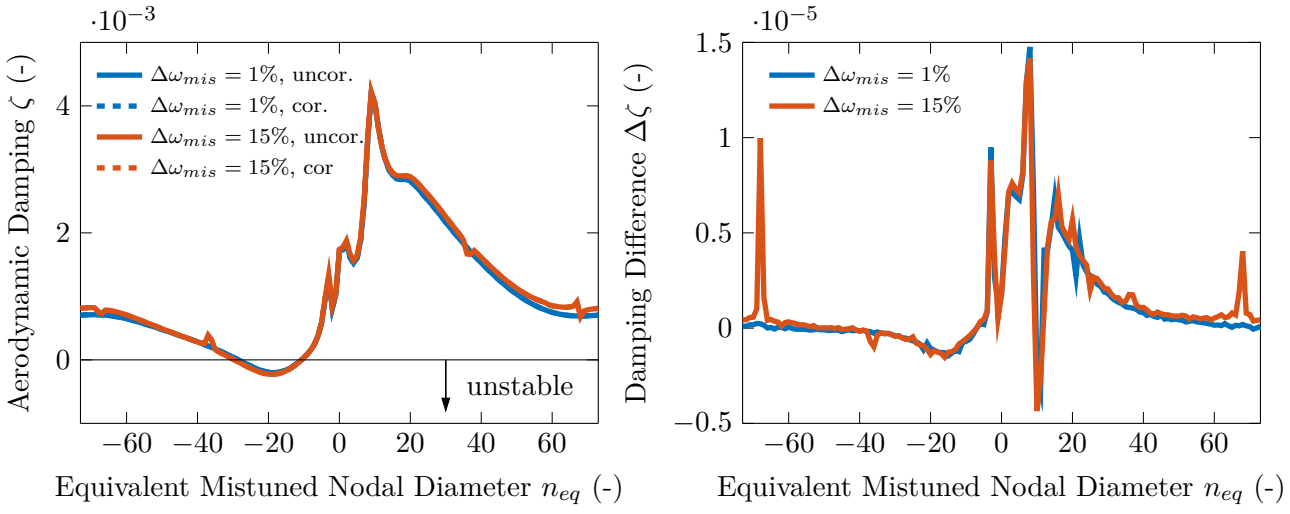

(a) Absolute **(b)** Absolute Difference, $\Delta\zeta = \zeta_{uncor} - \zeta_{cor}$

Figure A2: Aerodynamic Damping Comparison Between Uncorrected and Corrected Two Sector Structural Model for a Low and a High Frequency Amplitude

$n_{eq} = \pm 67$.

Nevertheless, the crucial differences would be at the most unstable modes and especially at the most unstable equivalent mistuned nodal diameter at $n_{eq} = -19$. It is important to show whether the curves greatly vary in this range or not. To satisfy this point, the damping curve around the most unstable mode is provided in Fig. A3.

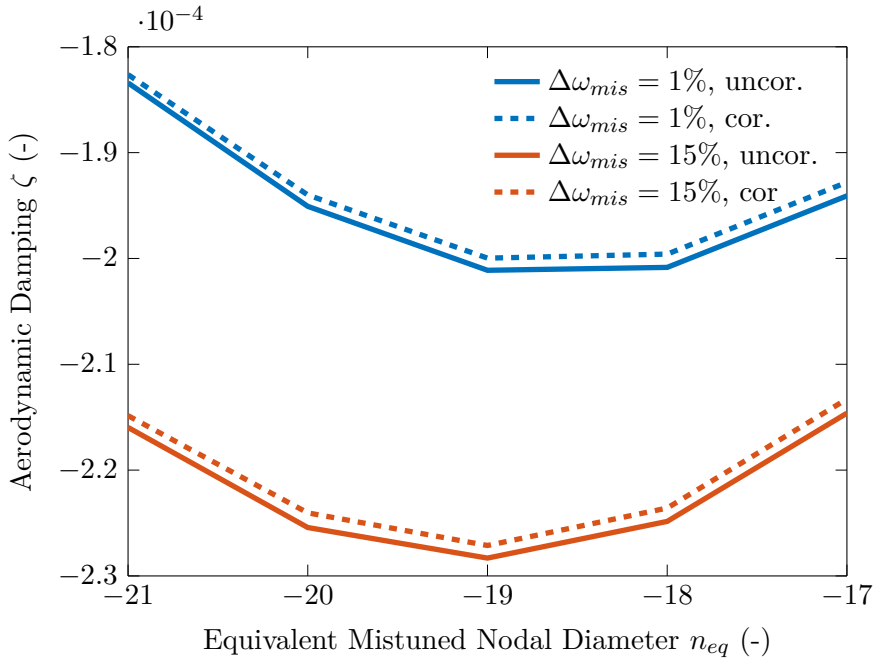

Figure A3: Aerodynamic Damping Between Uncorrected and Corrected Two Sector Structural Model for a Low and a High Frequency Amplitude; Zoom to the Range of Interest

By looking at Fig. A3, it gets obvious that the correction of the model simply slightly shifts the curve up for both mistuning amplitudes while the overall trend remains the same. Also, the absolute difference is quite small for all of the unstable modes. In summary, the introduced error in the modal as well as stability results is acceptable and does not compromise the major points of this thesis.